ABSTRACT

Title of Dissertation: FUNDAMENTAL STUDY OF DETONATION STRUCTURE IN ROTATING DETONATION ENGINE

Jason Burr
Doctor of Philosophy, 2020

Dissertation directed by: Professor Kenneth H. Yu
Department of Aerospace Engineering

The maturation of Brayton-cycle engines has led to a plateau in combustor performance where improvements between successive generations are slight. Detonation-based heat addition, in place of deflagrations, may offer an opportunity to radically improve the performance of both air-breathing and rocket systems. This work is focused on experimentally examining the fundamental flow structures associated with the propagation of a detonation wave in the Rotating Detonation Engine (RDE) configuration to aid in the design and understanding of RDE.

In RDE, one or more detonation waves propagate around the circumference of an annular combustor while reactants are continuously fed axially into the combustor to sustain the detonation wave(s). Numerous applied research activities involving RDE are currently underway to determine how best to integrate RDE in air-breathing and rocket applications. Understanding the complex flowfield of the detonation wave within this combustor has become one of the main challenges in developing RDE.

In this work the propagation of various detonation waves through a flowfield analogous to RDE are studied experimentally. A canonical configuration that "unwraps" the RDE into a linear channel is used to examine the effects of reactant species, mixedness, heat release, and layer height on the structure and propagation characteristics of detonation in RDE. This novel approach allows for the use of high-quality optical measurements such as schlieren, shadowgraph, natural luminescence, and chemiluminescence that reveal previously unseen features of the detonation wave; incomplete reactant mixing produces a number of visually discernable structures. The presence and formation of detonation triple points is directly examined in a variety of reactant compositions; in some cases, the decoupling and decay of detonations occurs if an insufficient number of triple points are present. Results from these experiments are compared to a novel partial mixing model that examines a possible mechanism responsible for experimentally observed waves propagating at a deficit in comparison to the speed predicted by one-dimensional Chapman-Jouguet (CJ) theory. The work presented in this thesis not only yields insight into the design, development, and testing of experimental RDE, but also provides valuable test data for validating numerical simulations of RDE.

FUNDAMENTAL STUDY OF DETONATION STRUCTURE IN ROTATING DETONATION ENGINE

by

Jason Burr

Dissertation submitted to the Faculty of the Graduate School of the
University of Maryland, College Park, in partial fulfillment
of the requirements for the degree of
Doctor of Philosophy
2020

Advisory Committee:
Professor Kenneth H. Yu, Chair/Advisor
Professor Arnaud C. Trouvé, Dean's Representative
Professor Christopher P. Cadou
Associate Professor Stuart J. Laurence
Professor Raymond J. Sedwick

Acknowledgements

First and foremost, I want to thank my advisor, Dr. Kenneth H. Yu, whose expertise, guidance, and support have helped to make me a better engineer and researcher throughout the last eight years. From the moment I set foot in the Advanced Propulsion Research Laboratory as an undergraduate student, he has always made himself available for discussion and would often offer great insight into my current ventures. I'll forever be grateful for the assistance he offered during long nights of testing in the laboratory, as well as for the numerous opportunities that he provided for me to travel, both domestically and internationally, to present my research. It has been a true pleasure to work with him, and I hope that such an opportunity may one day present itself again.

In a similar spirit, I would also like to thank the members of my dissertation committee, Dr. Arnaud Trouvé, Dr. Christopher Cadou, Dr. Stuart Laurence, and Dr. Raymond Sedwick. The road to the conclusion of my doctoral work has been a long one; their support, insight, suggestions, and criticisms have all been invaluable to this journey. Each of these individuals have made a lasting and meaningful impact on my time at the University of Maryland, and I greatly appreciate the time and effort they were willing to dedicate to assist me.

I also need to thank Dr. Chiping Li, Program Manager at the Air Force Office of Scientific Research (AFOSR), for the funding that enabled this work. The ability to conduct research critical for understanding a developing propulsion technology, as well

as to attend the annual AFOSR/ARO/NSF Basic Combustion Research Review, have fundamentally changed the way I view research.

Invaluable technical support and encouragement came from the personnel at Arnold Engineering Development Complex's (AEDC) Hypervelocity Wind Tunnel 9 in White Oak, Maryland. A special thanks to Mike Smith for his regular visits to the University of Maryland (UMD) and guidance in the development of various optical diagnostic techniques. The technical interactions with Dr. Michael Kendra, Dr. Eric Marineau, Dan Marren, and John Lafferty as a result of the UMD-AEDC program have strongly influenced my decision to continue working in experimental testing.

I am also grateful for all of the help and guidance I've received from the UMD Aerospace Engineering department office staff over these many years including but not limited to Tom Hurst, Matt Sinclair, Aileen Hentz, LaVita Williams, Laura Thorsen, Gabrielle Madison, Rebecca Sarni, Jessica Hoobler, Kevin Lewy, and Otto Fandino. Progress on my research would not have been possible without your efforts. In addition, I want to thank Mike Perna and Howie Grossenbacher for their help manufacturing several key components of my research facility, as well as offering their advice and feedback on designing custom hardware.

To my friends and colleagues at the Advanced Propulsion Research Laboratory, none of this would have been possible without your help and support. Dr. Amardip Ghosh, Dr. Camilo Aguilera, Dr. Sammy Park, Dr. Jonathan Geerts, and Dr. Robert Fievisohn helped to guide and mentor me during the early years of developing my experimental hardware and were always quick to offer advice and feedback when prompted. Kyung-Hoon Shin, Shikha Redhal, Mithuun Kanapathipillai, and Minwook

Chang each assisted me in further refining and collecting my experimental research, despite the often-long hours and late evenings required to do so. To all of you, thank you immensely for your support and encouragement, and I wish you the best on your own endeavors.

I would also like to thank all of my friends from graduate school who helped to make my life outside of the lab that much more enjoyable. To Dr. Joseph Chung, Dr. Xiao Zhang, Dr. Ryan Houim, Dr. Qina Diao, Vijay Ramasubramanian, Dr. Matthew Marcus, Dr. Joshua Sloane, Dr. Jarred Young, Eric Frizzell, Melissa Adams, Dr. Adam Halperin, Dr. Adriane Faust, Dr. Pratik Saripalli, Dr. Elaine Petro, Dr. John Vitucci, Dr. Vera Klimchenko, Kyle Zittle, Andrew Ceruzzi, Dr. Gabe Goodwin, and Dr. Nathan Shumway, thank you. Each and every one of you offered words of encouragement and advice at times when I needed it, and I cannot possibly imagine graduate school without any of you in it.

Of course, I owe my deepest thanks to my family – my mother, my father, and my sister who have always been there and guided me when I needed them most. They have been, and no doubt will continue to be, one of the driving forces that seems to always get me through impossible odds. Words are insufficient to succinctly describe how much I truly owe them.

Table of Contents

List of Figures and Tables

List of Abbreviations

DDT	Deflagration to Detonation Transition
CJ	Chapman-Jouguet
VN	von Neumann
ZND	Zel'dovich – von Neumann – Döring
ODWE	Oblique Detonation Wave Engine
PDE	Pulse Detonation Engine
RDE	Rotating Detonation Engine
DRDE	Disk Rotating Detonation Engine
LMDE	Linear Model Detonation Engine
eLMDE	Extended Linear Model Detonation Engine
PLIF	Planar Laser-Induced Fluorescence
PMT	Photomultiplier
AFRL	U.S. Air Force Research Laboratory
NRL	U.S. Naval Research Laboratory

Chapter 1: Introduction

1.1 Overview and Motivation

Development of detonation-based combustors has been driven by a desire to outperform existing constant pressure systems [1.1-1.3]. The Rotating Detonation Engine (RDE) has emerged as the lead candidate due to its applicability in both air-breathing and rocket systems [1.4-1.7]; benefits such as the potential increase in thermodynamic performance, simple design, compact reaction zone, cyclical heat addition, and ease of integration into aerospike nozzles make the RDE an ideal choice for practical implementation [1.8-1.10].

RDE combustor geometry is characterized by an annular channel with one or more detonations propagating around the circumference, as shown in Fig. 1.1 [1.4]. A continuous supply of reactants in the axial direction sustains the detonation wave; reactant injection is suppressed immediately in the wake of the detonation but resumes as the detonation moves away and the local flow continuous to expand. Reactant confinement in the RDE is achieved to the sides by the annulus walls, below by the injection plane, and above by the combustion products from the previous cycle. Unwanted reactant burning, poor injector mixing, heat transfer losses, and development of suitable high-

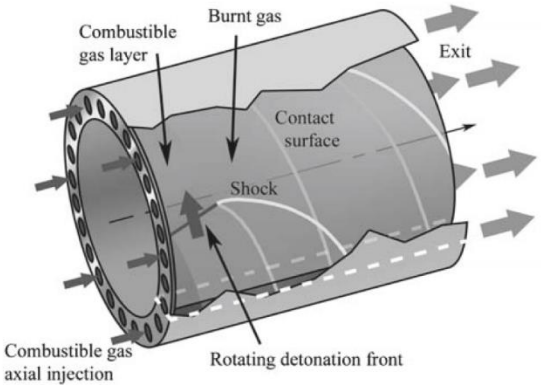

Figure 1.1: A schematic of flowfield in a rotating detonation engine [1.4].

temperature materials are all key issues to RDE that need to be addressed prior to practical implementation [1.3].

Experimental insight into RDE operation dates back to the late 1950's when Voitsekhovskii sought to sustain a detonation wave for study and inadvertently developed a facility analogous to the modern RDE [1.11]. In the 1960s and 1970s numerous researchers examined the propagation of a detonation through a layer of reactive gas [1.12-1.14]. A number of recent investigations have sought to improve RDE understanding in ways that range from providing insight into flow physics, to integration for flight applications [1.15-1.18]. Numerical efforts have examined the three-dimensional detonation structure and produced insightful visualizations of the RDE flowfield [1.5,1.19-1.21]. However, little to no experimental data are available to compare or validate the structures from these detailed simulations.

Current investigation of RDE is driven by both experimental and numerical studies. In both cases restrictions exist on understanding the nature of the detonation flowfield. Experimental data are limited by the quality of the optical measurements that are able to be made when observing an annular combustor; numerical results are limited by computational expense and a lack of data to validate against. A simple and canonical configuration that is able to distill the essence of the RDE flowfield into an easily visualized framework is of significant value to improving the understanding of the fundamental detonation structure.

1.2 Technical Objectives

The primary objective of this work is to investigate the fundamental structure of the RDE flowfield. The goal is to accurately identify and characterize the features

pertinent to detonation propagation by using a novel combustor that captures the essence of the RDE configuration. Unlike previous efforts, this combustor will allow for integral visualization techniques of the detonation-reactant, thereby allowing for direct observation of the 1) primary detonation wave, 2) reactant layer, 3) oblique shock, 4) transverse shock features, and 5) heat release.

The linearized combustor allows for variation in the reactant composition, mixedness, and layer height, as well as control over pre-detonator conditions. The flexibility of the linear combustor allows for rapid testing and flowfield evaluation of numerous RDE configurations. Propagation modes for these different conditions are characterized experimentally through the identification of structures such as transverse waves, reaction zones, and triple points.

Data collected from the experimental studies of the various fuels are used to inform an analytical model of partially mixed RDE propagation. Results from the model are compared with experimental data to identify possible causes of observed detonation wave speeds. Additionally, collected data are assembled for use in future numerical validation and collaboration efforts.

This work will include the following:

- Development and testing of a new novel combustor configuration that captures the essence of the RDE flowfield, neglecting curvature.
- High-quality visualizations of detonations propagating through partially-mixed and orthogonally injected reactant jets of various compositions.
- Identification of the influence of reactant mixing on the structure of detonations in RDE.

- Visualization of the reactant refresh process following a detonation transit and the role of feed plenum dynamics in this recovery.
- Investigation of detonation propagation modes for hydrocarbon mixtures with respect to transverse waves and heat release.
- A simplified analytical model of mixing limited detonation propagation and the resulting impact on detonation wave speed.

1.3 Scope

The scope of this work includes the investigation of several fuel-oxidizer mixtures commonly used in RDE through the use of a novel combustor configuration that simplifies the RDE flowfield into a linearized analog. The linearized investigation neglects the curvature of the RDE annulus and the steady-state operation of the device. Instead, the focus is on identifying the structure of the detonation and oblique shock waves, the partially mixed reactants and their passage through the reaction zone, and the subsequent recovery of reactant jets to the decaying pressure trailing the detonation wave.

Insight into the stability and propagation modes of detonation in RDE will require direct observation of features such as strong transverse shocks, shock reflections, and triple points. Implementation of line-of-sight visualization techniques such as schlieren, shadowgraph, luminescence, and chemiluminescence, as well as time-resolved measurements of dynamic pressure and heat release are required to reveal these features.

Once the fundamental structure of the detonation front is established for the different fuel-oxidizer mixtures, a simplified mixing model based on the observed

flowfields is created. This model relies upon the experimentally observed heat release distributions, wave speeds, and simplified flowfield assumptions. Results from this model are used to explain, in part, the experimentally observed wave speeds in RDE.

1.4 References

[1.1] G. D. Roy, S. M. Frolov, A. A. Borisov, and D. W. Netzer. Pulse detonation propulsion: challenges, current status, and future perspective. Progress in Energy and Combustion Science, 30(6):545-672, 2004.

[1.2] F. A. Bykovskii, S. A. Zhdan, and E. F. Vedernikov. Continuous Spin Detonations. Journal of Propulsion and Power, 22(6):1204-1216, 2006.

[1.3] F. K. Lu and E. M. Braun. Rotating Detonation Wave Propulsion: Experimental Challenged, Modeling, and Engine Concepts. Journal of Propulsion and Power, 30(5):1125-1142, 2014.

[1.4] M. Hishida, T. Fujiwara, and P. Wolanski. Fundamentals of rotating detonations. Shock Waves 19(1):1-10, 2009.

[1.5] D. Schwer and K. Kailasanath. Numerical investigation of the physics of rotating-detonation-engines. Proceedings of the Combustion Institute, 33(2):2195-2202, 2011.

[1.6] J. A. Nicholls, R. E. Cullen, and K. W. Ragland. Feasibility studies of a rotating detonation wave rocket motor. Journal of Spacecraft and Rockets, 3(6):893-898, 1966.

[1.7] P. I. Shen and T. C. Adamson Jr. Theoretical Analysis of a Rotating Two-Phase Detonation in Liquid Rocket Motors. Astronautica Acta, 17(4):715-728, 1972.

[1.8] K. Kailasanath. Review of Propulsion Applications of Detonation Waves. AIAA Journal, 38(9):1698-1708, 2000.

[1.9] P. Wolanski. Detonative propulsion. Proceedings of the Combustion Institute, 34(1):125-158, 2013.

[1.10] F. Falempin, E. Daniau, F. Getin, F. Bykovskii, and S. Zhdan. Toward a Continuous Detonation Wave Rocket Engine Demonstrator. In 14th AIAA/AHI Space Planes and Hypersonic Systems and Technologies Conference, AIAA Paper 2006-7956, Nov. 2006.

[1.11] B. V. Voitsekhovsky. Stationary detonation. Reports of USSR Academy of Sciences, 129(6):1254-1256, 1959.

[1.12] W. P. Sommers and R. B. Morrison. Simulation of Condensed-Explosive Detonation Phenomena with Gases. The Physics of Fluids, 5:241, 1962.

[1.13] E. K. Dabora, J. A. Nicholls, and R. B. Morrison. The influence of a compressible boundary on the propagation of gaseous detonation. Symposium (International) on Combustion, 10(1):817-830, 1965.

[1.14] M. Sichel and J. C. Foster. The ground impulse generated by a plane fuel-air explosion with side relief. Acta Astronautica, 6(3-4):243-256, 1979.

[1.15] L. Thomas, F. Schauer, J. Hoke, and A. Naples. Buildup and Operation of a Rotating Detonation Engine. In 49th AIAA Aerospace Sciences Meeting, AIAA Paper 2011-602, Jan. 2011.

[1.16] J. Kindracki, P. Wolanski, and Z. Gut. Experimental research on the rotating detonation in gaseous fuels-oxygen mixtures. Shock Waves, 21(2):75:84, 2011.

[1.17] B. A Rankin, D. R. Richardson, A. W. Caswell, A. G. Naples, J. L. Hoke, and F. R. Schauer. Chemiluminescence imaging of an optically accessible non-premixed rotating detonation engine. Combustion and Flame, 176(1):12-22, 2017.

[1.18] Y. Shao and J. P. Wang. Continuous Detonation Engine and Effects of Different Types of Nozzle on Its Propulsion Performance. Chinese Journal of Aeronautics, 23(6):647-652, 2010.

[1.19] N. Tsuboi, Y. Watanabe, T. Kojima, and A. Koichi Hayashi. Numerical estimation of the thrust performance on a rotating detonation engine for a hydrogen-oxygen mixture. Proceedings of the Combustion Institute, 35(2):2005-2013, 2015.

[1.20] R. Zhou and J. P. Wang. Numerical investigation of flow particle paths and thermodynamic performance of continuously rotating detonation engines. Combustion and Flame, 159(12):3632-3645, 2012.

[1.21] C. A. Nordeen, D. Schwer, F. Schauer, J. Hoke, T. Barber, and B. Cetegen. Thermodynamic model of a rotating detonation engine. Combustion, Explosion, and Shock Waves, 50:568-577, 2014.

Chapter 2: Background

2.1 Detonation Theory

2.1.1 Thermodynamics

Study of detonation-based heat addition systems necessitates a brief discussion on the fundamentals of detonation thermodynamics. The Chapman-Jouguet (CJ) theory is the simplest model of a detonation wave; the CJ theory assumes that a detonation wave can be modeled as an infinitely thin shock wave with heat release occurring in the wave-fixed frame [2.1]. A diagram of this framework is shown in Fig. 2.1.

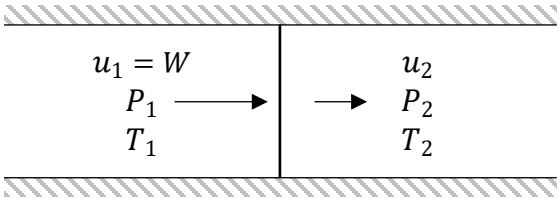

Figure 2.1: Simple CJ theory detonation model in the wave-fixed frame.

In the simplest CJ theory, the detonation propagates into a quiescent gas, such that the velocity u_1 corresponds to the detonation wave speed W. By assuming the reactants and products can be treated as calorically perfect gases with equal heat capacities, the conservation of mass, momentum, and energy equations are expressed as follows:

$$\rho_1 u_1 = \rho_2 u_2 \tag{2.1}$$

$$P_1 + \rho_1 u_1^2 = P_2 + \rho_2 u_2^2 \tag{2.2}$$

$$c_P T_1 + \frac{1}{2}u_1^2 + q_{in} = c_P T_2 + \frac{1}{2}u_2^2$$

(2.3)

Note that in Eqn. 2.3 the entirety of heat addition is lumped into a single parameter in the energy equation, q_{in}. The equation of state assumes an ideal gas and is given by:

$$P = \rho RT$$

(2.4)

Combination of the mass and momentum equations yields the equation for the Rayleigh line:

$$\frac{P_2}{P_1} = \left[-\frac{W^2}{P_1 v_1}\right] \cdot \frac{v_2}{v_1} + \left[1 + \frac{W^2}{P_1 v_1}\right]$$

(2.5)

Density (ρ) has been replaced with its reciprocal specific volume (v) in the above and subsequent expressions. It is apparent that in *P*-*v* space the slope of the Rayleigh line is dependent upon the incident wave speed, W. Conservation of mass, momentum, and energy, in addition to the equation of state, yields the Hugoniot curve:

$$\frac{P_2}{P_1} = \frac{\left[\frac{\gamma+1}{\gamma-1} + \frac{2\gamma}{\gamma-1} \cdot \hat{q}\right] - \frac{v_2}{v_1}}{\left[\frac{\gamma+1}{\gamma-1}\right]\frac{v_2}{v_1} - 1}, \qquad \hat{q} = \frac{q_{in}}{c_P T_1}$$

(2.6)

Two Hugoniot curves are shown in Fig. 2.2. The Hugoniot curve without heat addition, often referred to as the "Shock-Hugoniot", corresponds to the locus of all states that satisfy the mass, momentum, and energy equations without heat addition and

is drawn in black in Fig. 2.2. Similarly, the red curve ($\frac{q_{in}}{c_P T_1}$=0.5) corresponds to the locus of all states after heat is added to the flow.

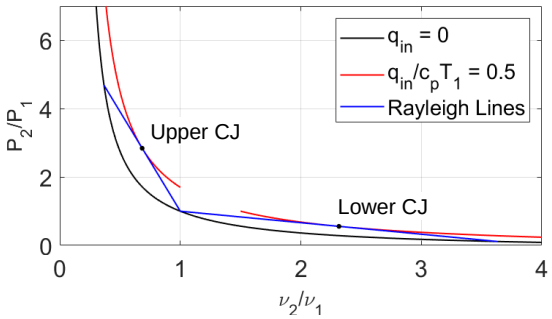

Figure 2.2: Hugoniot curves with and without heat release in *P-v* space. Rayleigh lines for CJ points included.

The two branches of the Hugoniot with heat addition correspond to detonation and deflagration solutions. On the detonation branch the specific volume decreases and the pressure increases; on the deflagration branch the pressure decreases and the specific volume increases. Additionally, the wave speeds corresponding to points along the detonation branch are supersonic while those along the deflagration branch are subsonic.

On each branch there is a single point where the Rayleigh line is tangent to the Hugoniot curve with heat addition. This point is the Chapman-Jouguet point and is indicated as the upper and lower CJ points in Fig. 2.2 for the detonation and deflagration branches, respectively. The Rayleigh lines corresponding to these points are shown in blue. For the detonation CJ point, the gas is shocked along the Shock-Hugoniot to where it intersects with the Rayleigh line (the von Nuemann point), and then heat is added to the flow along the Rayleigh line until it reaches the upper CJ point.

The entropy of the gas along the Hugoniot curve with heat addition is shown in Fig. 2.3, and can be expressed as:

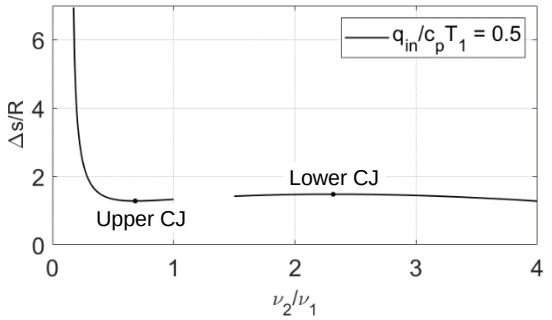

Figure 2.3: Entropy corresponding to Hugoniot curve with heat release.

$$\frac{\Delta s}{R} = \frac{1}{\gamma - 1}\ln\left(\frac{P_2}{P_1}\right) + \frac{\gamma}{\gamma - 1}\ln\left(\frac{v_2}{v_1}\right)$$

(2.7)

It is apparent by inspection that the CJ point along the detonation branch corresponds to a global minimum in entropy rise. This entropy minimum, which corresponds to a maximum in thermodynamic efficiency, drives the pursuit for a system that utilizes detonation-based heat addition.

Detonations corresponding to the upper CJ point are referred to as CJ detonations. These detonations have the characteristics of 1) minimum entropy, 2) sonic flow downstream of the wave, and 3) the minimum wave speed along the detonation branch. Note that the third characteristic is an equivalent expression of the tangency criteria discussed previously. The wave speed of CJ detonations can be derived by equating Eqn. 2.5 and Eqn. 2.6, and is expressed as:

$$\frac{V_{CJ}^2}{a_1^2} = [(\gamma + 1)\hat{q} + 1] + \sqrt{[(\gamma + 1)\hat{q} + 1]^2 - 1}$$

(2.8)

Where a_1 is the reactant sound speed. In detonation there is a significant pressure and temperature rise, as well as species changes due to chemistry. While the assumption of a calorically perfect gas no longer applies, chemical mechanisms can be used to approximate the state after heat addition. Software such as *NASA Chemical Equilibrium with Applications (CEA)*, *CHEMKIN*, or *Cantera* can be used to calculate the one-dimensional CJ detonation speed for real gas compositions.

2.1.2 Structure

While there is good agreement between this one-dimensional CJ speed and experimental measurements, a detonation wave is not one-dimensional [2.2]. Instead of a smooth planar shock with uniform heat release, the detonation wave is instead composed of numerous incident shocks, Mach stems, and transverse waves [2.3]. The typical structure of a detonation wave is shown in Fig. 2.4.

At the bottom of Fig. 2.4 a Mach stem with closely coupled reaction zone is centered in the figure. To either side of the Mach stem are outwards propagating transverse waves, driven by the elevated pressure behind the Mach stem. These transverse waves propagate into incident shocks, which are weaker than the Mach stem

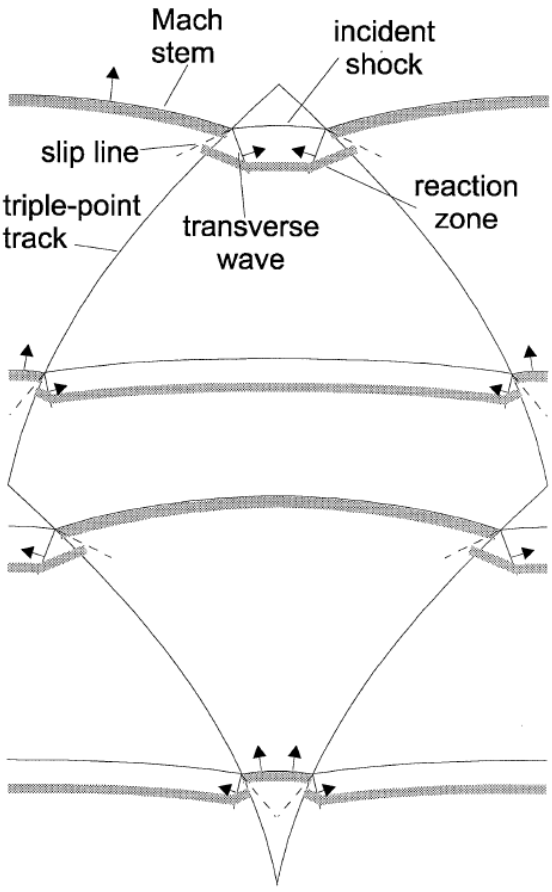

Figure 2.4: Schematic illustration of wave motion in a detonation cell. Detonation propagates upward [2.4].

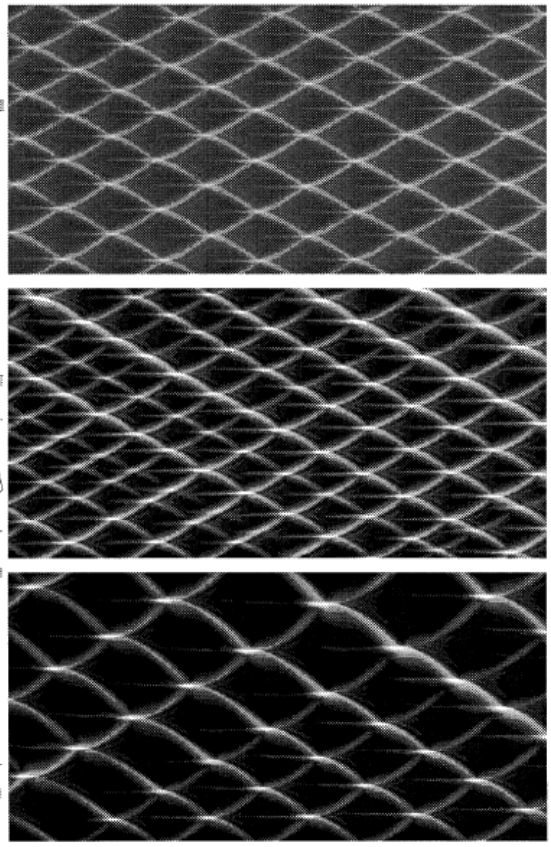

Figure 2.5: Numerically simulated detonation cells. Dimensionless activation energies increasing from top to bottom [2.4].

and allow the reaction zone to lag behind. The intersection of these three flow structures form a triple point [2.3].

As the detonation front moves upwards the Mach stem weakens and the transverse shocks continue to propagate outwards. Eventually the transverse waves from adjacent Mach stems intersect to form a new Mach stem; the original Mach stem weakens further into an incident shock and the cycle continues anew. The trajectories of the triple points trace out a characteristic fish-scale like structure known as the "detonation cell" (λ) [2.3]. A set of numerically simulated detonation cells are shown in Fig. 2.5. The regularity of the detonation cell size is dependent upon the normalized mixture activation energy [2.4]; significant variation in detonation cell size for a well-mixed reactant composition is not uncommon.

Unfortunately, no theory exists that is capable of predicting the size of the detonation cell from fundamental theory [2.3]. Numerous attempts have been made to empirically correlate the detonation cell to parameters such as the reaction zone length [2.5-2.6] or the mixture activation energy [2.4]. However, these approaches are poor at extrapolating the detonation cell size beyond the datasets used. As a result,

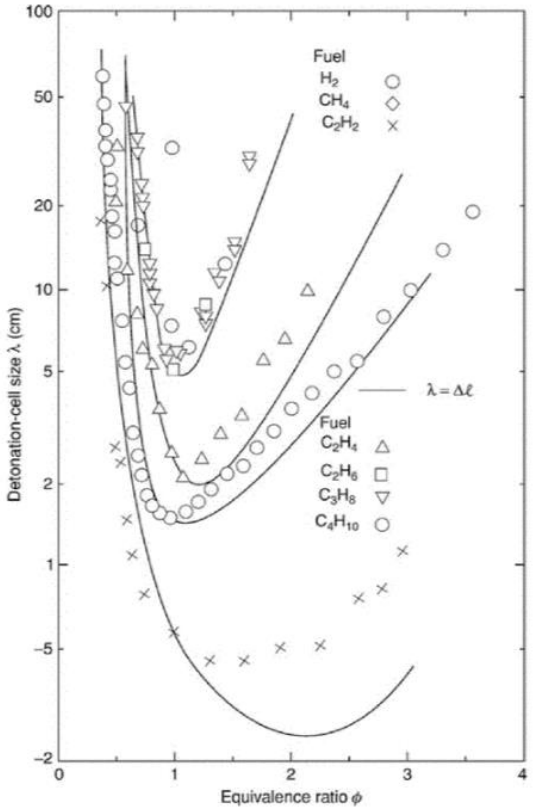

Figure 2.6: Detonation cell size as a function of equivalence ratio for various fuel-air mixtures [2.8].

reference databases of experimentally measured cell sizes have been assembled [2.9].

A selection of fuel-air detonation cell sizes, for various equivalence ratios, are shown in Fig. 2.6. The solid lines in the figure correspond to the fit approach used by Shchelkin and Troshin, where the cell size scales linearly with the reaction zone length and is calibrated at stoichiometric conditions. Detonation cell sizes are minimum near stoichiometric conditions and quickly grow by one or more order of magnitude in both the fuel-rich and fuel-lean limits.

2.2 Propulsion Applications of Detonation

2.2.1 Standing Detonation Engine

As early as 1940 Zel'dovich considered a hypothetical combustor where a standing detonation wave was stabilized, as shown in Fig. 2.7 [2.10]. Zel'dovich only examined the system analytically from the perspective of cycle efficiency and determined that a sizable fraction of the heat release would be required to couple with the detonation wave to maintain its position. He concluded that the "practical application of detonation combustion to energy production [is] inadvisable" [2.10].

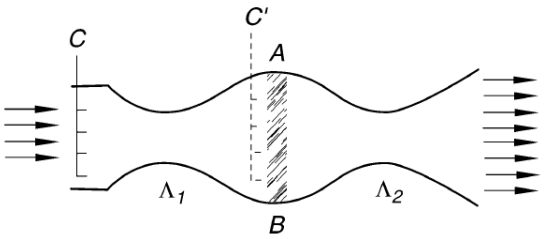

Figure 2.7: Early concept for a standing detonation wave engine [2.10].

Wintenberger and Shepherd would later examine the standing detonation engine from the perspective of the Hugoniot [2.11]. In deriving the Hugoniot equation (Eqn. 2.6) it was assumed the reaction waves propagated into a quiescent gas. The resulting points on the Hugoniot curve, each with their own Rayleigh line and wave velocity,

necessarily have different stagnation conditions. The "Stagnation Hugoniot" is derived such that the stagnation state for every point on the Hugoniot curve is equal [2.11]. Assuming a calorically perfect gas, the Stagnation Hugoniot can be expressed as:

$$\frac{P_2}{P_1} = 1 + \frac{2\gamma}{\gamma - 1}\left(1 - \frac{\nu_2}{\nu_1}\right)\left[\frac{1 + \hat{q}_0 - \frac{\nu_2}{\nu_1}}{\frac{\gamma+1}{\gamma-1}\left(1-\frac{\nu_2}{\nu_1}\right)\frac{\nu_2}{\nu_1} + \frac{\nu_2}{\nu_1} - (1+\hat{q}_0)}\right], \qquad \hat{q}_0 = \frac{q_{in}}{c_P T_{01}} \tag{2.9}$$

Note that $\hat{q}_0$ is normalized by the stagnation temperature of the flow. Equation 2.7 is still valid for determining the entropy along the Stagnation-Hugoniot. The resulting curve is shown in Fig. 2.8 in blue, with the traditional Hugoniot curve for the same amount of heat release ($\hat{q}_0$=0.5) in black. Note that in the Stagnation-Hugoniot curve the upper CJ point still corresponds to a local minimum, but the shock-incurred losses now outweigh the benefits of detonation-based heat addition.

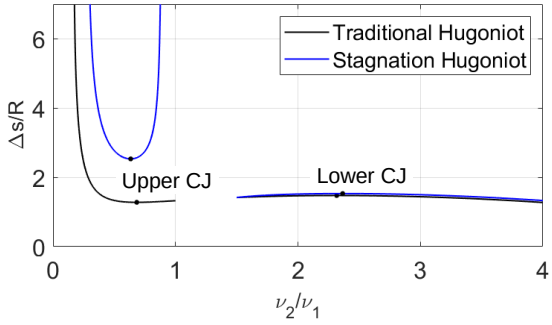

Figure 2.8: Entropy corresponding to a traditional and Stagnation Hugoniot analysis ($\hat{q} = \hat{q}_0$=0.5).

No serious ventures to construct a standing detonation engine are noted.

2.2.2 Oblique Detonation Wave Engine

An additional challenge faced by the standing detonation engine is keeping the wave, which propagates through a quiescent gas at speeds on the order of kilometers per second, balanced by the reactant inflow; the oblique detonation wave engine (ODWE) achieves detonation by either a wedge or conical deflection source, and as a result can operate over a wide range of flow conditions [2.12].

A simplified flowfield of the oblique detonation near the deflection source is shown in Fig. 2.9. Initial flow deflection behind the wedge is achieved by a nonreactive shock. The elevated temperature in the wake of the lead shock leads to ignition of the reactants by means of deflagration near the deflection surface. Upwards spread of this reaction zone leads to an interaction with the incident shock, allowing the two to couple and produce a reactive shock [2.12].

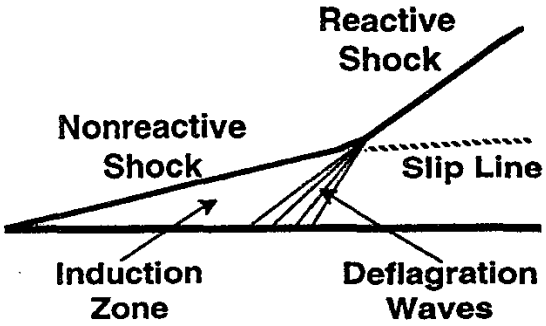

Figure 2.9: Schematic of the basic structure of wedge-induced oblique detonation waves [2.12].

Common architectures utilizing ODWE explore applications analogous to scramjet, Fig. 2.10. Although the ODWE suffers from performance losses comparable to the standing detonation, the compact reaction zone of the ODWE is beneficial attribute in applications where combustor residence time is small [2.13].

For completeness, the oblique detonation wave serves as the combustion source for ram accelerators [2.14]. In these systems, a conical projectile is fired into a tube of detonable gasses. The resulting oblique detonations that form on this projectile provide a large pressure differential that continue to accelerate the projectile through the gas.

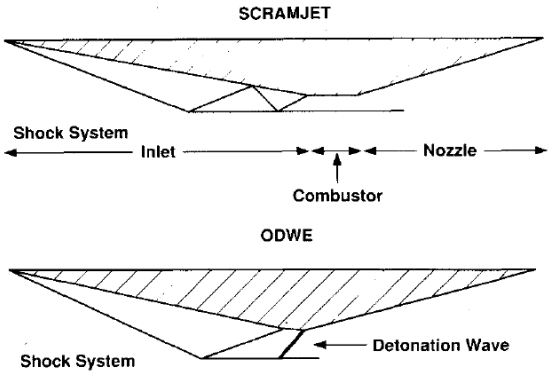

Figure 2.10: Schematic of shock structure for scramjet engine and ODWE, including detonation [2.13].

2.2.3 Pulse Detonation Engine

The pulse detonation engine (PDE) reflects the first modern effort to facilitate the use of detonation-based heat addition. PDE geometry is essentially a long tube filled with detonable gases [2.15]. PDEs are operated cyclically, as shown in Fig. 2.11; PDE operation includes 1) reactant fill, 2) ignition, 3) detonation propagation, 4) product exhaust, and 5) purge [2.16]. Because the detonation propagation speed is much greater than the reactant or purge gas flow velocity, the traditional Hugoniot derivation applies and benefits of detonation-based heat addition are attainable.

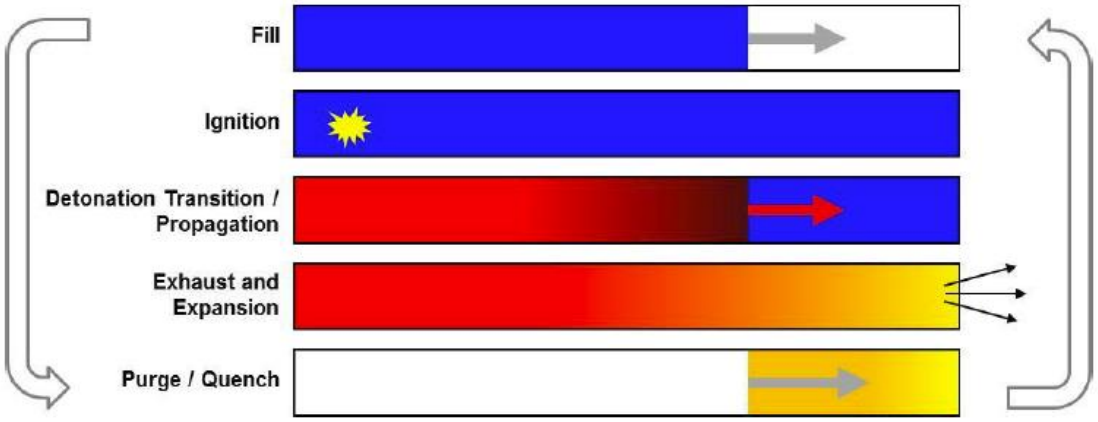

Figure 2.11: Pulse detonation engine (PDE) cycle [2.16].

The cyclic process of repeated ignition in PDE is a significant detriment; operation of PDE is typically limited to 10-100 Hz [2.17]. A significant fraction of losses associated with PDE were linked to the deflagration-to-detonation transition (DDT) process that occurred after every ignition within the device [2.15]. Despite this challenge, the first flight of a PDE powered aircraft occurred in 2008 [2.18-2.19].

2.2.4 Rotating Detonation Engine

The Rotating Detonation Engine (RDE), unlike PDE, continuously detonates reactants. RDE geometry is characterized by an annular combustor, Fig. 1.1. Reactants

are continuously fed in the axial direction, and one or more detonations propagate around the circumference of the annulus in the azimuthal direction [2.20]. RDEs operate in the range of 1-10 kHz; frequency is controlled by the number of detonation waves present, annulus circumference, and detonation wave speed [2.21].

Like PDE, the thermodynamic benefits associated with the traditional Hugoniot analysis are attainable in RDE. The simple design, compact reaction zone, and periodic heat addition process have contributed to the recent surge of efforts in developing RDE [2.22-2.24]. RDE geometry is flexible enough to accommodate both rocket [2.25–2.30] and air-breathing [2.22-2.23,2.31] applications.

In comparison to the standing detonation engine, OWDE, and PDE, the RDE flowfield is complex and highly coupled. A fundamental understanding of the structures and features of this flowfield are required to properly understand and implement RDE. This work exclusively focuses on improving this understanding.

2.3 Studies of the Rotating Detonation Engine Structure

The earliest progenitor of the RDE combustor can be traced to work performed by Voitsekhovskii in 1960 [2.32]. At the time Voitsekhovskii was uninterested in the propulsive aspects of detonation, and only sought to examine the detonation phenomenon. The combustor utilized in this early research is analogous to the modern Disk Rotating Detonation Engine (DRDE) [2.33-2.34]; reactants and products both flowed radially outwards from the core of Voitsekhovskii's device. Premixed reactants were injected via a slot injector, and the detonation transits were visualized.

Later that decade Nicholls et. al. examined a "Rotating Detonation Wave Rocket Motor" [2.27]. Their interests stemmed from a desire to improve the understanding of

detonation instabilities in liquid rocket combustors, and if possible, to implement these phenomena in a practical propulsive device. While they were unable to sustain detonation propagation, their insights undoubtedly aided in the design of future RDE.

2.3.1 Experimental

In 1980 Bykovskii and Mitrofanov investigated detonation propagation in an annular channel [2.35]. Figure 2.12 shows the flowfield associated with these detonations. Inclined detonation fronts are indicated by line segments BC and B'C' and propagate from left to right; reactant injection occurs at the top of the figure.

As observed by Bykovskii and Mitrofanov, the injection in the wake of wave BC is suppressed until point A, then resumes to form the fill region A-M'-C' prior to the subsequent wave arrival. An oblique shock is anchored on the detonation wave in order to yield equal pressures on both sides of the material interface E/E'.

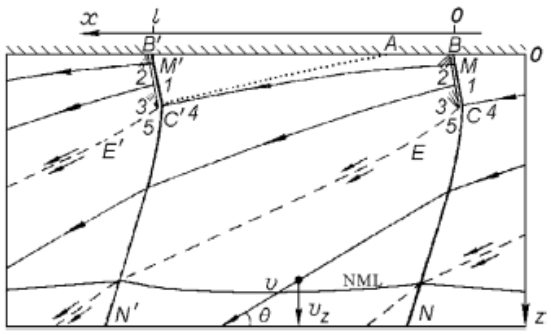

Figure 2.12: Detonation wave structure and flow in the coordinate system of a wave [2.35].

Assuming steady reactant inflow and wave speeds, the reactant fill height of BC and B'C' should be equal. Further insight into the detonation-oblique structure can be gleaned from the work by Dabora et. al. in the mid-1960's [2.36]. In their experiments a reactive layer of gas was separated from an inert gas by a thin membrane. Detonations were propagated into the reactive layer, and the membrane was destroyed by the detonation on comparable time scales; a visualization of one such transit is shown in Fig. 2.13.

Of particular interest is the material interface that forms between the detonation products and the shocked inert gases. The onset of a Kelvin-Helmholtz instability is observed just below the arrow indicating the interface, which is omitted from Bykovskii et. al.'s annotation. Sichel and Foster used the configuration presented by Dabora et. al. to estimate the pressure profile along the right wall in the wake of the detonation through the use of the method of characteristics [2.37]. In 2017 this approach was extended to the entirety of the simplified RDE flowfield by Fievisohn et. al. to estimate the reactant refresh profile, detonation inclination, and oblique shock shape [2.24].

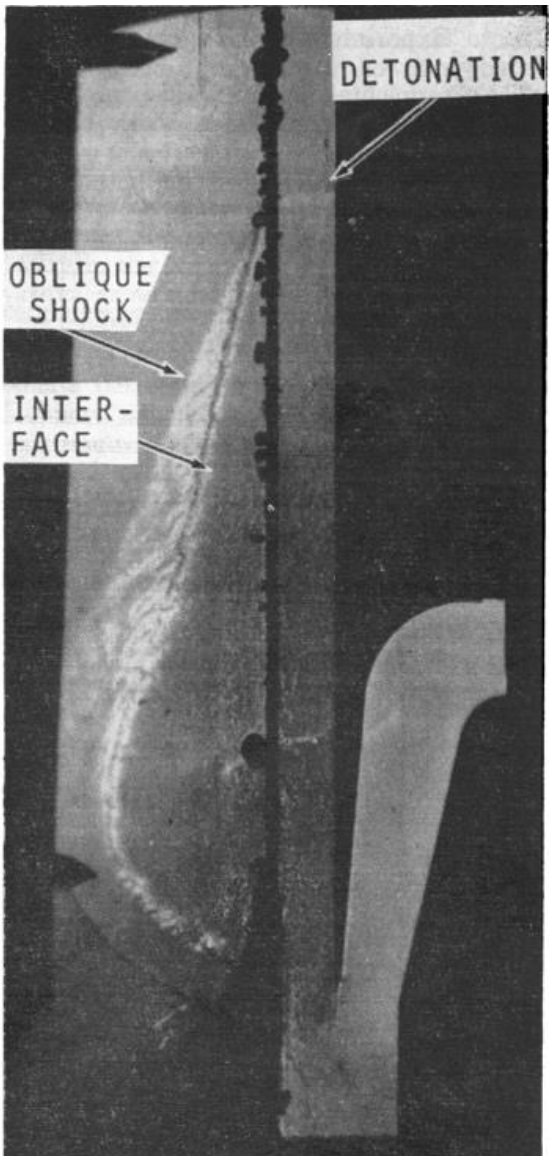

Figure 2.13: Typical spark photograph of an unquenched detonation [2.36].

Recent experimental investigations have continued to contribute to the understanding of RDE flowfield and structure. Detonations have been directly visualized in RDE through natural luminescence, chemiluminescence, and mid-infrared techniques [2.38-2.40]. Figure 2.14 shows a detonation wave propagating from right to left. Improvements in camera imaging are reflected in this image; the region of

heat release associated with detonation-based combustion is directly visualized as the bright zone immediately behind the wave front. Similarly, the oblique shock angle, material interface, and reflected shock (from the exit of the RDE) are noted. However, small scale structures, such as the expected transverse waves and triple points of a detonation cell, are lacking from these images.

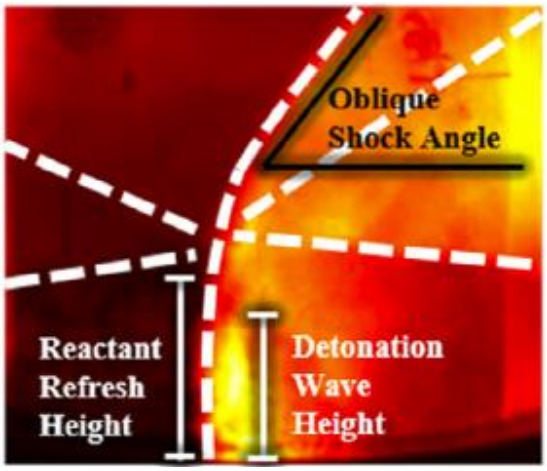

Figure 2.14: Instantaneous mid-infrared image of detonation wave propagated through RDE [2.40].

Chacon et. al. reduced the optical aberrations associated with the imaging of an annular combustor by developing a "racetrack" RDE [2.41]. In this configuration the RDE annulus was cut along the axial direction, and two straight segments were added. A typical image of detonation in this configuration is shown in Fig. 2.15. Chacon was able to distinguish combustion from the detonation wave as well as deflagration in the immediate wake and preceding the detonation wave. The presence of deflagration, as well as the irregular detonation shape, are indicators of poor mixing in RDE operation.

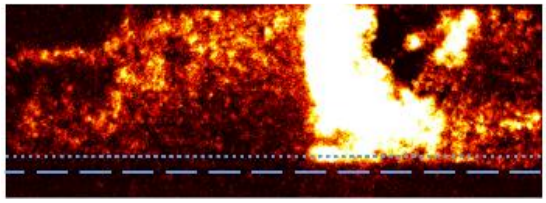

Figure 2.15: OH* chemiluminescence of detonation in "racetrack" RDE [2.41].

2.3.2 Computational

Numerical studies provided further insight into the structure of the RDE flowfield. Kailasanath and Schwer were able to model the annular RDE flowfield in a

two-dimensional and periodic domain to great detail [2.23, 2.42-2.43]. One such solution is shown in Fig. 2.16. The A) inclined detonation front, B) oblique shock, and G) reactant fill region agree qualitatively with the experimental observations.

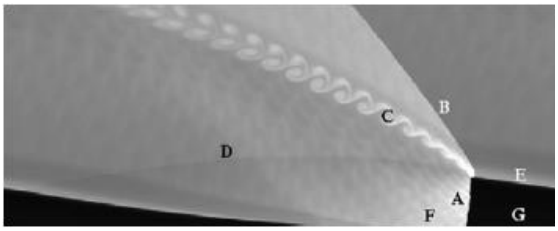

Figure 2.16: Temperature solution of an "unrolled" hydrogen-air RDE [2.23].

However, the computational solution in Fig. 2.16 also shows D) secondary shock structures and C) the development of a well-defined Kelvin-Helmholtz instability. The smooth and uniform flow structures and regions are the result, in part, of the continuous inflow condition. Paxson uses a similar simplification in his model of detonation in RDE [2.45], Fig. 2.17. In both cases the simplification reduced the challenge of modeling the mixing and detonation time scales, as well as the specificity of selecting a single injector scheme.

An additional flow feature common to these simulations is the protrusion of the oblique shock ahead of the incident detonation front. Insight into this phenomenon can be drawn from the work of Houim et. al., who simulated a layered detonation configuration reminiscent of the experiments of Dabora et. al. in the 1960s [2.46]. In their simulations the temperature of the inert reactant confining the reactant layer was varied, with two cases shown in Fig. 2.18.

Increase in inert temperature similarly increases sound speed; at some critical value the disturbance caused by the detonation races ahead within the

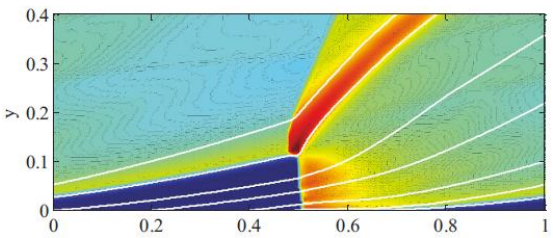

Figure 2.17: Computed contours of temperature throughout the annulus of an "unwrapped", steady RDE [2.45].

inert gas. The resulting disturbance propagates down into the reactant layer and is transmitted as an oblique shock back towards the detonation wave. In the case of detonation propagation, Houim et. al. found this behavior to be critically important.

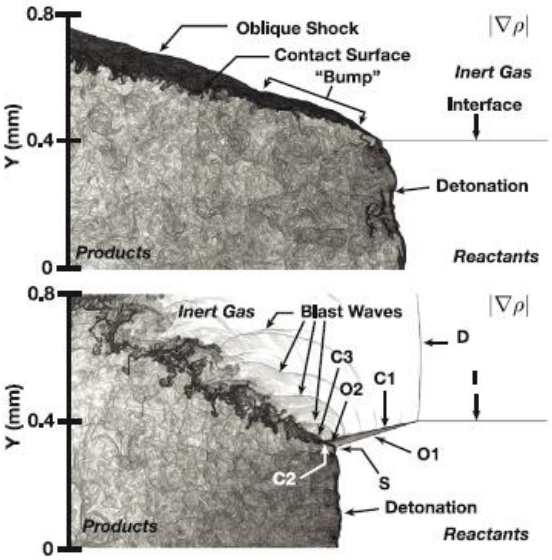

Figure 2.18: Numerical schlieren of detonation bound by high acoustic impedance (top) and low acoustic impedance (bottom) inert gas [2.46].

Transverse waves critical to the detonation survival reflect strongly off of both a low temperature (high acoustic impedance) inert gas boundary and a high temperature (low acoustic impedance) inert gas boundary due to the induced oblique shock. Within certain temperature ranges, however, either no or weak reflection of transverse waves occurs, leading to an extinction of the horizontally propagating detonation wave [2.46]. In RDE the acoustic impedance of the confining gas is naturally low due to the elevated product temperature.

Despite the qualitative agreement between the experimental and computational works, it is apparent that there is a discrepancy between the two datasets; experiments lack the resolution necessary to validate numerical predictions, and computational efforts often limit the inclusion of characteristics, such as mixing and deflagration in the contact region between fresh reactants and products. In this work the transit of a detonation into a configuration analogous to RDE will be experimentally investigated. The resulting flow structures and features will be examined for insight into RDE

operation; the collected data will be used to draw conclusions on detonation propagation characteristics and for use in future computational validation efforts.

2.4 References

[2.1] W. Fickett and W. C. Davis, *Detonation Theory and Experiment* (Dover Publications, Inc., New York, 2000).

[2.2] B. V. Voitsekhovskii, V. V. Mitrofanov, and M.E. Topchiyan. Structure of the detonation front in gases (survey). *Combustion, Explosion, and Shock Waves*, 5(3):267-273, 1969.

[2.3] J. S. Lee, *The Detonation Phenomenon* (Cambridge University Press, New York, 2008).

[2.4] A. I. Gavrikov, A. A. Efimenko, and S. B. Dorofeev. A Model for Detonation Cell Size Prediction from Chemical Kinetics. Combustion and Flame 120(1):19-33, 2000.

[2.5] K. I. Shchelkin and Y. K. Troshin, *Gasdynamics of Combustion* (Mono Book Corporation, Baltimore, 1965).

[2.6] H. D. Ng. The effect of chemical reaction kinetics on the structure of gaseous detonations. Ph.D. Thesis, McGill University, 2005.

[2.7] M. Kaneshige and J.E. Shepherd. Detonation database. Technical Report FM97-8, GALCIT, July 1997 (http://www.galcit.caltech.edu/detn_db/html/).

[2.8] R. Knystautas, C. Guiaro, J. H. S. Lee, and A. Sulmistras. Measurements of Cell Size in Hydrocarbon-Air Mixtures and Predictions of Critical Tube Diameter, Critical Initiation Energy, and Detonability Limits. In *Dynamics of Shock Waves, Explosions, and Detonations*, ed. J. R. Bowen, N. Manson, A. K. Oppenheim, and R.I. Soloukhin (1985).

[2.9] W. H. Sargent and R. A. Gross. Detonation Wave Hypersonic Ramjet. *American Rocket Science Journal*, 30(6), 1960.

[2.10] Y. B Zel'dovich. To the Question of Energy Use of Detonation Combustion. *Zhurnal Teknicheskoi Fiziki*, 10(17):1453-1461, 1940.

[2.11] E. Wintenberger and J. E. Shepherd. Stagnation Hugoniot Analysis for Steady Combustion Waves in Propulsion Systems. *Journal of Propulsion and Power*, 22(4), 2006.

[2.12] C. Li, K. Kailasanath, and E. S. Oran. Detonation structures behind oblique shocks. *Physics of Fluids*, 6(4):1600-1611, 1994.

[2.13] G. P. Menees, H. G. Adelman, J. Cambier, and J. V. Bowles. Wave combustors for trans-atmospheric vehicles. *Journal of Propulsion and Power*, 8(3):709-713, 1992.

[2.14] D. Li, K. Kailasanath, E. S Oran, A. M. Landsberg, and J. P Boris. Dynamics of oblique detonations in ram accelerators. *Shock Waves*, 5(1):97-101, 1995.

[2.15] K. Kailasanath. Research on Pulse Detonation Combustion Systems: A Status Report. In *47th AIAA Aerospace Sciences Meeting*, AIAA Paper 2009-631, 2009.

[2.16] A. St. George, R. Driscoll, V. Anand, S. Randall, D. Munday, and E. J. Gutmark. Development of a Rotating Detonation Engine Facility at the University of Cincinnati. In *53rd AIAA Aerospace Sciences Meeting*, AIAA Paper 2015-0635, 2015.

[2.17] G. D. Roy, S. M. Frolov, A. A. Borisov, and D. W. Netzer. Pulse detonation propulsion: challenges, current status, and future perspective. *Progress in Energy and Combustion Science*, 30(6):545-672, 2004.

[2.18] P. Wolanski. Detonative propulsion. *Proceedings of the Combustion Institute*, 34(1):125-158, 2013.

[2.19] A. Naples. Recent progress in detonation at air force research labs. In *International Workshop on Detonation for Propulsion*, Busan, Korea, 2011.

[2.20] F. A. Bykovskii, S. A. Zhdan, and E. F. Vedernikov. Continuous Spin Detonations. *Journal of Propulsion and Power*, 22(6):1204-1216, 2006.

[2.21] F. K. Lu and E. M. Braun. Rotating Detonation Wave Propulsion: Experimental Challenged, Modeling, and Engine Concepts. *Journal of Propulsion and Power*, 30(5):1125-1142, 2014.

[2.22] M. Hishida, T. Fujiwara, and P. Wolanski. Fundamentals of rotating detonations. *Shock Waves* 19(1):1-10, 2009.

[2.23] D. Schwer and K. Kailasanath. Numerical investigation of the physics of rotating-detonation-engines. *Proceedings of the Combustion Institute*, 33(2):2195-2202, 2011.

[2.24] R. T. Fievisohn and K. H. Yu. Steady-State Analysis of Rotating Detonation Engine Flowfields with the Method of Characteristics. *Journal of Propulsion and Power*, 33(1):89-99, 2017.

[2.25] F. K. Lu, R. Miller, M. R. Nalim, and K. H. Yu. Introduction: Special Section on Pressure Gain Combustion. *Journal of Propulsion and Power*, 33(1):16, 2017.

[2.26] R. M. Clayton and R. S. Rogero. Experimental Measurements on a Rotating Detonation-Like Wave Observed During Liquid Rocket Resonant Combustion. Jet Propulsion Laboratory Technical Report No. 32-788, 1965.

[2.27] J. A. Nicholls, R. E. Cullen, and K. W. Ragland. Feasibility studies of a rotating detonation wave rocket motor. *Journal of Spacecraft and Rockets*, 3(6):893-898, 1966.

[2.28] T. C. Adamson Jr. and G. R. Olsson. Performance Analysis of a Rotating Detonation Wave Rocket Engine. *Astronautica Acta*, 13(4):405-415, 1967.

[2.29] P. I. Shen and T. C. Adamson Jr. Theoretical Analysis of a Rotating Two-Phase Detonation in Liquid Rocket Motors. *Astronautica Acta*, 17(4):715-728, 1972.

[2.30] J. Kindracki, P. Wolanski, and Z. Gut. Experimental research on the rotating detonation in gaseous fuels-oxygen mixtures. *Shock Waves*, 21(2):75:84, 2011.

[2.31] F. A. Bykovskii and E.F. Vedernikov. Continuous detonation combustion of an annular gas-mixture layer. *Combustion, Explosion and Shock Waves*, 32(5):489:491, 1996.

[2.32] B. V. Voitsekhovskii. Maintained detonations. *Soviet Physics Doklady*, 4(1):1207, 1960.

[2.33] R. Huff, M. D. Polanka, M. J. McClearn, F. R. Schauer, M. Fotia, and J. L. Hoke. A Disk Rotating Detonation Engine Part 1: Design and Buildup. In *2018 AIAA Aerospace Sciences Meeting*, AIAA Paper 2018-0633, 2018.

[2.34] M. J. McClearn, F. R. Schauer, R. Huff, M. D. Polanka, J. L. Hoke, and M. Fotia. A Disk Rotating Detonation Engine Part 2: Operation. In *2018 AIAA Aerospace Sciences Meeting*, AIAA Paper 2018-1607, 2018.

[2.35] F. A. Bykovskii and V. V. Mitrofanov. Detonation combustion of a gas mixture in a cylindrical chamber. *Combustion, Explosion and Shock Waves*, 16(5):570-578, 1980.

[2.36] E. K. Dabora, J. A. Nicholls, and R. B. Morrison. The influence of a compressible boundary on the propagation of gaseous detonation. *Symposium (International) on Combustion*, 10(1):817-830, 1965.

[2.37] M. Sichel and J. C. Foster. The ground impulse generated by a plane fuel-air explosion with side relief. *Acta Astronautica*, 6(3-4):243-256, 1979.

[2.38] A. Naples, J. Hoke, J. Karnesky, and F. Schauer. Flowfield Characterization of a Rotating Detonation Engine. In *51t AIAA Aerospace Sciences Meeting*, AIAA Paper 2013-0278, 2013.

[2.39] B. A. Rankin, D. R. Richardson, A. W. Caswell, A. Naples, J. L. Hoke, and F. R. Schauer. Imaging of OH* Chemiluminescence in an Optically Accessible

Nonpremixed Rotating Detonation Engine. In *53rd AIAA Aerospace Sciences Meeting*, AIAA Paper 2015-1604, 2015.

[2.40] B. A. Rankin and F. R. Schauer. Investigation of the structure of detonation waves in a non-premixed hydrogen-air rotating detonation engine using mid-infrared imaging. *Proceedings of the Combustion Institute*, 37(3):3479-3486, 2019.

[2.41] F. Chacon and M. Gamba. Study of Parasitic Combustion in an Optically Accessible Continuous Wave Rotating Detonation Engine. In *2019 AIAA Aerospace Sciences Meeting*, AIAA Paper 2019-0473, 2019.

[2.42] D. Schwer and K. Kailasanath. Feedback into Mixture Plenums in Rotating Detonation Engines. In *50th AIAA Aerospace Sciences Meeting*, AIAA Paper 2012-0617, Jan. 2012.

[2.43] D. Schwer and K. Kailasanath. Fluid dynamics of rotating detonation engines with hydrogen and hydrocarbon fuels. *Proceedings of the Combustion Institute*, 34(2):1991-1998, 2013.

[2.44] K. Wu, S. Zhang, M. Luan, and J. P. Wang. Effects of flow-field structures on the stability of rotating detonation ramjet engine. *Acta Astronautica*, 168(1):174-181, 2020.

[2.45] D. E. Paxson. Numerical Analysis of a Rotating Detonation Engine in the Relative Reference Frame. In *52nd Aerospace Sciences Meeting*, AIAA Paper 2014-0284, 2014.

[2.46] R. W. Houim and R. T Fievisohn. The influence of acoustic impedance on gaseous layered detonations bounded by an inert gas. *Combustion and Flame*, 179(1):185-198, 2017.

Chapter 3: Structure of H_2 Detonations

The contents of this chapter examine the features of H_2-O_2 detonations in the LMDE experimental facility (Appendix B). The text is adapted from the following peer reviewed proceedings of the 2017 International Colloquium on the Dynamics of Explosions and Reactive Systems (ICDERS):

> J. R. Burr and K. H. Yu. Detonation Propagation in a Linear Channel with Discrete Injectors and Side Relief. In *26th International Colloquium on the Dynamics of Explosions and Reactive Systems*, ICDERS Paper 2017-1107, Aug. 2017.

3.1 Introduction

The potential thermodynamic gains associated with pressure gain combustion cycles have resulted in a steady rise in interest in combustors like the pulse detonation engine (PDE) and rotating detonation engine (RDE) [3.1-3.3]. While the PDE operates in a manner that requires multiple ignition events and transitions of deflagrations to detonations, the RDE is the realization of a continuously propagating detonation about the circumference of an annular channel [3.1]. Reactants are supplied axially into the annular channel and continuously refresh the azimuthally propagating detonation structure [3.2]. It may also be possible to develop more practical engine designs by integrating an aerospike nozzle with the annular shape of an RDE combustor, thus

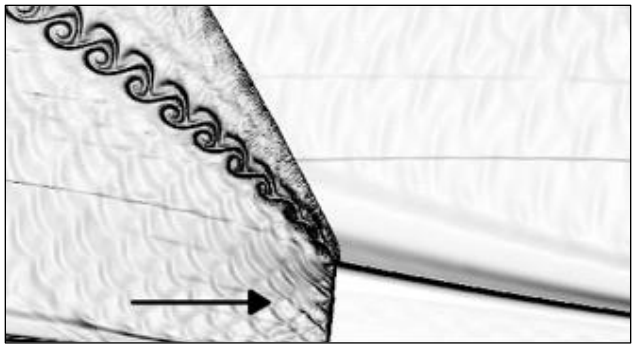

Figure 3.1: Numerical schlieren of the RDE [3.9]. Detonation propagates from left to right.

substantially reducing the thruster weight and length [3.4].

A number of experimental and computational studies have helped to shape the understanding of RDE operation. Voitsekhovskii (1959) reported an experimental facility similar to the modern RDE for studying the propagation of a detonation wave [3.5]. Also, Sommers & Morrison (1962), Dabora et al. (1965), and Sichel & Foster (1979) examined the propagation of a detonation wave in a thin layer of reactive gas bound by an inert gas [3.6-3.8]. More recent numerical studies on the RDE have produced more insightful visualizations of the RDE flowfield [3.9], and have influenced subsequent approaches that quantify the global thermodynamic efficiency of the RDE cycle [3.10]. A host of recent investigations have sought to improve RDE understanding in ways that range from providing insight into flow physics, to integration for flight applications [3.11-3.13].

Many challenges still remain before the practical implementation of an RDE system in which the potential benefits can be realized; unwanted deflagration burning, injector mixing, heat transfer losses, and suitable high temperature material are all important issues within the RDE that have yet to be fully addressed [3.3]. Fundamental experimental studies are needed for the RDE that can fully investigate relevant flow and chemistry features to better understand these loss mechanisms and operating conditions. Numerically, Schwer & Kailasanath [3.9, 3.11], and Davidenko, Gökalp & Kudryavtsev [3.13] have studied the fully three-dimensional detonation structure in such RDE models. No experimental data with such details are yet available for comparison or validation of detailed simulation results.

The objectives of this study are to experimentally investigate the nature of a detonation wave propagating across transversely injected reactants in a canonical channel set-up simulating an unwrapped RDE configuration and to provide detailed experimental data that can not only increase the fundamental understanding of the RDE flow structure but can also be used for CFD validation. The approach is to simplify the experimental environment by examining the transient propagation of a detonation wave in cross-flowing reactants through a novel linear channel facility instead of the annular RDE arrangement. Studying the detonation wave propagation in a straight channel allows for the use of high-quality optical measurements that are much more difficult in a curved annulus.

3.2 Experimental Setup

The Linear Model Detonation Engine (LMDE) facility is shown in Fig. 3.2, with dimensions normalized by recessed tube diameter **d** and channel width (Y direction) of 3**d**. Design of the LMDE integrates elements of the AFRL's 6-inch RDE [3.14] and the NRL's premixed microinjection system [3.15]. In the current configuration the non-crosshatched regions of Fig. 3.2 (for $Z \geq 0$) represent optically accessible regions of the combustor that allow for imaging of evolving flow structures. Tubes used for reactant injection ($Z < 0$) are not visualized in the current LMDE configuration.

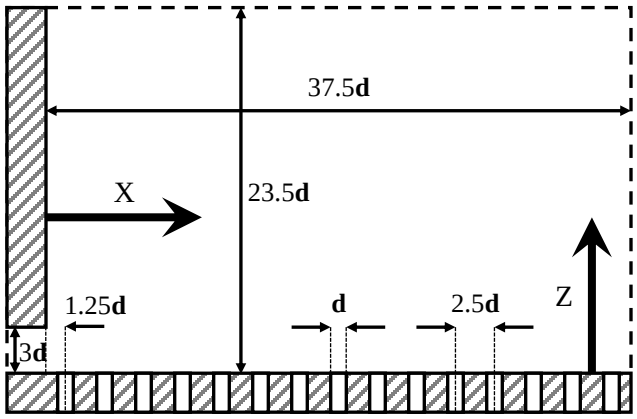

Figure 3.2: Cross-section view of the LMDE test section. Dimensions normalized by diameter of recessed pre-mixing tube (**d** = 2.54 mm).

Confinement of reactant species is provided on the sides by the quartz windows and below by the injection plane.

Reactant flow propagates in the Z direction, simulating RDE inflow. Fuel and oxidizer species are partially premixed within each of the fifteen recessed cylindrical tubes (L/D of 11.25) at a depth of 10d relative to the bottom of the LMDE channel as illustrated in Fig. 3.2. Independent solenoid control for reactant species allows for control over the height of the partially premixed reactant layer just prior to detonation transit.

A pre-detonator with internal diameter of 4.3**d** and L/D of 42 generates a detonation that propagates in the positive X direction into the reactive cross-flow within the LMDE. A transition piece converts the circular cross-section to a square one with side measuring 3**d**. The pre-detonator operates using a stoichiometric mixture of hydrogen and oxygen, with fill times restricted to mitigate contamination in the LMDE. An electric spark from an automotive ignition system using an iridium tipped spark plug initiates combustion. Dynamic pressure transducers, sampled at 750 kHz with a National Instruments cDAQ-9188 system, positioned 65**d** and 25**d** upstream of the LMDE measure the detonation speed as 2830 m/s.

3.3 Experimental Results and Discussion

Initial experiments were conducted without reactive cross-flow to establish baseline behavior of the pre-detonator discharge into the LMDE facility. In these experiments the detonation transitions to a strong blast wave upon entering the LMDE channel, Fig. 3.3a. Pre-detonator discharge occurs from left to right. An incident curved shock structure leads the material interface between pre-detonator exhaust and the gas

compressed by the incident shock. Between the incident shock and the material interface, shocklets are observed anchored to the recessed tubes used for reactant injection.

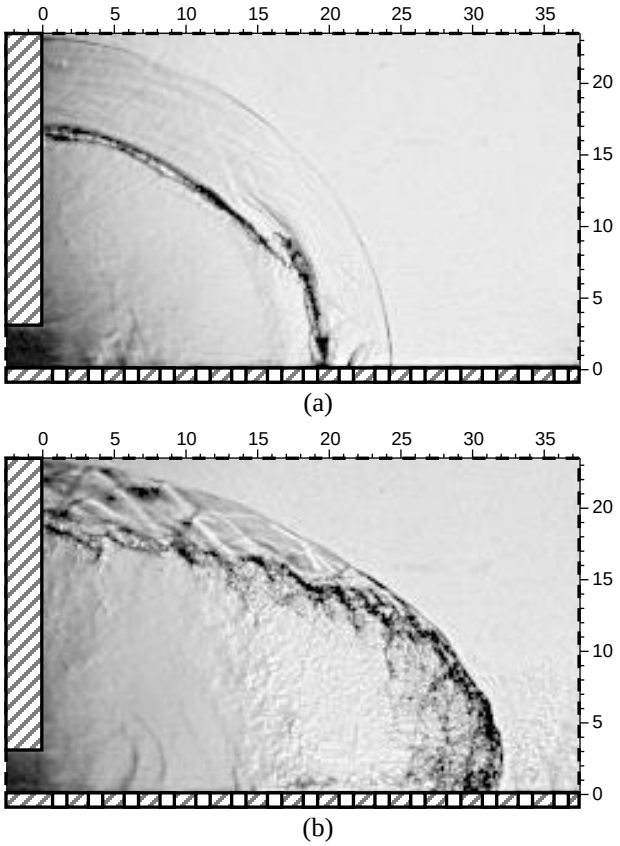

Figure 3.3: Schlieren image of pre-detonator discharge without cross-flow (a) and detonation propagation in cross-flow of hydrogen-oxygen mixture ($\phi = 1.0$) (b).

Experiments conducted with cross-flow present yielded successful detonations, Fig. 3.3b. The reactive cross-flow is visualized to the right of the detonation structure with a height of 8-9**d**. Variation in crossflow height is piecewise sinusoidal and due to the discrete injection of reactants; cross-flow height is greatest directly above injection locations and shorter elsewhere. The cross-flow shape gives way to the shape of the material interface, which is distinct from the incident shock at X/**d** of zero. The nonuniformity of the initial cross-flow likely accelerates the growth of the Richtmyer-Meshkov instability that forms after the detonation transit. The incident shock and material interface curve to meet the detonation structure near an X/**d** of 31. The region between these two structures is populated by weak shock and expansion waves, likely the result of flow deflection off of the irregularly shaped material interface.

The detonation structure is expressed with significant curvature with the leading edge positioned 2-3**d** above the base of the LMDE. Reactant injection is performed with an evolving jet to replicate the flow conditions within an RDE – immediately after detonation transit inflow is impeded by pressure gain, but resumes as unchoked injection as the pressure falls. For different species, in this case hydrogen and oxygen, the inflow velocities differ, resulting in a non-uniform distribution of reactant species in the direction of jet propagation. In addition, the time-varying velocities create time-varying degrees of mixedness between the species. The leading edge of the detonation indicates the relative maximum in cross-flow detonability as a function of these parameters.

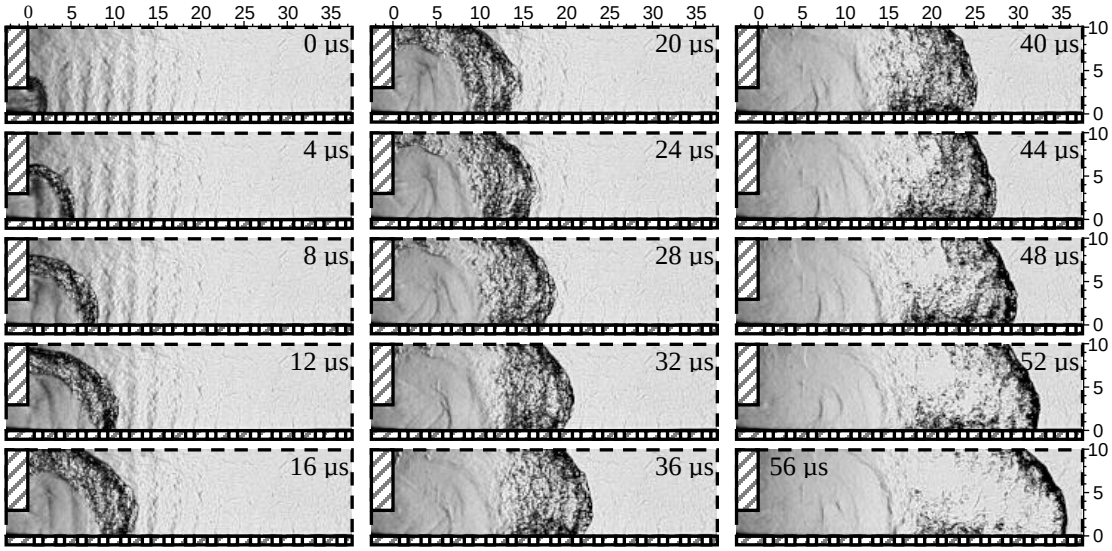

Figure 3.4: Schlieren images of detonation propagation in cross-flow of hydrogen-oxygen mixture (ϕ = 1.0). The horizontal and vertical scales are the non-dimensional position in the channel X/d and Z/d, respectively.

The detonation transit is examined temporally to investigate variation in propagation behavior with distance from ignition by the pre-detonator, Fig. 3.4. Images were acquired at 500 kHz, with images shown in increments of 4 µs. The resulting estimates in detonation velocity, Fig. 3.5, show three distinct regimes of detonation

propagation – diffraction, reduced velocity, and acceleration – and indicate the detonation propagation has yet to reach a steady behavior.

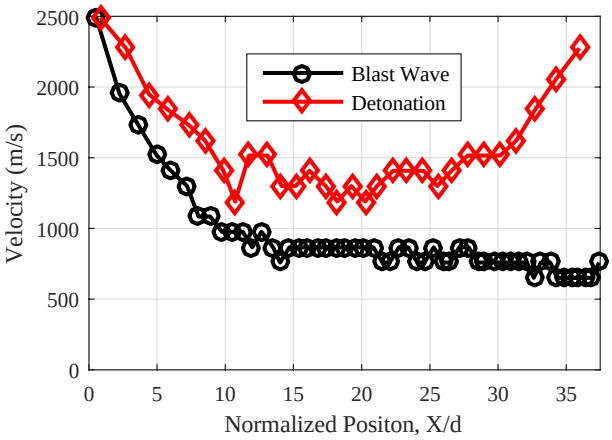

Figure 3.5: Blast wave and detonation velocities within LMDE channel based off of schlieren images acquired at 500 kHz.

Within the pre-detonator the detonation wave is confined on all sides by solid walls; upon exiting the pre-detonator the detonation loses confinement from above and similarly loses triple points to the gaseous confinement layer. The result is a sudden arrest in forward motion of the detonation wave in the first 12 μs of propagation, and mimics the behavior of the blast wave. In the next 22 μs of propagation the detonation moves at a significantly reduced velocity – nearly 50% of the incident detonation speed. In the corresponding schlieren images the detonation structure is curved with a pronounced bulge; the wave structure intersects the base of the LMDE at an oblique angle. The combination of poor mixing, oblique shock angle, and low speed near the base of the LMDE indicate the cross-flow is likely not detonating at this height. The final region of propagation is characterized by a sudden acceleration of the detonation structure to speeds matching that of the incident detonation. In addition, while the bulge of the detonation front still exists, the intersection of the structure with the base of the LMDE occurs at an angle closer to the normal, signifying a greater pressure rise in this region. A greater percentage of the cross-flow reactants are likely detonating in this regime.

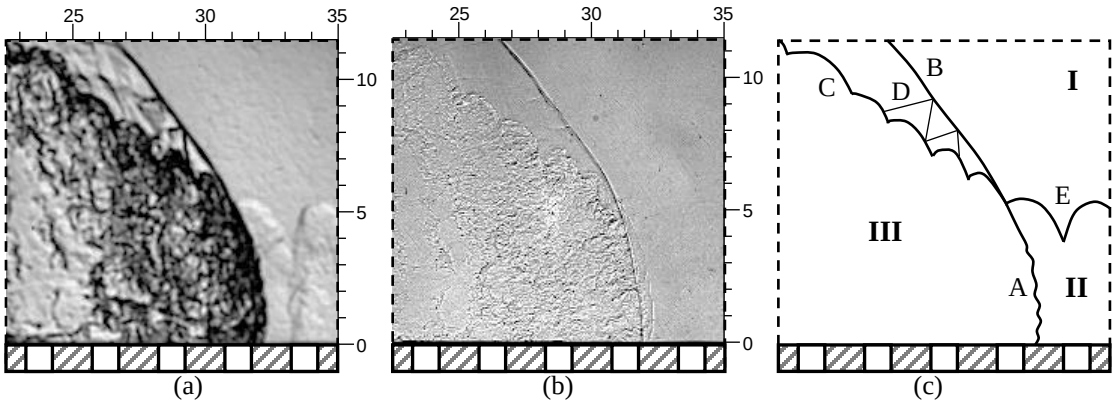

Figure 3.6: Schlieren (a), shadowgraph (b), and annotated illustration (c) of detonation in cross-flow of hydrogen-oxygen mixture ($\phi = 0.8$).

The detonation transit is imaged in the region of sudden acceleration at a higher resolution to observe flow features, Fig. 3.6. Key flow regions are the background confinement gas (I), the reactant cross-flow (II), and the combusted products (III). Structures include the detonation front (A), an oblique shock (B), the material interface between combustion products and shocked background gas (C), shocks and expansion fans reflecting off of the material interface (D), and the material interface between the cross-flow and the background gas (E). The irregularities in the detonation front appear to be cellular structures, although the mechanism that maintains them in the LMDE configuration requires further investigation.

3.4 Concluding Remarks

An experimental study is in progress to study detonation waves propagating across an array of reactant jets discharged into a narrow channel. The principal objective was to gain better understanding of the fundamental flow structure and the physical processes that occur inside an RDE combustor. Preliminary results indicate the detonation propagates as a curved structure with peak propagation occurring in the

middle of the cross-flow and is likely a function of inflow velocity and mixing characteristics. Three regimes of propagation have been identified – diffraction, reduced velocity, and acceleration – with images acquired during the acceleration regime to visualize key detonation structures.

In this paper, we present the results from one of the cases where partially-premixed hydrogen-oxygen jets are injected into the oxygen-enriched air background. Since the partially-premixed reactant jets evolve inside the channel, they also mix with the background gas resulting in highly non-uniform reactant mixture along the jet height. At the same time, there are discretely spaced reactant jets along the wave propagation direction, possibly creating a discontinuous pathway of detonable mixture. As a result, even in such a simple configuration as that considered in this paper, the flowfield becomes quite complicated.

The wave and flow structures were characterized using two simultaneously applied high-speed visualization techniques and dynamic pressure measurements. It was shown that the detonation wave speed was not constant across the channel passage, suggesting the wave was still in the transient stage of development. Furthermore, the wave speed fluctuated substantially, suggesting possible effects of nonuniform reactant mixture. The present results highlighted that the mixing within the reactive mixture as well as the mixing between the reactant jets and the previous cycle products should play a critical role for sustaining and stabilizing detonation wave propagation inside an RDE combustor.

3.5 Acknowledgments

This research was supported by the Air Force Office of Scientific Research with Dr. Chiping Li as the program manager.

3.6 References

[3.1] G. D. Roy, S. M. Frolov, A. A. Borisov, and D. W. Netzer. Pulse detonation propulsion: challenges, current status, and future perspective. *Progress in Energy and Combustion Science*, 30(6):545-672, 2004.

[3.2] F. A. Bykovskii, S. A. Zhdan, and E. F. Vedernikov. Continuous Spin Detonations. *Journal of Propulsion and Power*, 22(6):1204-1216, 2006.

[3.3] F. K. Lu and E. M. Braun. Rotating Detonation Wave Propulsion: Experimental Challenges, Modeling, and Engine Concepts. *Journal of Propulsion and Power*, 30(5):1125-1142, 2014.

[3.4] F. Falempin, E. Daniau, F. Getin, F. Bykovskii, and S. Zhdan. Toward a Continuous Detonation Wave Rocket Engine Demonstrator. In *14th AIAA/AHI Space Planes and Hypersonic Systems and Technologies Conference*, AIAA Paper 2006-7956, Nov. 2006.

[3.5] B. V. Voitsekhovsky. Stationary detonation. *Reports of USSR Academy of Sciences*, 129(6):1254-1256, 1959.

[3.6] W. P. Sommers and R. B. Morrison. Simulation of Condensed-Explosive Detonation Phenomena with Gases. *The Physics of Fluids*, 5:241, 1962.

[3.7] E. K. Dabora, J. A. Nicholls, and R. B. Morrison. The influence of a compressible boundary on the propagation of gaseous detonation. *Symposium (International) on Combustion*, 10(1):817-830, 1965.

[3.8] M. Sichel and J. C. Foster. The ground impulse generated by a plane fuel-air explosion with side relief. *Acta Astronautica*, 6(3-4):243-256, 1979.

[3.9] K. Kailasanath. Rotating Detonation Engine Research at NRL. In *2013 International Workshop for Detonations in Propulsion*, July 2013.

[3.10] C. A. Nordeen, D. Schwer, F. Schauer, J. Hoke, T. Barber, and B. Cetegen. Thermodynamic model of a rotating detonation engine. *Combustion, Explosion, and Shock Waves*, 50:568-577, 2014.

[3.11] D. Schwer and K. Kailasanath. Numerical investigation of the physics of rotating-detonation-engines. *Proceedings of the Combustion Institute*, 33(2):2195-2202, 2011.

[3.12] L. Thomas, F. Schauer, J. Hoke, and A. Naples. Buildup and Operation of a Rotating Detonation Engine. In *49th AIAA Aerospace Sciences Meeting*, AIAA Paper 2011-602, Jan. 2011.

[3.13] D. M. Davidenko, I. Gokalp, and A. N. Kurdrvavtsev. Numerical Simulation of the Continuous Rotating Hydrogen-Oxygen Detonation with a Detailed Chemical Mechanism. In *West-East High Speed Flow Field Conference*, Nov. 2007.

[3.14] J. C. Shank. Development and Testing of a Rotating Detonation Engine Run on Hydrogen and Air. MS thesis, Air Force Institute of Technology, 2012.

[3.15] D. Schwer and K. Kailasanath. Feedback into Mixture Plenums in Rotating Detonation Engines. In *50th AIAA Aerospace Sciences Meeting*, AIAA Paper 2012-0617, Jan. 2012.

Chapter 4: Role of Mixing in C_2H_4 Detonations

The contents of this chapter examine the features of C_2H_4-O_2 detonations in the LMDE experimental facility (Appendix B). The text is adapted from the following peer reviewed proceedings of the 2018 International Symposium on Combustion and subsequent journal publication:

> J. R. Burr and K. H. Yu. Experimental characterization of RDE combustor flowfield using linear channel. *Proceedings of the Combustion Institute*, 37(3):3471-3478, 2019.

4.1 Abstract

An experimental study was conducted to characterize fundamental behavior of detonation waves propagating across an array of reactant jets inside a narrow channel, which simulated an unwrapped rotating detonation engine (RDE) configuration. Several key flow features in an ethylene-oxygen combustor were explored by sending detonation waves across reactant jets entering into cold bounding gas as well as hot combustion products. In this setup, ethylene and oxygen were injected separately into each recessed injector tube, while a total of 15 injectors were used to establish a partially premixed reactant jet array. The results revealed various details of transient flowfield, including a complex detonation wave front leading a curved oblique shock wave, the unsteady production of transverse waves at the edge of the reactant jets, and the onset of suppressed reactant jets re-entering the combustor following a detonation wave passage. The visualization images showed a complex, multidimensional, and highly irregular detonation wave front. It appeared non-uniform mixing of reactant jets

lead to dynamic transverse wave structure. The refreshed reactant jets evolving in the wake of the detonation wave were severely distorted, indicating the effect of dynamic flowfield and rapid pressure change. The results suggest that the mixing between the fuel and oxidizer, as well as the mixing between the fresh reactants and the background products, should affect the stability of the RDE combustor processes.

4.2 Introduction

Recently, there has been a renewed interest in developing rotating detonation engines (RDE) as an alternative combustor concept [4.1–4.3]. It is possible to implement RDEs on both rocket [4.4–4.9] and air-breathing [4.1,4.2,4.10] applications. RDE has a detonation-based thermodynamic cycle, which can provide thermodynamic efficiency improvements over the Brayton-cycle engines for certain applications [4.11–4.14]. Moreover, possible system benefits stemming from the simple design, compact reaction zone, and periodic cyclic process make the potential use of RDE more interesting. The renewed interest appears to be driven by increasing demand for greater fuel economy and recent developments in related technology areas such as high-temperature materials and additive manufacturing.

In RDE a detonation wave propagates continuously in the azimuthal direction around an annular or cylindrical chamber. Reactants are steadily fed from one end of the annulus/cylinder along the axial direction [4.15]. The nature of the waves is affected by the local chemical composition as well as fluid mechanical and thermodynamic properties of the local mixture, which determine periodic formation of detonation or blast wave fronts [4.16, 4.17]. While there have been a plenty of fundamental and

applied research activities involving RDE [4.18, 4.19], there is still a lack of high-quality experimental data for visualizing the flowfield.

This study is motivated by the desire to provide better characterization of the RDE-relevant flowfield by building a linear model of the RDE combustor. By using a canonical configuration containing the essence of the RDE flowfield, it was expected that we can better visualize the detonation wave structure interacting with reactant flows under controlled conditions. Since the reactants are injected from the base of the channel just before the detonation wave arrival, there may not have been sufficient time to create uniform homogeneous mixture inside the channel. This can set up periodically varying mixture composition along the wave path downstream.

The purpose of this work was to obtain detailed information on the fundamental flow structures associated with a detonation wave that propagates inside a narrow open channel containing transversely flowing reactant jets. It was the intention of this experiment to simulate only the essence of the RDE geometry, excluding the curvature effects of the annulus. We focused our efforts on investigating the interaction between the detonation wave propagating along the channel and the reactant jets flowing orthogonally to the detonation wave. We hope the simplified combustor configuration allows us to obtain better understanding of the physics of the RDE flowfields by being able to focus our attention on the detonation wave-flowfield interaction inside a narrow open channel.

4.3 Experimental Approach

Experiments were performed in the Linear Model Detonation Engine (LMDE) combustor, shown in Fig. 4.1. Conditions generated by this facility simulate the

canonical flowfield encountered in the RDE; a detonation propagates transversely through discretely spaced reactant jets. Design of the LMDE integrated elements of the AFRL's 6-inch RDE [4.20] and the NRL's premixed microinjection system [4.2] into a simplified linear facility.

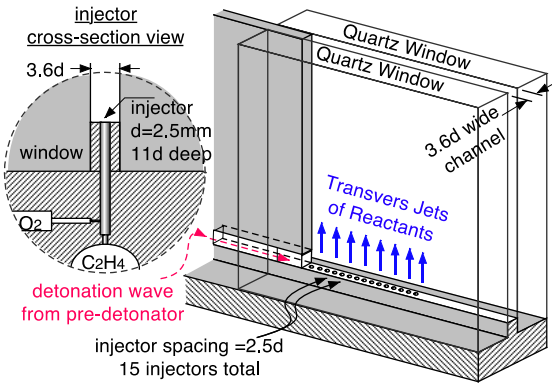

Figure 4.1: Isometric view of the LMDE combustor with cutaway of injector geometry.

The annulus walls of the RDE are replaced with planar, optically transparent quartz windows in the LMDE combustor. These windows allowed for use of one or more Phantom v2512 cameras in imaging the flowfield. Ethylene and oxygen reactants were injected into the LMDE through 15 recessed cylinders, each with a diameter **d** = 2.54 mm. Upon entry into the channel reactants are only partially mixed in order to reduce injector tube length and to replicate behavior of practical RDE injection geometries. Dimensions in subsequent figures are normalized by the tube diameter. Additional details regarding experimental setup are available [4.16].

Figure 4.2 shows the dynamic pressure measurements of a typical LMDE test that includes two pre-detonator ignitions spaced 110 ms apart; Figure 4.2(a) shows the test in its entirety, while Fig. 4.2(b)–(d) focus on subsets of the test to emphasize important features. A detonation transit of a sensor is defined as the time when the signal derivative reaches a local maximum; in the case of dynamic pressure sensor #1 the two transit times are labeled as τ_1 and τ_2 throughout Fig. 4.2. The pre-detonator wave speed for a given ignition event was estimated from the delay in transit time be- tween the

two sensors and known sensor spacing. Sensor #1 and sensor #2 are located 65**d** and 25**d** upstream of the LMDE reactant cross-flow, respectively. For the signals in Fig. 4.2 , the first wave speed was measured as 3.0 ± 0.2 km/s, and the second wave speed was measured as 1.9 ± 0.1 km/s. Pre-detonator wave speeds were calibrated to minimize the transient behavior of the detonation transition within the LMDE; detonation wave speed within the LMDE was steady between injectors #5–15.

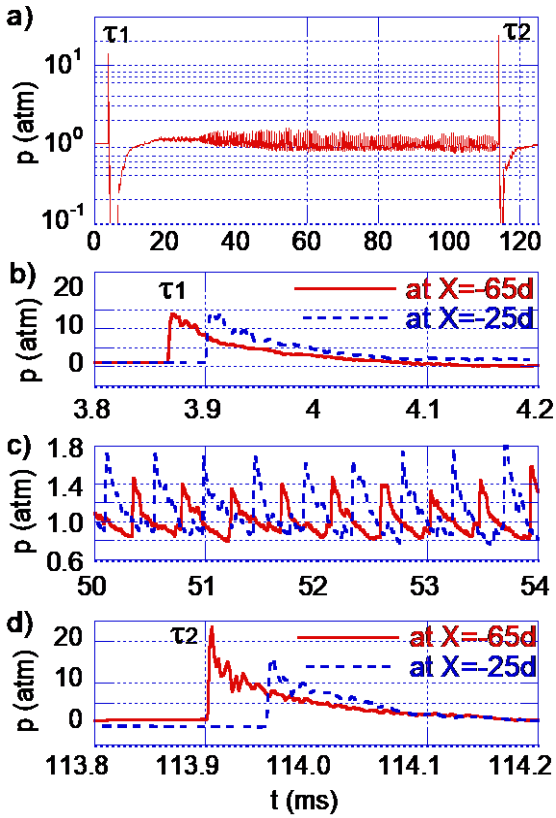

Figure 4.2: Typical dynamic pressure recording of LMDE test (a). Sensor response to initial detonation transmission (b), combustion instability (c), and second detonation transmission (d). Relative times for detonation transits in subsequent images noted on corresponding plots.

During the LMDE test in Fig. 4.2 there were two distinct detonation confinement configurations. The first detonation transit occurred in a reactant cross-flow of ethylene-oxygen confined by a "cold" background gas, Fig. 4.2(b). Channel pressure and temperature were 1 atm and 294 K, respectively. Following the first transit a combustion instability within the LMDE periodically deflagrated the reactant injection and filled the channel with combustion products, Fig. 4.2(c). The second detonation transit occurred in a reactant cross-flow of ethylene-oxygen confined by "hot" combustion products, Fig. 4.2(d). Channel pressure was 1 atm prior to detonation transit. During all test phases the

reactants were rigidly confined by the injection surface, the wall closest to the pre-detonator, and within the LMDE channel by the quartz windows. Reactants were free to expand upwards and in the direction of detonation propagation.

4.4 Results and Discussion

In RDE the pressure rise associated with the periodic passage of a detonation momentarily halts reactant inflow. Expansion of the flow to the initial pressure occurs following this spike, at which point the reactant refresh into the annulus renews. The exact details of how this refresh occurs are configuration dependent; the scope instead was limited to examining what general features resulted from such transient reactant inflow.

For the first detonation transit in the LMDE test, pressure in reactant manifolds was increased prior to detonation ignition to simulate transient reactant refresh of the RDE. Ethylene and oxygen reactants were introduced independently into the base of the recessed cylindrical injectors to ensure reactants are at an equal height within the channel at the time of detonation transit. Prior to this injection the LMDE was purged with an oxygen back- ground gas to reduce the number of species present within the channel.

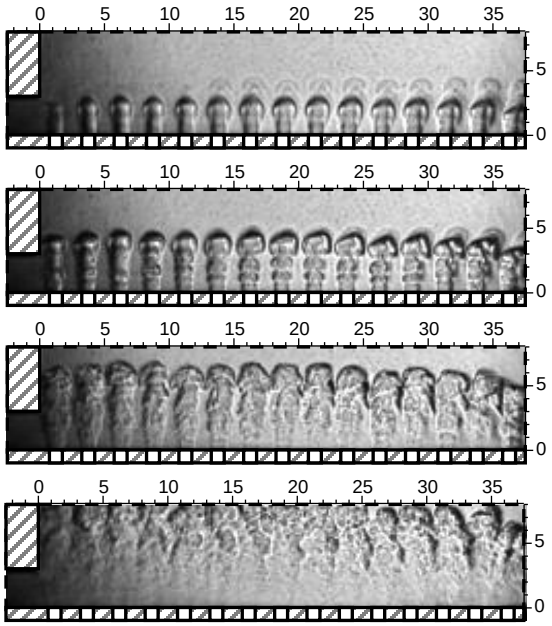

Figure 4.3: Evolving reactant cross-flow with increasing manifold back-pressure. From top to bottom, images a-d show times τ_1 – 1.7ms, τ_1 – 1.1ms, τ_1 – 0.5ms, and τ_1 + 0.1ms, respectively.

Figure 4.3 shows the evolution of the reactant cross-flow in time. Due to its lower propagation velocity, oxygen was injected prior to ethylene. At the time presented in Fig. 4.3(a) the oxygen reactants were at a height of 4**d**, while the ethylene reactants were at a height of 2.5**d**. All fifteen cross-flow jets were observed as laminar with large gaps of background gas between them.

In Fig. 4.3(b) the oxygen and ethylene reactants were both approximately at a height of 5**d** and evidence of gaps between reactant jets remained. As manifold backpressure increased, the cross-flow became more turbulent as seen in Fig. 4.3(c); adjacent reactant jets began impinging and mixing with the background gas in the rectangular channel. Despite improved mixing from the increased turbulence, the dark regions in the cross-flow front at a height of 6–7**d** indicate significant variations in local density, and therefore either poorly mixed reactants or strong concentrations of a single species at the jet tip. Mixing of cross-flow jets increased further in Fig. 4.3(d), but evidence of poor mixing remained.

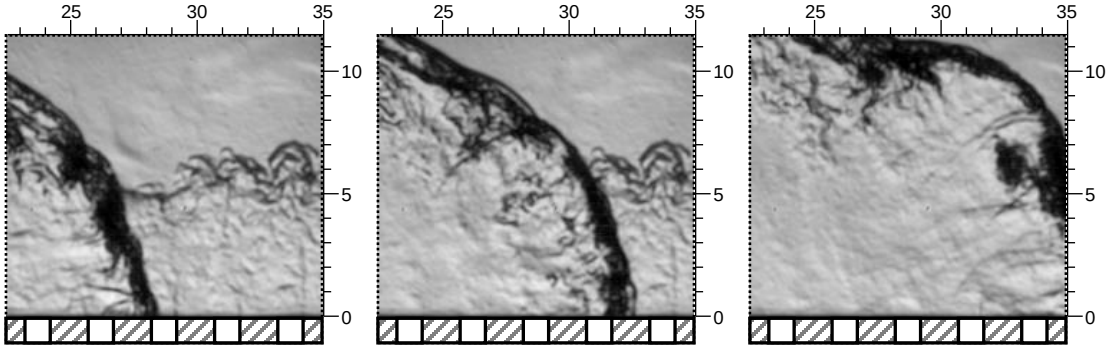

Figure 4.4: Detailed sequence of detonation in ethylene-oxygen cross-flow. From left to right, images a-c show times $\tau_1 + 86\mu s$, $\tau_1 + 91\mu s$, and $\tau_1 + 96\mu s$, respectively.

Transmission of the first detonation wave through the cross-flow is captured with high- resolution schlieren images in Fig. 4.4. The interface between the pre-detonator and LMDE channel is characterized by a sharp expansion at X = 0, as seen in Fig. 4.3.

After initial transient behavior due to diffraction at X = 0, the transmitted detonation propagated steadily from jets #5–15 at a speed of 2.4 ± 0.2 km/s into a reactant layer with a global equivalence ratio of 1. Although this measured wave speed was approximately 95% of the one- dimensional and well-mixed CJ speed, the schlieren images indicate the wave was likely propagating locally at both fuel rich and lean conditions.

Variations in the thickness of the detonation front were present in the schlieren images. Local discrepancies in reactant concentration and mixedness within the cross-flow yield different induction times behind the detonation front, and likely contributed to this effect. The primary contribution to this thickness was from the highly three-dimensional injection geometry; the circular jets emerged into a rectangular channel, producing a non-planar geometry across the span of the channel. Since schlieren imaging integrates across the entire channel width, this technique would blur three-dimensional structures.

Dark spots that appear to be unreacted components of the cross-flow were seen in Fig. 4.4(b) and (c), particularly around X = 30–33**d** . One such spot at X = 33**d** and Y = 6**d** in Fig. 4.4 (c) was the result of poor mixing at the tip of the cross-flow, while the spot at X = 30**d** and Y = 3.5**d** in Fig. 4.4(b) instead originated from variations in mixture or species concentration within the middle of the cross-flow.

Figure 4.4 also contains a number of transverse waves connected to the detonation front, in particular around X = 26–29**d** and Y = 7–10**d** in Fig. 4.4(b). These features are examined at a higher framerate in Fig. 4.5(c)–(e), where the origin of the trans- verse waves were revealed to be an unreacted pocket of gas behind the front, located near the

tip of the reactant cross-flow. Generation of transverse waves by means of pockets of unreacted gas at the jet tip has been demonstrated numerically in cases of uniform gas composition [4.21]. Figure 4.5(a) captures a “micro explosion” radiating shock waves in the immediate wake of the detonation front, also generated from a pocket of unreacted gas, and indicates that transverse waves can be generated elsewhere along the detonation front where non- uniformities in the reactant cross-flow composition exist.

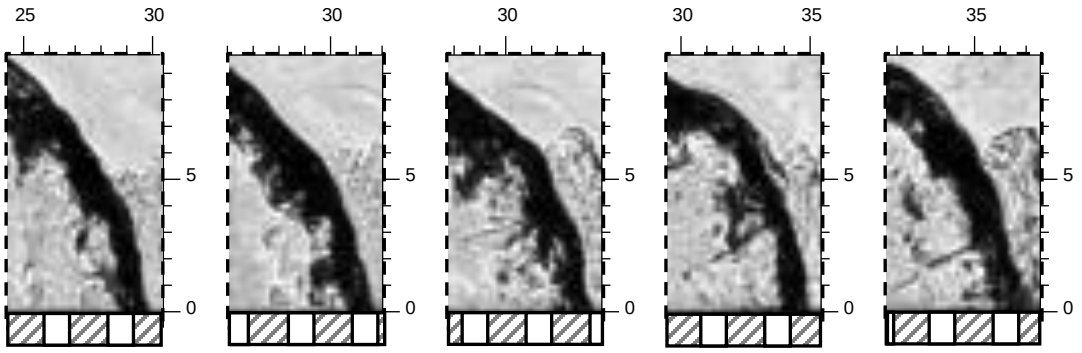

Figure 4.5: Appearance of “micro explosion” and growth of transverse wave. From left to right, images a-e show times $\tau_1 + 87\mu s$, $\tau_1 + 89\mu s$, $\tau_1 + 91\mu s$, $\tau_1 + 93\mu s$, and $\tau_1 + 95\mu s$, respectively.

The connection between these structures may be expected, as acoustic disturbances downstream of the detonation wave are able to influence the detonation front. In the case of these unreacted pockets, they are subjected to the strong pressure and temperature rise associated with the detonation wave, but their difference in composition correlates with different induction time scales. Combustion of these pockets occurs behind the detonation front, and the resulting pressure waves influence the detonation by providing an additional source of transverse waves to stabilize detonation propagation.

To resolve additional features along the detonation front, a second Phantom v2512 camera was used to simultaneously record schlieren and shadowgraph images

of the detonation in reactant cross-flow. Together the two imaging techniques were used to generate an annotated image of the typical structure of a detonation in a cross-flow of ethylene-oxygen, Fig. 4.6.

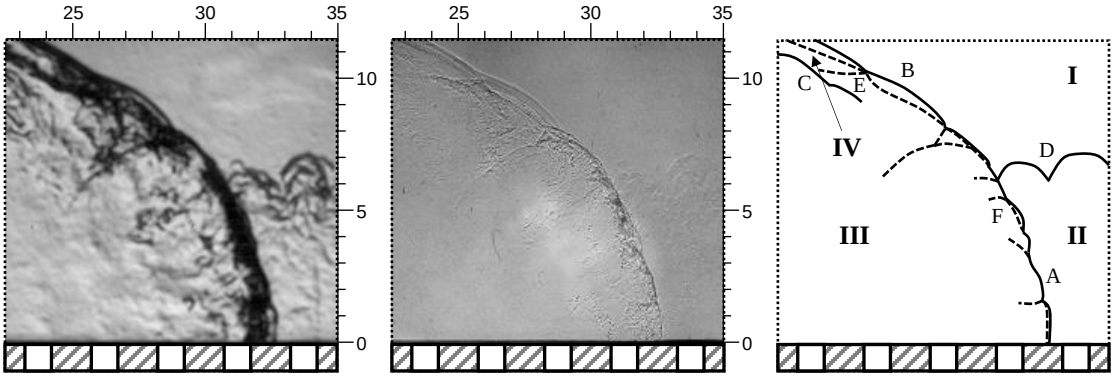

Figure 4.6: Schlieren (left), shadowgraph (middle), and annotated illustration (right) of detonation in cross-flow of ethylene-oxygen mixture.

Four regions of flow are marked in Fig. 4.6: background/purge gas (I), reactant cross-flow (II), combusted products (III), and shocked background/purge gas (IV). Marked structures in the figure include: detonation front (A), curved oblique shock(s) (B), material interface between shocked gas and combustion products (C), material interface between reactant cross-flow and back- ground/purge gas (D), shocklets in region IV (E), and transverse waves (F).

The detonation front gently curved back to transition into an oblique shock structure. This gradual incline indicated that either the improved mixing near the base of the cross-flow due to turbulent injection, or the local reactant concentration, was more favorable for detonation propagation. The expected loss of transverse waves through such a weak gaseous confinement of the reactant cross- flow stood in stark opposition to the continued survival of the detonation front. It has already been suggested that pockets of unreacted cross-flow may have contributed supplemental transverse waves, but it may be possible that a sufficient number of transverse waves

were already present to tolerate the loss rate to this interface, or that an entirely separate means of generating the transverse waves existed during the test.

The varying strength of transverse waves in Fig. 4.6 likely reflects local reactant reactivity, or three-dimensionality of the detonation front. Although the transverse waves meet and form triple points along the detonation front, the resulting cells would be irregular and their size dependent on the cross-flow mixing and species distribution characteristics. The schlieren image of the detonation front at X = 32.5**d** and Y = 0 suggests a complex wave-wall interactions. One possible explanation is that the reaction zone separates from the shock wave without a strong concentration of reactants present between jets, and the other is that the complex three-dimensional injection geometry is producing likewise three-dimensional shock features.

In RDE the average period between detonation transits is governed by the annulus circumference, wave speed, and number of stabilized detonation waves; cycling of the pre-detonator for the second detonation in the LMDE test required a minimum of 110 ms between waves. During this time reactant manifolds pressurized to a steady state of 2 atm and the reactant cross-flow continued to enter the channel with a

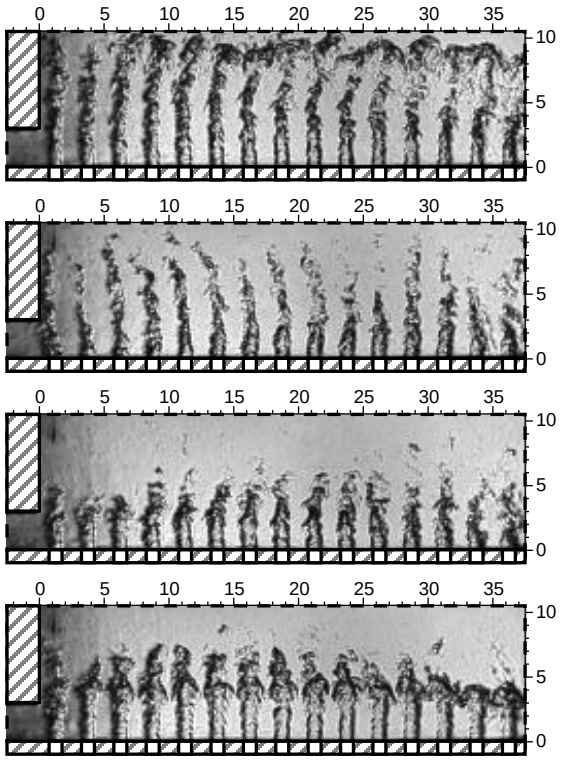

Figure 4.7: Combustion of cross-flow between detonation transits via instability. From top to bottom, images a-d show phases ψ = 0°, ψ = 90°, ψ = 180°, and ψ = 270°, respectively.

global equivalence ratio of 2.9. Following the first detonation transit a combustion instability repeatedly burned off the reactant cross-flow as it developed to a height of ~10**d** , shown as four phases in Fig. 4.7 . Phases of instability are noted with ψ, where ψ = 0° references the point in the instability just prior to combustion.

Analysis of the signal recorded by dynamic pressure transducers at the pre-detonator exit indicated the typical frequency of the combustion instability was 1.9 ± 0.1 kHz, Fig. 4.2(c). The period of the combustion instability is on the same order of magnitude as RDE reactant refresh. The key difference between the two configurations is that the combustion products produced by the instability are the result of deflagration, whereas in RDE they are produced by detonation.

Ignition of the pre-detonator was timed such that the detonation wave arrived in the LMDE as the cross-flow approached the state shown in Fig. 4.7(a), just prior to combustion via instability. Cross-flow composition between reactant jets in Fig. 4.7(a) was fairly uniform, while the jet cores appeared as dark structures; temperature differences between the reactant jet core and reactants mixed with combustion

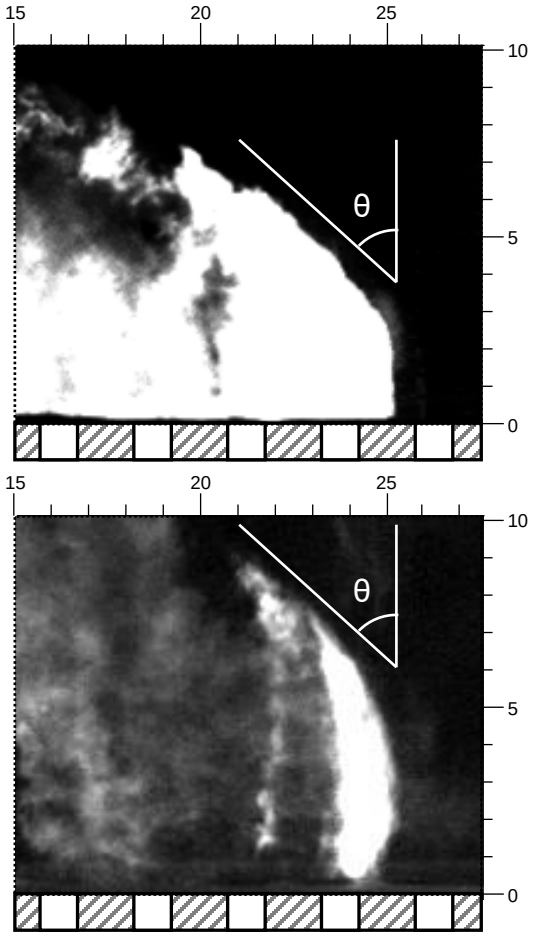

Figure 4.8: Comparison of natural luminescence from the first (top, a) and second (bottom, b) detonation waves.

products provide a stark contrast in the schlieren images.

The temperature of the background gas, i.e., the combustion products, reduced the strength of schlieren images in the narrow test section; luminescence of the second detonation transit is shown in Fig. 4.8 with the luminescence of the first detonation transit included for reference. Both test cases produced similar oblique shock angles (θ), validating the use of the first detonation transit for detailed structure visualization. The transmitted detonation wave speed was limited to 1.3 ± 0.2 km/s due to a combination of the reduced pre-detonator incident wave speed, the poor mixing between adjacent re- actant jets, and the large cell size expected at fuel rich conditions.

The detonation front for the second wave was lofted and met the channel base at a non- perpendicular angle as a result of gaps between the discrete reactant jets near the channel base. In the first detonation transit the reactant cross-flow developed over the period of 3–4 ms as the reactant manifolds pressurized, providing ample time for reactants to mix and diffuse into the bottom of the channel; during the combustion instability a comparable height cross-flow developed in 0.52 ± 0.02ms.

Despite the reduction in mixing between adjacent jets, mixing within jets was quite good for the second detonation transit. Figure 4.8 shows combustion was more concentrated behind the detonation front during the second transit than the first. The column of luminescence in Fig. 4.8(b) at X = 21.5**d** indicated the cores of the reactant jets provided the bulk of the energy release during the second transit, which agreed with the schlieren visualization of the reactants from Fig. 4.7(a).

Visualization of the reactant refresh in the wake of the second detonation transit provides insight into reactant cross-flow recovery from the impulsive jump in pressure.

Figure 4.9 shows a composite image, split over two rows, of the reactant cross- flow refresh in the wave-fixed reference frame. Note that the direction of wave propagation is flipped to allow for the time axis to increase from left to right. For the case shown, the detonation wave propagated at a rate of one reactant injector every 5 μs with images acquired at 200 kHz. Placing every fifth image side-by-side performs the transformation from laboratory-fixed to wave-fixed reference frame for the five injectors.

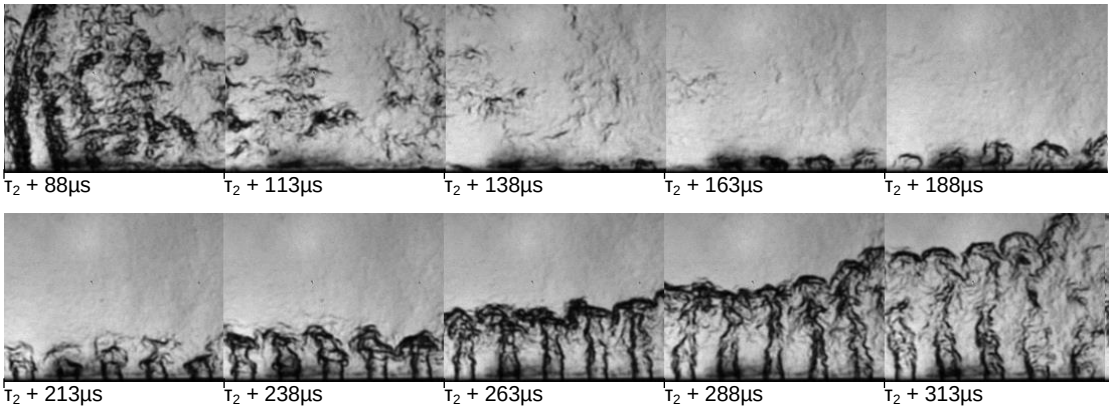

Figure 4.9: Composite image of reactant cross-flow refresh in wave-fixed reference frame. Times relative to τ_2 are shown increasing from left to right. Apparent wave motion from right to left.

Reactant cross-flow injection was halted immediately in the wake of the detonation wave. Injection did not recover until 50–75 μs after the wave transit. This time corresponded with when the mixing and/or combustion of the pockets of unreacted gases behind the detonation front produced a uniform background gas composition. Immediately following the rise in pressure associated with the detonation transit some backflow of combustion products into the recessed tubes and the transmission of some shock structures was likely to have occurred; initial injection of the reactant cross-flow

was at a low speed with a poorly defined material interface between fresh reactants and combustion products.

Shortly following the return of reactant injection the material interface accelerated upwards, indicating that the pressure in the wake of the detonation wave dropped. During this period of accelerated reactant cross-flow growth the delineation of the material interface between the cross-flow and combustion products increased. Mixing between and within the reactant jets increased as well, as a result the reactant cross-flow was partially made up of combustion products. Thorough mixing with these products will dilute the reactant concentration and increase cross-flow temperature. In some configurations the conditions may cause autoignition of the reactant cross-flow to occur via this mixing. Approximately 250 μs after detonation transit the reactant cross-flow recovered to its pre- detonation height.

4.5 Summary and Conclusions

We investigated the detailed flowfield structures associated with detonation waves propagating inside a straight channel that simulates an un- wrapped RDE combustor. Partially premixed jets of ethylene-oxygen mixture were established, and two detonation waves from a pre-detonator were scheduled to arrive at the reactant jets as the jets reached the predetermined fill-height inside the combustor channel. Under the controlled test conditions investigated, the detonation waves continued to propagate along the channel by detonating the reactant cross-flow.

The first detonation wave was sent to the combustor with a cold background gas confining the reactive cross-flow. After the first detonation wave passage, the reactants ignited and established a combustion instability that periodically burned off the cross-

flow. About 110 ms later, the second detonation wave was sent into the reactive cross-flow bound by the hot combustion products of the instability. After the second wave passage, the temporal evolution of the ensuing flowfield simulated the injection refresh process occurring in RDE.

The detonation waves in this study were characterized by unsteady, highly irregular, and multi-dimensional structures that were observed on the lead wave front. Some of these structures were seen protruding ahead of the more two- dimensional incident shock wave that surged ahead forming a lead shock wave front. The present experimental data reveals details of the flow structure under two different controlled bounding gas conditions. While these observations are consistent with what is expected of high activation energy reactants, other factors can also contribute to the un-steadiness, such as the three-dimensional nature of the flowfield and non-uniform mixing of the reactants due to extremely short injection time and low fill-height.

The experimental data showed that transverse waves were generated at the tip of the reactive cross-flow, as observed in the numerical study by Uemura et al. (2013), who further linked the transverse wave generation and reflection processes to the detonation propagation mechanism. The present finding not only provides experimental evidence of transverse wave generation process at the tip of the cross-flow, but also appears to support Uemura's description of the physical mechanisms. In addition, the present findings include evidence of transverse wave generation through the combustion of unreacted pockets of gas in the wake of the detonation wave.

Lastly, experimental data was provided that captures the reactant jet refresh process following a detonation wave passage. The results showed that the typical

characteristic time for reactant blockage was on the order of 100 μs for the case tested. While the flow blockage time should be a function of the injector geometry and the stagnation pressure available, it could limit the maximum operating frequency in the steady state operation of a practical system. The present approach can be used as an effective tool for studying physical mechanisms associated with RDE relevant processes. Furthermore, the experimental results and findings appear well suited for understanding the RDE-relevant flow- field structure and provide a database for validation purpose.

4.6 Acknowledgments

This material is based upon work supported by the U.S. Air Force Office of Scientific Research under grant number FA9550-17-1-0086 with Dr. Chiping Li as the program manager.

4.7 References

[4.1] M. Hishida, T. Fujiwara, and P. Wolanski. Fundamentals of rotating detonations. *Shock Waves*, 19(1):1-10, 2009.

[4.2] D. Schwer and K. Kailasanath. Numerical investigation of the physics of rotating-detonation-engines. *Proceedings of the Combustion Institute*, 33(2):2195-2202, 2011.

[4.3] R. T. Fievisohn and K. H. Yu. Steady-State Analysis of Rotating Detonation Engine Flowfields with the Method of Characteristics. *Journal of Propulsion and Power*, 33(1):89-99, 2017.

[4.4] F. K. Lu, R. Miller, M. R. Nalim, and K. H. Yu. Introduction: Special Section on Pressure Gain Combustion. *Journal of Propulsion and Power*, 33(1):16, 2017.

[4.5] R. M. Clayton and R. S. Rogero. Experimental Measurements on a Rotating Detonation-Like Wave Observed During Liquid Rocket Resonant Combustion. Jet Propulsion Laboratory Technical Report No. 32-788, 1965.

[4.6] J. A. Nicholls, R. E. Cullen, and K. W. Ragland. Feasibility studies of a rotating detonation wave rocket motor. *Journal of Spacecraft and Rockets*, 3(6):893-898, 1966.

[4.7] T. C. Adamson Jr. and G. R. Olsson. Performance Analysis of a Rotating Detonation Wave Rocket Engine. *Astronautica Acta*, 13(4):405-415, 1967.

[4.8] P. I. Shen and T. C. Adamson Jr. Theoretical Analysis of a Rotating Two-Phase Detonation in Liquid Rocket Motors. *Astronautica Acta*, 17(4):715-728, 1972.

[4.9] J. Kindracki, P. Wolanski, and Z. Gut. Experimental research on the rotating detonation in gaseous fuels-oxygen mixtures. *Shock Waves*, 21(2):75:84, 2011.

[4.10] F. A. Bykovskii and E.F. Vedernikov. Continuous detonation combustion of an annular gas-mixture layer. *Combustion, Explosion and Shock Waves*, 32:489:491, 1996.

[4.11] K. Kailasanath. Review of Propulsion Applications of Detonation Waves. *AIAA Journal*, 38(9):1698-1708, 2000.

[4.12] P. Wolanski. Detonative propulsion. *Proceedings of the Combustion Institute*, 34(1):125-158, 2013.

[4.13] F. K. Lu and E. M. Braun. Rotating Detonation Wave Propulsion: Experimental Challenged, Modeling, and Engine Concepts. *Journal of Propulsion and Power*, 30(5):1125-1142, 2014.

[4.14] Y. T. Shao, M. Liu, and J. P. Wang. Numerical Investigation of Rotating Detonation Engine Propulsive Performance. *Combustion Science and Technology*, 182(11-12):1586-1597, 2010.

[4.15] F. A. Bykovskii, S. A. Zhdan, and E. F. Vedernikov. Continuous Spin Detonations. *Journal of Propulsion and Power*, 22(6):1204-1216, 2006.

[4.16] J. R. Burr and K. H. Yu. Detonation Propagation in a Linear Channel with Discrete Injectors and Side Relief. In *26th International Colloquium on the Dynamics of Explosions and Reactive Systems*, ICDERS Paper 2017-1107, Aug. 2017.

[4.17] R. T. Fievisohn and K. H. Yu. Parametric Study of an Ethylene-Air Rotating Detonation Engine Using an Ideal Model. In *54th AIAA Aerospace Sciences Meeting*, AIAA Paper 2016-1403, Jan. 2016.

[4.18] N. Tsuboi, Y. Watanabe, T. Kojima, and A. Koichi Hayashi. Numerical estimation of the thrust performance on a rotating detonation engine for a hydrogen-oxygen mixture. *Proceedings of the Combustion Institute*, 35(2):2005-2013, 2015.

[4.19] R. Zhou and J. P. Wang. Numerical investigation of flow particle paths and thermodynamic performance of continuously rotating detonation engines. *Combustion and Flame*, 159(12):3632-3645, 2012.

[4.20] J. C. Shank. Development and Testing of a Rotating Detonation Engine Run on Hydrogen and Air. MS thesis, Air Force Institute of Technology, 2012.

[4.21] Y. Uemura, A. Koichi Hayashi, M. Asahara, N. Tsuboi, and E. Yamada. Transverse wave generation mechanisms in rotating detonation. *Proceedings of the Combustion Institute*, 34(2):1981-1989, 2013.

Chapter 5: Propagation Modes of CH_4 Detonations

The contents of this chapter examine the features of CH_4-O_2 detonations in the eLMDE experimental facility (Appendix C).

5.1 Abstract

An experimental study was conducted to characterize detonation waves propagating across a row of temporally evolving reactant jets of partially mixed gaseous methane-oxygen within a linear channel. The geometric and flow configuration simulated the flowfield within the unwrapped annulus of a rotating detonation engine (RDE). In this setup, methane and oxygen were injected independently into 48 discrete injector tubes, forming a partially mixed reactant layer. Detonation waves were initiated via a pre-detonator positioned at the entrance of the channel combustor at appropriate timings to yield varied reactant layer heights. Characterization of the resulting detonation-reactant interaction was performed with simultaneous measurements of shadowgraph, chemiluminescence, luminescence, and dynamic pressure measurements. Repeated experiments at several controlled conditions were conducted and yielded several distinct propagation modes. Robust detonations propagating near the one-dimensional Chapman-Jouguet (CJ) speed were observed for fill heights above 18 injector diameters. At lower heights a bifurcating behavior was observed that alternated between a weak detonation propagating at 85% of the one-dimensional CJ speed and a decoupling detonation wave. For reactant fill heights of 14 jet diameters a decoupled shock-flame was consistently observed.

Shadowgraph images of these cases reveal the presence of triple points along the wave front, with the results between cases indicating that several triple points may be required to maintain the robustness of close shock-reaction coupling and stable wave propagation in the RDE configuration.

5.2 Introduction

Rotating detonation engine (RDE) has recently garnered interest as an alternative combustor concept [5.1-5.3]. The detonation-based thermodynamic cycle of RDE provides possible work and efficiency improvements over Brayton-cycle engines for certain applications [5.4-5.7]. Additional system benefits associated with the simple design, compact reaction zone, and cyclical heat addition process further extend the potential of RDE; the renewed interest in RDE has grown in parallel with the demand for improved fuel efficiency and improvements in related technologies such as additive manufacturing and high-temperature materials. Proposed applications of RDE extend to both air-breathing [5.1-5.2,5.8] and rocket [5.9-5.14] systems.

RDE combustor geometry is characterized by an annular channel with reactants injected in the axial direction and one or more detonations propagating in the azimuthal direction [5.15]. In single wave operation, reactant refresh occurs while the detonation propagates around the circumference of the annular channel. Reactant wave confinement occurs to the sides by the annulus wall, above by the hot products from the previous detonation cycle, and below by the reactant injection plane; deflagration between the fresh reactants and detonation products is common. The pressure rise associated with the detonation abruptly halts reactant inflow, and often results in backflow of combustion products into the feed plenum. Reactant injection resumes

when the local annulus pressure drops below the reactant stagnation pressure. In implementation of RDE, local variations in reactant mixedness, species concentrations, and fill heights can have drastic impacts on the propagation of the detonation(s) [5.16-5.22]. While there have been numerous fundamental and applied research activities involving RDE [5.23-5.36], there is still a lack of high-quality experimental data for visualizing the flowfield.

This study is motivated by the desire to study the fundamental flow structure associated with a detonation wave propagating transversely to discretely spaced reactant jets of methane-oxygen composition in a linear model of the RDE combustor. Through the use of a canonical configuration that captures the essence of the RDE flowfield, it was hoped that the detonation wave structure interacting with reactant flows under controlled conditions could be better visualized. Because reactants are injected from the base of the channel just prior to detonation wave arrival, there is likely insufficient time to allow for homogenous mixing inside of the channel. The result is a periodically varying mixture composition in the direction of wave propagation.

The purpose of this work was to obtain detailed information on the fundamental structure associated with a detonation wave propagating inside a channel containing transversely flowing reactants. A combination of shadowgraph, chemiluminescence, luminescence, and dynamic pressure transducer measurements are used to examine the time dependent behavior of the detonation-reactant interaction. Only the essence of the RDE geometry is simulated in this experiment and excludes the effect of annulus curvature. We hope the simplified combustor configuration allows us to obtain better

understanding of the physics of the RDE flowfields by focusing our attention on the detonation-flowfield interaction inside a narrow channel.

5.3 Experimental Setup

2.4.1 Linear Detonation Facility

Detonation experiments were performed using the extended linear model detonation engine (eLMDE) combustor at the University of Maryland's Propulsion Research Laboratory. Design of the eLMDE combustor incorporated elements of the AFRL's 6-inch RDE [5.37] and the NRL's premixed microinjection geometries [5.2]; a schematic of the flowfield detailing the detonation channel and recessed tubes for reactant injection is shown in Fig. 5.1 with dimensions normalized by recessed tube diameter **d**, 2.54 mm. The 48 discrete recessed reactant tubes are not visualized in the configuration shown.

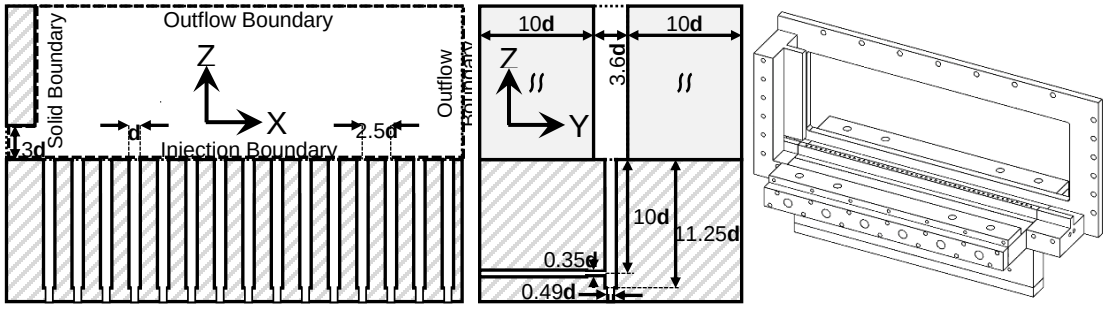

Figure 5.1: Partial cross-section of eLMDE and injectors in the X-Z (left) and Y-Z (middle) planes. Isometric view of facility with full injector array (right). Optically accessible region indicated by dashed boundary.

RDE inflow is simulated in the eLMDE by reactant flow propagating in the positive Z direction in Fig. 5.1; unmixed methane and oxygen streams impinge 10**d** below the injection boundary of the eLMDE channel, allowing for partial but incomplete mixing of the reactant species. Independent solenoid control of methane

and oxygen gases allows for variation in both reactant layer height and phasing between reactant injection. Fuel injection phasing (θ_{FUEL}) is relative to the oxidizer injection and is normalized by the total injection period; positive θ_{FUEL} indicates oxidizer injection occurs prior to fuel injection. Steady-state reactant mass flow rate is controlled by varying jet stagnation pressure prior to opening solenoids. A summary of test conditions, as well as the range of typically observed wave speeds through the reactant layer, are shown in Table 5.1; mass flow rates are per injector, and reactant layer height is normalized by injector tube diameter.

Table 5.1: Methane-oxygen reactant test conditions.

Case	ϕ_{JET}	$\dot{m}_{JET}$ (g/s)	θ_{FUEL} (deg.)	h_{JET} (**d**)	$V_{TRANSIT}$ (m/s)
1	0.8	0.38	0	22 ± 3	2260 ± 30
2a	1.2	0.48	110	16 ± 2	2070 ± 50
2b	1.2	0.38	110	16 ± 2	1425 ± 300
3	1.0	0.48	-70	14	710 ± 10

Detonations propagate in the positive X direction in Fig. 5.1. A pre-detonator with internal diameter of 4.3**d** and L/D of 42 generates a steady, stoichiometric ethylene-oxygen detonation. A transition piece converts the circular cross-section to a rectangular one with sides measuring 3**d** and 3.6**d** just prior to entering the eLMDE at the solid boundary marked in Fig. 5.1. Pre-detonator fill times are varied to control the strength of the detonation wave upon entering the eLMDE facility; an electric spark from an automotive ignition system using an iridium tipped spark plug initiates combustion. Reactant layer height in the eLMDE (h_{JET}) is recorded at the time of detonation transit through the gas layer.

2.4.2 Flow Diagnostics

Simultaneously acquired shadowgraph and CH* chemiluminescence served as the primary means of studying and characterizing the behavior of the different detonation cases examined. A conventional Z-shadowgraph configuration was employed to obtain the second spatial derivative of density in the XZ plane of the eLMDE facility. A high-speed Phantom v2512 camera was used with a CAVILUX Smart pulsing diode laser (640 nm) and two spherical mirrors for this setup. The images were recorded at a rate of 30 kHz with a laser pulse width of 10-30 ns. Vision Research's Phantom Camera Control (PCC) software was used to control the cameras as well as to record, access, and save the images.

The chemiluminescence deexcitation of the CH* radical was photographed in conjunction with the shadowgraph images. The CH* signal captured was used in this study as an optical marker of heat release; CH* is primarily produced through the reaction of monatomic and diatomic oxygen with the ethynyl radical [5.38]. A second Phantom v2512 camera operating simultaneously with the shadowgraph camera and with a 430±5 nm optical bandpass filter (Edmund Optics #65-198) also collected images at 30 kHz. The exposure time for the chemiluminescence was 480 ns; shadowgraph and chemiluminescence images are synchronized such that the end of the CAVILUX laser pulse coincides with the end of the chemiluminescence Phantom exposure.

High frequency pressure sensors (PCB 113B24) with a range of 0-68 atm were recorded at 500 kHz using a National Instruments cDAQ-9188 system. Dynamic pressure measurements were collected in a vertical array positioned at X = 69.1**d**, from

Y = 2.3**d** to Y = 24.7**d** in increments of 7.5**d**, to characterize the detonation pressure profile at various points within the reactant layer. Two additional dynamic pressure transducers were positioned 65**d** and 25**d** upstream of the exit of the pre-detonator to measure the incident detonation strength.

5.4 Results

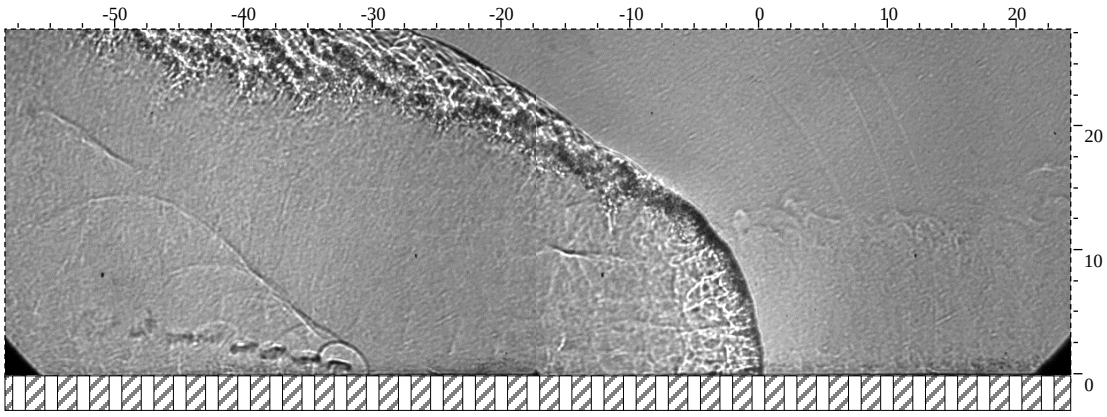

Figure 5.2: Composite image of detonation propagation into gaseous methane-oxygen mixture (2310 m/s). Horizontal coordinates are relative to detonation front.

The shadowgraph of a typical robust methane-oxygen detonation wave propagating through the eLMDE facility is presented in Fig. 5.2. In this figure the wave propagates from left to right, with the horizontal coordinates relative to the detonation front; two subsequent frames acquired at 83.3 kHz are used to generate the composite image shown. The detonation front gradually inclines as it nears the top of the reactant layer and gives way to the oblique shock propagating into the gas confining the reactant layer. As the inclination of the detonation increases the apparent thickness of the detonation front increases; the broadening of the dark region immediately post-detonation front is indicative that the width of the reaction zone, where rapid density

change is occurring, is increasing as well. The position and distribution of the heat release within this broadening region is unclear from the shadowgraph alone.

Trailing the detonation by 30**d** is a reflected shock structure from the recessed injectors. In the configuration detailed in Fig. 5.1, the recessed injector area is approximately 9% of the total channel area, allowing for significant transmission of the incident detonation wave into the recessed tube. The reflection of the transmitted shock from the base of the recessed tube yields the trailing features observed in Fig. 5.2. In RDE, injection of fresh reactants following a detonation transit cannot begin until both this process and the decrease of annulus pressure below the feed system stagnation pressure have completed.

Natural luminescence from the detonation was acquired simultaneously with shadowgraph in Fig. 5.3. In this and subsequent figures the marked horizontal position is relative to the exit plane of the pre-detonator at the far left of the eLMDE channel in Fig. 5.1. The majority of Fig. 5.3 is representative of a shadowgraph exposure of the detonation transit, but at locations of strong natural luminescence the image is saturated.

Strong transverse shocks are visualized to either side of the saturation region; from the

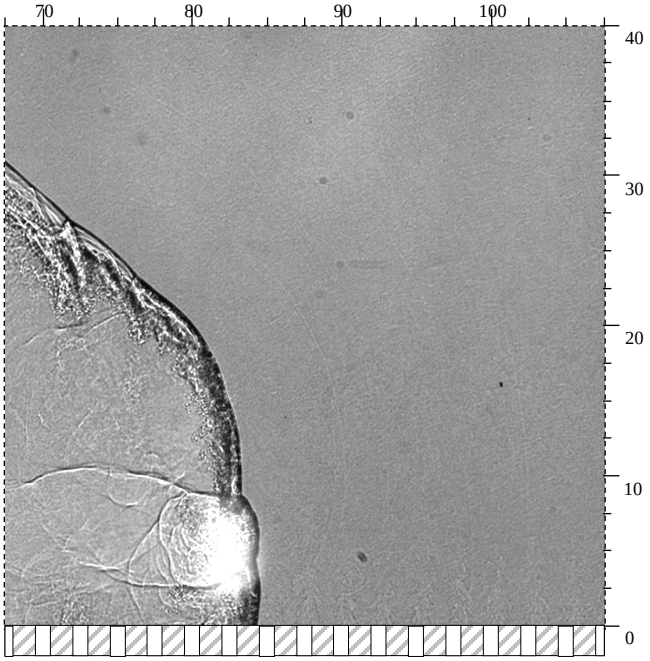

Figure 5.3: Simultaneous exposure of shadowgraph and luminescence.

structures present it is inferred the luminescence is occurring in the wake of a Mach stem with the transverse shocks propagating away from the region of luminescence. Above the upper transverse shock, the reaction zone is separated from the incident shock front and the corresponding luminescence is negligible. The intersection of the incident shock front, the Mach stem ahead of the luminescence region, and the upper transverse shock is directly visualized as a detonation triple point. The expected position of the triple point corresponding to the lower transverse shock coincides with significant luminescence and is not directly observed.

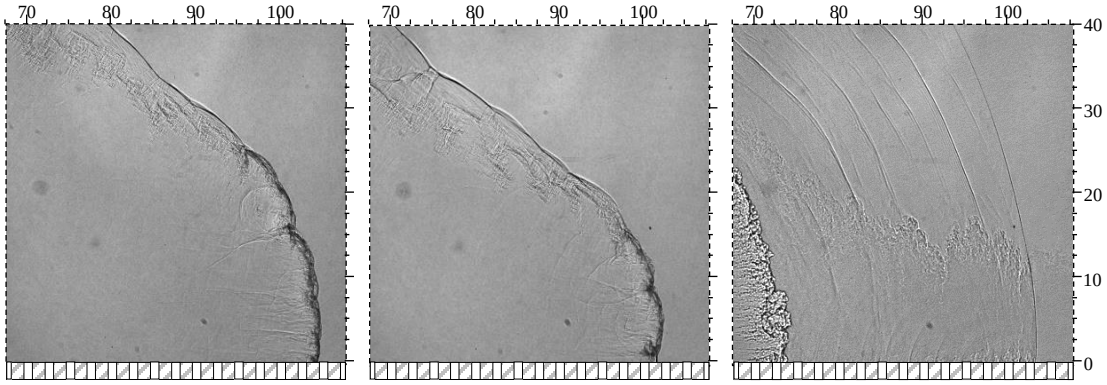

(a) Case 1, τ_1 (b) Case 2a, τ_2 (c) Case 3, τ_3

Figure 5.4: Shadowgraph images of (a) strong detonation propagation, (b) weak detonation propagation, and (c) decoupled shock-flame propagation.

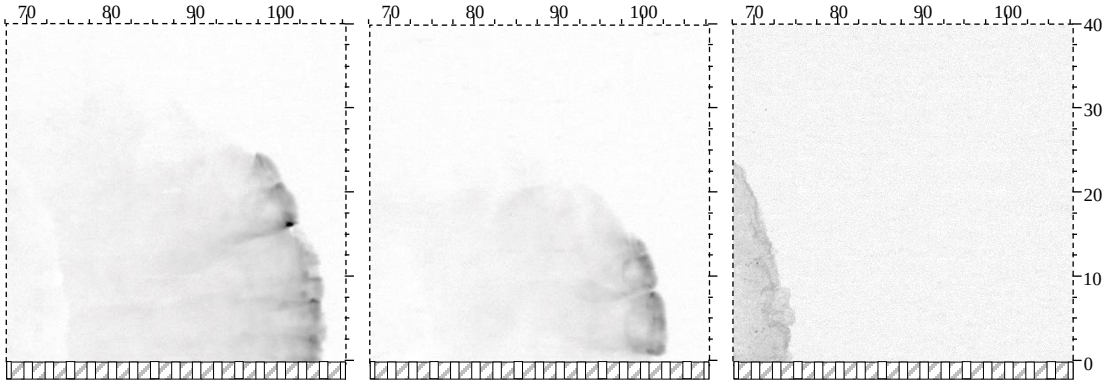

(a) Case 1, τ_1 (b) Case 2a, τ_2 (c) Case 3, τ_3

Figure 5.5: Chemiluminescence images of (a) strong detonation propagation, and (b) weak detonation propagation, and luminescence of (c) decoupled shock-flame.

Separation of shadowgraph and CH* chemiluminescence imaging to two simultaneously operating cameras yielded the images in Fig. 5.4 and Fig. 5.5, respectively; images are characteristic of their corresponding test case. Natural luminescence is absent from the shadowgraphy due to the addition of a bandpass filter at 640 nm. For test Case 3, natural luminescence is used in place of CH* chemiluminescence due to the low signal strength observed for the decoupled shock-flame in comparison to other cases. Chemiluminescence and luminescence exposures in Fig. 5.5 are inverted such that dark regions correspond to emissions.

A strong detonation propagation is shown in Fig. 5.4a and Fig. 5.5a. In this case the detonation propagates at 2260 m/s, or at 95% of the one-dimensional and well-mixed CJ wave speed for a stoichiometric methane-oxygen detonation. Figure 5.4a shows a number of transverse wave features along the entirety of the incident front; the strongest transverse shocks are present in both the shadowgraph and chemiluminescence images. The detonation front, which meets the channel base orthogonally, gradually inclines and transitions into the oblique shock. Despite this inclination, the reaction zone appears closely coupled to the detonation in the shadowgraph. Chemiluminescence of Case 1 shows that the presence of CH* is coincident with the wave front throughout the entirety of the reactant layer, with weak emissions extending well behind the incident front.

A strong localized region of heat release is noted at the approximate position of X = 100**d** and Y = 17**d** in Fig. 5.5a. By examination of the corresponding point in Fig. 5.4a, it is clear that this position corresponds to a triple point intersection between a transverse shock, normal shock, and Mach stem. In proximity to this point in the

shadowgraph is a circular shock feature, likely the result of a small micro-explosion along the detonation front and the source of the strong transverse shock previously noted. These transverse features are numerous in Case 1, and in particular are most closely clustered in the lower part of the detonation front where the wave front is orthogonal to the channel base.

In Case 2a, visualized in Fig. 5.4b and Fig. 5.5b, a significant reduction in the number of these transverse features occurs and yields a weak detonation; the wave in the images shown propagates through the eLMDE at 2070 m/s, approximately 85% of the characteristic CJ speed. The shadowgraph of this case indicates an increase in the curvature of the detonation front, as well as separation of the reaction zone from the incident front above a height of ~15**d**; chemiluminescence of this case confirms the majority of the emissions are localized to the two cellular features seen in the shadowgraph, with some emissions occurring above 15**d** but within the reactant layer.

In addition to the reduction in overall chemiluminescence emission strength and number of transverse wave features, Case 2a also lacks chemiluminescence at the base of the channel. The shadowgraph of this position reveals an apparent separation of shock and reaction zone. A combination of an increased flowrate for Case 2a and reduced reactant layer height caused a reduction of jet-to-jet mixing upon the partially mixed reactants entering the channel. As a result, the base of the eLMDE channel is likely largely diluted with background gas that had not yet been entrained by the emerging reactant jets.

The total separation of shock and reaction zone occurred in Case 3 upon a further reduction in reactant layer height. Figures 5.4c and Fig. 5.5c show the shadowgraph

and natural luminescence, respectively, of a decoupled shock-flame propagating at 710 m/s, approximately 30% of the characteristic CJ speed. While in the linear eLMDE facility there is no opportunity for the incident shock to couple with the reaction zone, within the annulus of an RDE this wave could lap the reaction zone and provide additional opportunities to transition to detonation, dependent upon other criteria at the time of this interaction. Despite the decoupling of the reaction zone, a number of reflected shock features are observed emanating off of the discrete injector arrays. It may be possible to intentionally space and shape these injectors such that a desirable resonance with the nominal mixture cell size is achieved in RDE.

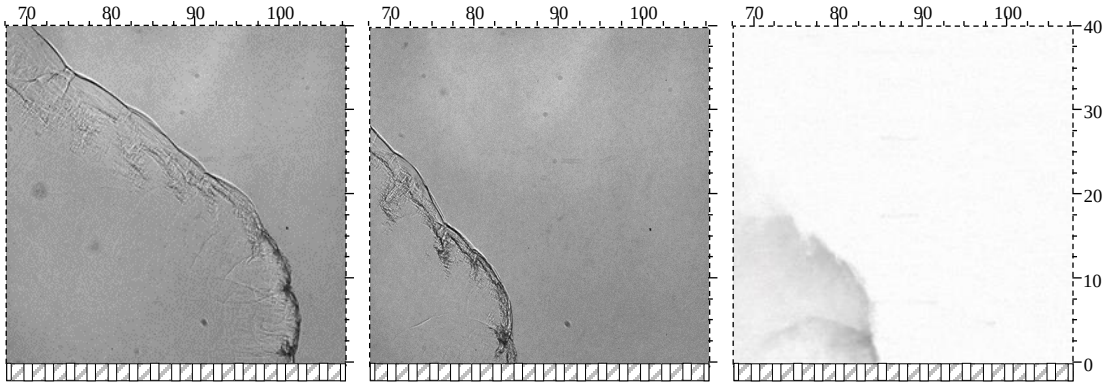

(a) Case 2a, τ_1 (b) Case 2b, τ_1 (c) Case 2b, τ_1

Figure 5.6: Shadowgraph images of (a) weak detonation propagation, and (b) decoupling detonation, and chemiluminescence of (c) decoupling detonation.

The reactant cross-flow conditions that yielded Case 2a also produced Case 2b, a detonation wave in the process of decoupling. Figure 5.6b-c shows the shadowgraph and chemiluminescence of Case 2b in comparison to the shadowgraph of Case 2a in Fig. 5.6a. While the probability of the cross-flow yielding Case 2a is equal to that of Case 2b, the range of measured wave speeds for Case 2b varies significantly; the simultaneously acquired images in Fig. 6b-c correspond to a wave propagating at 1425 m/s, or 60% of the characteristic CJ speed.

Separation of the reaction zone from the incident shock front is apparent throughout Case 2b, with the exception of where a transverse shock is present, as revealed in the chemiluminescence. Likewise, the chemiluminescence for this case is nearly uniformly distributed, similar to the luminescence of Case 3. The range in observed wave speeds for this decoupling case is likely the result of the position within the eLMDE channel where the detonation began to decay and may be the result of run-to-run variations in the reactant layer fill characteristics.

Dynamic pressure measurements corresponding to these test cases are shown in Fig. 5.7. The two pressure

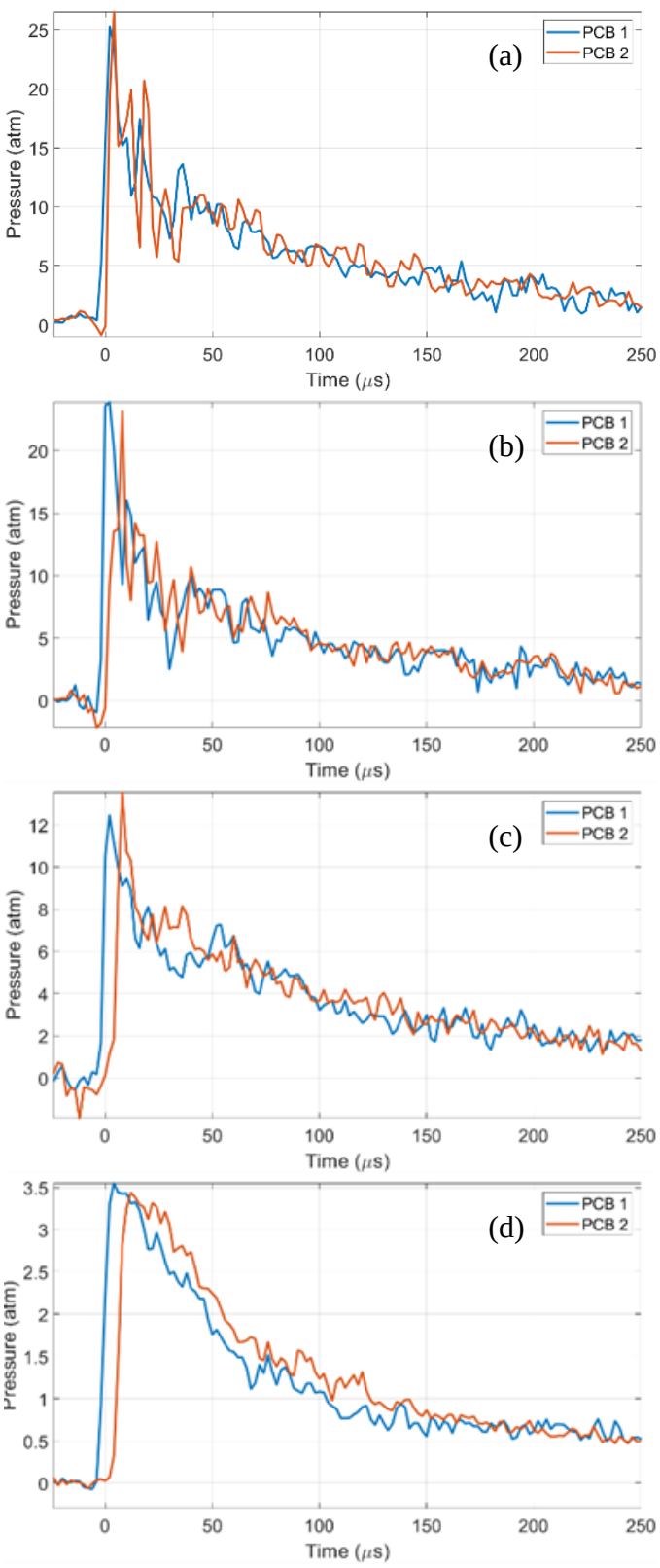

Figure 5.7: Pressure record of wave transit for (a) Case 1, (b) Case 2a, (c) Case 2b, and (d) Case 3 structures at two locations.

transducer locations referenced as PCB 1 and PCB 2 correspond to positions 2.3**d** and 17.3**d** above the base of the eLMDE channel, respectively, and are placed 69.1**d** downstream of the exit plane of the pre-detonator. These positions were chosen such that PCB 1 was always within the reactant layer while PCB 2 was near the interface of the reactant layer and background gas.

In Case 1, where the reactant layer height exceeded the position of PCB 2 and the curvature of the wave front was minimal, the dynamic pressure traces produced by the two sensors were similar. Measured pressures were of similar strength at 25-26 atm, or 86-89% of the expected one-dimensional and well-mixed CJ pressure; post-detonation pressure is not expected to agree with the one-dimensional theory due to effects such as reduced wave speed, front curvature, gaseous side relief, limited reactant mixing, and sensor response time scales. Fluctuations in the amplitude of PCB 2 were more exaggerated following the initial transit, likely due to transverse wave interactions at the material interface.

As a result of the reduction in wave speed in Case 2a, the measured pressure decreased to 23-24 atm. In this case PCB 2 was positioned near the reactant layer height and, combined with the visualized wave curvature, yielded a delay between the two measured signals. Case 2b is clearly identified from the dynamic pressure trace; despite the same reactant layer conditions the measured pressure was 12-13 atm, half that of Case 2a. Peak pressures measured in Case 3 were further reduced; the sharp pressure peak characteristic of a detonation front in Fig. 5.7a-c is replaced by a plateau in pressure that decreases smoothly for 75 μs prior to trailing reaction zone's transit of the sensor array.

Experimentally measured wave speeds for a number of tests of each case are shown in Fig. 5.8 in comparison to a simplified one-dimensional mixing model [5.39]. The model assumes that only part of the reactant layer chemically reacts and couples with the incident wave to produce the measured wave speed, while the rest of the reactant gas remains chemically inert.

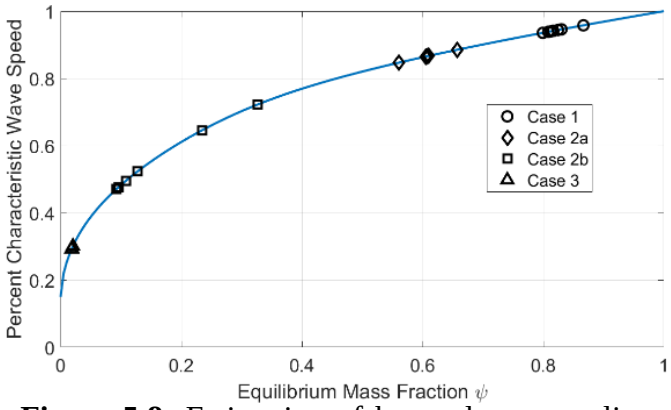

Figure 5.8: Estimation of heat release coupling with detonation wave from one-dimensional model.

According to this model Case 1, which presents with little variation in wave speed, propagates with approximately 80% heat release coupling to the incident detonation front. This qualitatively agrees with the shadowgraph and chemiluminescence of Case 1, where reaction in the inclined part of the detonation front is unlikely to meaningfully drive the detonation wave. With the exception of Case 2b, the majority of the points for each case are closely clustered in Fig. 5.8 and agree with the chemiluminescence images.

The measured wave speeds are compared to the reactant layer heights in Fig. 5.9; reactant layer heights were directly measured from the shadowgraph and

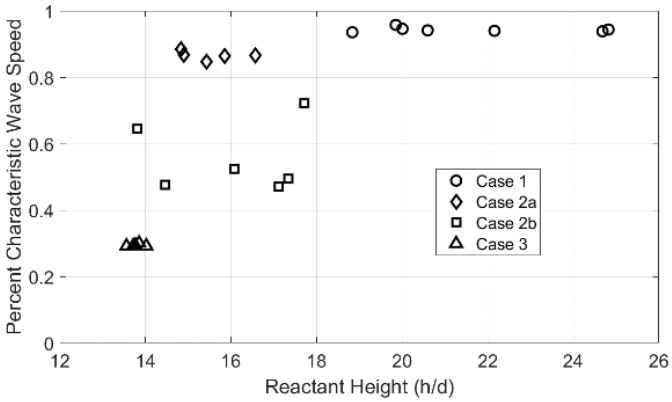

Figure 5.9: Experimentally observed wave speed compared to fill height.

chemiluminescence. Despite run to run variations in layer heights, Case 1 routinely produced a strong detonation propagating in excess of 90% of the one-dimensional and well-mixed CJ speed. Likewise, at the low height of 14**d**, Case 3 yielded repeatable decoupled shock-flames propagating at 30% of the characteristic CJ speed.

The bifurcation in results between Case 2a and Case 2b is of particular interest; even with similar fill conditions producing reactant layer heights of 14-18**d**, there were significant variations in the experimentally measured wave speed. A reactant layer that has insufficient thickness to continually generate transverse features at a rate greater than they are lost will decouple and decay in strength, as is observed in Case 2b. Due to the stochastic nature of the initial conditions in terms of mixing, layer thickness, and wave speed within the eLMDE, this critical point likely varies from run-to-run. As a result, some cases retain two or more strong transverse shocks and propagate as Case 2a at 85% of the characteristic CJ speed, and others reach this limiting value and begin to decay in Case 2b at a considerably lower speed. Of particular note is the range in layer thicknesses for this bimodal behavior; results from Fig. 9 indicate that layer heights of 18**d** are required for robust methane-oxygen detonation propagation in the configuration tested.

5.5 Conclusions

We investigated detonation and shock waves propagating across an array of reactant jets inside a narrow channel, simulating an unwrapped RDE configuration. Partially premixed gaseous methane-oxygen jets were examined, with global jet equivalence ratios approximately representative of stoichiometric operation. Experimental observations were conducted using simultaneously acquired high-speed

flow visualization techniques and high-frequency-response dynamic pressure transducers.

Propagation modes were characterized by reactant cross-flow layer heights and wave speeds. In test configurations with layer heights in excess of 18d, robust detonation waves propagating in excess of 90% of the one-dimensional CJ speed were observed. The simultaneously acquired shadowgraph and chemiluminescence images for these cases revealed a complex detonation front composed of several transverse shocks; several Mach stems and triple points were observed directly. Heat release occurred near the incident wave front, and the dynamic pressure measurements indicated a uniform strength front throughout the reactant fill layer.

For intermediate reactant layer heights in the range of 14-18**d** a bifurcation in transmitted propagation mode was observed; waves propagated through the test section as either weak detonations or decoupling detonations. Weak detonations propagated at approximately 85% of the one-dimensional CJ speed and at pressures comparable to the robust detonation waves resulting from greater fill heights. The visualized inclination of the weak detonation front resulted in a delay between the dynamic pressure transducer signals. Simultaneous shadowgraph and chemiluminescence images indicated a significant reduction in strong transverse shocks to one or two, and a broadening of the reaction zone.

Decoupling detonations were observed propagated at speeds in the range of 40-80% of the one-dimensional CJ speed; dynamic pressure measurements were similar in amplitude between the two sensor locations at approximately 50% of the pressure recorded in either the weak or robust detonation cases. Shadowgraph images revealed

separation between the incident shock and reaction zone as well as the steepening of the oblique shock in the background gas. Chemiluminescence measurements likewise showed the increase in width of the reaction zone at the reduced post-shock pressure.

At a sufficiently low reactant layer height of 14**d**, the transmitted detonation wave yielded a decoupled shock-flame propagating at 30% of the one-dimensional CJ speed. In this case the peak pressure was further reduced to less than 15% of the amplitude of the robust detonation wave. Shadowgraph visualizations showed a significant separation between the incident shock and the reaction zone, as well as several waves reflecting off the discrete injector array. Luminescence measurements indicated a uniform intensity reaction zone with no evidence of transverse wave features.

The variety of transmitted mode behavior indicates that the reactant layer height of 18**d** is likely approaching a limiting value for the gaseous methane-oxygen jets in the current injector configuration. Bifurcation in transmitted mode occurs below this reactant layer height in the range of 14-18**d**. In this range weak detonation waves propagate with two or more transverse shocks, but decoupling waves exhibit one or less transverse shock waves. At a reactant layer height of 14**d** a decoupled shock-flame propagates without any evidence of transverse shocks. The present approach of using a linear channel is well suited for understanding the RDE-relevant flowfield for different injector geometries and flow conditions and allows for visualization of features pertinent to the interaction between a detonation wave and transversely injected reactant cross-flow.

5.6 Acknowledgements

This work was supported by the United States Air Force Office of Scientific Research [grant number FA9550-17-1-0086].

5.7 References

[5.1] M. Hishida, T. Fujiwara, and P. Wolanski. Fundamentals of rotating detonations. *Shock Waves* 19(1):1-10, 2009.

[5.2] D. Schwer and K. Kailasanath. Numerical investigation of the physics of rotating-detonation-engines. *Proceedings of the Combustion Institute*, 33(2):2195-2202, 2011.

[5.3] R. T. Fievisohn and K. H. Yu. Steady-State Analysis of Rotating Detonation Engine Flowfields with the Method of Characteristics. *Journal of Propulsion and Power*, 33(1):89-99, 2017.

[5.4] K. Kailasanath. Review of Propulsion Applications of Detonation Waves. *AIAA Journal*, 38(9):1698-1708, 2000.

[5.5] P. Wolanski. Detonative propulsion. *Proceedings of the Combustion Institute*, 34(1):125-158, 2013.

[5.6] F. K. Lu and E. M. Braun. Rotating Detonation Wave Propulsion: Experimental Challenged, Modeling, and Engine Concepts. *Journal of Propulsion and Power*, 30(5):1125-1142, 2014.

[5.7] Y. T. Shao, M. Liu, and J. P. Wang. Numerical Investigation of Rotating Detonation Engine Propulsive Performance. *Combustion Science and Technology*, 182(11-12):1586-1597, 2010.

[5.8] F. A. Bykovskii and E.F. Vedernikov. Continuous detonation combustion of an annular gas-mixture layer. *Combustion, Explosion and Shock Waves*, 32(5):489:491, 1996.

[5.9] F. K. Lu, R. Miller, M. R. Nalim, and K. H. Yu. Introduction: Special Section on Pressure Gain Combustion. *Journal of Propulsion and Power*, 33(1):16, 2017.

[5.10] R. M. Clayton and R. S. Rogero. Experimental Measurements on a Rotating Detonation-Like Wave Observed During Liquid Rocket Resonant Combustion. Jet Propulsion Laboratory Technical Report No. 32-788, 1965.

[5.11] J. A. Nicholls, R. E. Cullen, and K. W. Ragland. Feasibility studies of a rotating detonation wave rocket motor. *Journal of Spacecraft and Rockets*, 3(6):893-898, 1966.

[5.12] T. C. Adamson Jr. and G. R. Olsson. Performance Analysis of a Rotating Detonation Wave Rocket Engine. *Astronautica Acta*, 13(4):405-415, 1967.

[5.13] P. I. Shen and T. C. Adamson Jr. Theoretical Analysis of a Rotating Two-Phase Detonation in Liquid Rocket Motors. *Astronautica Acta*, 17(4):715-728, 1972.

[5.14] J. Kindracki, P. Wolanski, and Z. Gut. Experimental research on the rotating detonation in gaseous fuels-oxygen mixtures. *Shock Waves*, 21(2):75:84, 2011.

[5.15] F. A. Bykovskii, S. A. Zhdan, and E. F. Vedernikov. Continuous Spin Detonations. *Journal of Propulsion and Power*, 22(6):1204-1216, 2006.

[5.16] J. R. Burr and K. H. Yu. Detonation Propagation in a Linear Channel with Discrete Injectors and Side Relief. In *26th International Colloquium on the Dynamics of Explosions and Reactive Systems*, ICDERS Paper 2017-1107, Aug. 2017.

[5.17] J. Fujii and J. Kasahara. Numerical investigation on detonation velocity in rotating detonation engine. *Proceedings of the Combustion Institute*, 36(2):2665-2672, 2017.

[5.18] S. Yao, Z. Ma, S. Zhang, M. Luan, and J. P. Wang. Reinitiation phenomenon in hydrogen-air rotating detonation engine. *International Journal of Hydrogen Energy*, 42(47):28588-28598, 2017.

[5.19] L. Deng, H. Ma, C. Xu, X. Liu, and C. Zhou. The feasibility of mode control in rotating detonation engine. *Applied Thermal Engineering*, 129(1):1538-1550, 2018.

[5.20] Y. Uemura, A. Koichi Hayashi, M. Asahara, N. Tsuboi, and E. Yamada. Transverse wave generation mechanisms in rotating detonation. *Proceedings of the Combustion Institute*, 34(2):1981-1989, 2013.

[5.21] F. A. Bykovskii, A. A. Vasil'ev, E. F. Vedernikov, and V. V. Mitrofanov. Explosive combustion of a gas mixture in radial annular chambers. *Combustion, Explosion and Shock Waves*, 30(4):510-516, 1994.

[5.22] F. A. Bykovskii and V. V. Mitrofanov. Detonation combustion of a gas mixture in a cylindrical chamber. *Combustion, Explosion and Shock Waves*, 16(5):570-578, 1980.

[5.23] Y. Shao and J. P. Wang. Continuous Detonation Engine and Effects of Different Types of Nozzle on Its Propulsion Performance. *Chinese Journal of Aeronautics*, 23(6):647-652, 2010.

[5.24] N. Tsuboi, Y. Watanabe, T. Kojima, and A. Koichi Hayashi. Numerical estimation of the thrust performance on a rotating detonation engine for a hydrogen-oxygen mixture. *Proceedings of the Combustion Institute*, 35(2):2005-2013, 2015.

[5.25] R. Zhou and J. P. Wang. Numerical investigation of flow particle paths and thermodynamic performance of continuously rotating detonation engines. *Combustion and Flame*, 159(12):3632-3645, 2012.

[5.26] C. A. Nordeen, D. Schwer, F. Schauer, J. Hoke, T. Barber, and B. M. Cetegen. Role of inlet reactant mixedness on the thermodynamic performance of a rotating detonation engine. *Shock Waves*, 26(4):417-428, 2016.

[5.27] J. Sun, J. Zhou, S. Liu, and Z. Lin. Numerical investigation of a rotating detonation engine under premixed/non-premixed conditions. *Acta Astronautica*, 152(1):630-638, 2018.

[5.28] B. A Rankin, D. R. Richardson, A. W. Caswell, A. G. Naples, J. L. Hoke, and F. R. Schauer. Chemiluminescence imaging of an optically accessible non-premixed rotating detonation engine. *Combustion and Flame*, 176(1):12-22, 2017.

[5.29] Y. Wang, J. Le, C. Wang, and Y. Zheng. A non-premixed rotating detonation engine using ethylene and air. *Applied Thermal Engineering*, 137(1):749-757, 2018.

[5.30] B. A. Rankin and F. R. Schauer. Investigation of the structure of detonation waves in a non-premixed hydrogen-air rotating detonation engine using mid-infrared imaging. *Proceedings of the Combustion Institute*, 37(3):3479-3486, 2019.

[5.31] J. Sousa, G. Paniagua, and E. C. Morata. Thermodynamic analysis of a gas turbine engine with a rotating detonation combustor. *Applied Energy*, 195(1):247-256, 2017.

[5.32] S. Zhou, H. Ma, Y. Yang, and C. Zhou. Investigation on propagation characteristics of rotating detonation wave in a radial-flow turbine engine combustor model. *Acta Astronautica*, 160(1):15-24, 2019.

[5.33] C. A. Nordeen, D. Schwer, F. Schauer, J. Hoke, T. Barber, and B. Cetegen. Thermodynamic model of a rotating detonation engine. *Combustion, Explosion, and Shock Waves*, 50:568-577, 2014.

[5.34] A. Okninski, J. Kindracki, and P. Wolanski. Rocket rotating detonation engine flight demonstrator. *Aircraft Engineering and Aerospace Technology*, 88(4):480-491, 2016.

[5.35] G. Ge, L. Deng, H. Ma, X. Liu, and C. Zhou. Effect of blockage ratio on the existence of multiple waves in rotating detonation engine. *Acta Astronautica*, 164(1):230-240, 2019.

[5.36] M. L. Fotia, J. Hoke, and F. Schauer. Study of the ignition process in a laboratory scale rotating detonation engine. *Experimental Thermal and Fluid Science*, 94(1):345-354, 2018.

[5.37] J. C. Shank. Development and Testing of a Rotating Detonation Engine Run on Hydrogen and Air. MS thesis, Air Force Institute of Technology, 2012.

[5.38] K. T Walsh and M. D. Smooke. Experimental and computational study of CH, CH*, and OH* in an axisymmetric laminar diffusion flame. *Symposium (International) on Combustion*, 27(1):615-623, 1998.

[5.39] J. R. Burr and K. H. Yu. Mixing in Linear Detonation Channel with Discrete Injectors and Side Relief. In *57th AIAA Aerospace Sciences Meeting*, AIAA Paper 2019-1014, Jan. 2019.

Chapter 6: Partial Reaction Mixing Model

The contents of this chapter include experiments of C_2H_4-O_2 and CH_4-O_2 detonations in the LMDE and eLMDE experimental facilities (Appendix B and C). Based off of these data a new model for calculating partially mixed detonation wave speeds is proposed. The text is adapted from the following conference proceedings of the 2019 AIAA Aerospace Sciences Meeting:

> J. R. Burr and K. H. Yu. Mixing in Linear Detonation Channel with Discrete Injectors and Side Relief. In *2019 AIAA Aerospace Sciences Meeting*, AIAA Paper 2019-1014, Jan. 2019.

6.1 Abstract

In rotating detonation engine (RDE) flowfields, a detonation wave often propagates through evolving reactant mixtures under partially confined geometric conditions. It is also observed that the resulting detonation wave speed in RDE is often significantly smaller than the characteristic Chapman-Jouguet wave speed for the corresponding mixture in a fully confined one-dimensional (1D) situation. In this paper, effects of incomplete mixing at the time of the detonation wave arrival in an RDE flowfield are examined both experimentally and analytically. For experimental approach, we use a linear channel with a series of fuel-oxidizer injectors to simulate an "unwrapped" RDE flowfield, and a pre-detonator to produce the properly timed detonation wave in the simulated flowfield. The reactants in the experiments are partially premixed as they enter the linear channel, and the degree of their premixing is adjusted by controlling the timing of the reactant valves and the pre-detonator initiation. For analytical approach, it is assumed that, as a consequence of the partial confinement,

only a fraction of reactants that are already premixed at the time of the wave arrival will produce the relevant heat release for sustaining the detonation wave speed. Then, the effect of partial heat release on detonation wave speed can be calculated using a 1D frozen-species equilibrium assumption. The results show the partial pre-mixing model can explain the discrepancies in experimentally observed RDE detonation wave speeds. Good agreements are found between our experimental data and the analytical results.

6.2 Nomenclature

a	sound speed
c_P	heat capacity
h	enthalpy
P	pressure
q_{in}	net heat addition
R	gas constant
T	temperature
u	velocity
X, Y, Z	experimental coordinate axes
$\bar{Y}$	species mass fractions unit vector
ρ	density
v	specific volume
γ	heat capacity ratio
ψ_{EQ}	equilibrium mass fraction

6.3 Introduction

Rotating detonation engines (RDEs) have emerged as lead candidates in the development of a practical detonation-based combustor [6.1-6.3]. In air breathing applications the potential thermodynamic benefits of detonative over constant-pressure heat addition makes such systems attractive [6.1-6.8]. Additional system properties, such as a simple design, compact reaction zone, and periodic heat addition process, are equally beneficial to both air breathing and rocket applications [6.9-6.14].

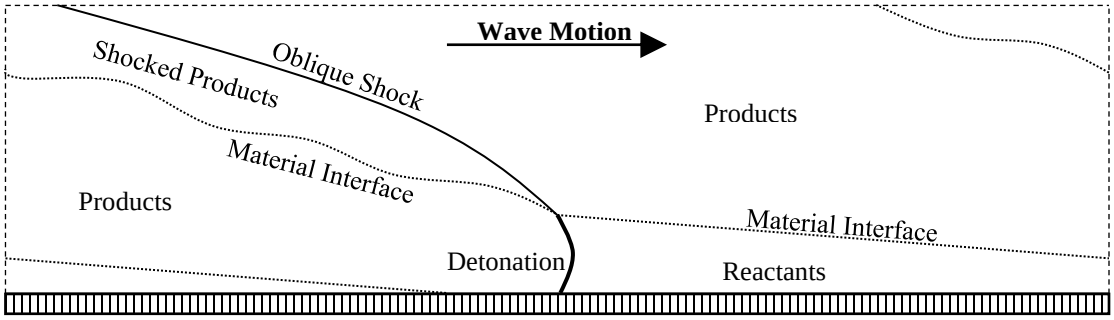

Figure 6.1: Simplified RDE/RDRE flowfield in the wave-centered reference frame.

RDE geometry is characterized by an annular channel with reactants injected in the axial direction and the detonation propagating along the azimuthal direction [6.15]. For single wave operation, the reactant refresh occurs in the time the detonation wave takes to propagate around the circumference of the annular channel. Reactant confinement, as shown in the detonation reference frame in Fig. 6.1, occurs on the sides by the annulus wall, above by the hot products from the previous detonation cycle, and below by the reactant injection plane. Figure 6.1 shows reactant injection occurring immediately in the wake of the incident detonation. However, the pressure rise associated with the detonation structure abruptly halts reactant inflow, and may result in some backflow of combustion products unless the stagnation pressure of the reactant jets exceeds the post-detonation pressure. Reactant injection resumes when the local pressure within the annulus drops to below the jet stagnation pressure.

In general, the injection of reactants occurs at discrete intervals, resulting in a cross-flow composition that varies with azimuthal position within the RDE annulus. This composition must remain sufficiently detonable in spite of problems associated with localized mixing between fuel and oxidizer species, contamination with hot products from the previous detonation transit, critical heights required to sustain transverse waves along the detonation front, and deflagrations forming between the

fresh reactants and hot products. In configurations where the cross-flow is not able to sustain a detonation, the decoupling of the reaction zone from the shock in the detonation front may occur.

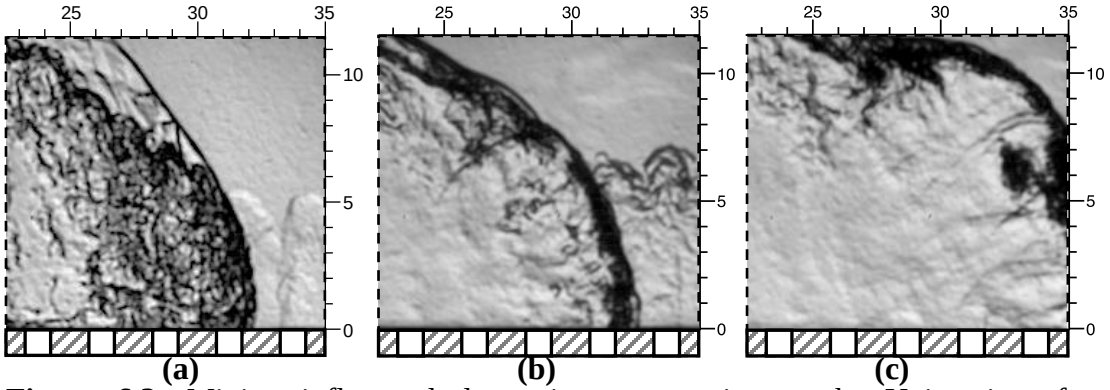

Figure 6.2: Mixing influenced detonation propagation at the University of Maryland. Schlieren of detonation in (a) H_2/O_2 mixture, and in C_2H_4/O_2 mixture at times (b) τ_1 and (c) $\tau_1 + 5\mu s$.

Experiments at the University of Maryland have revealed a number of configurations that show evidence of reduced coupling between the reactant cross-flow and the incident wave front. Figure 6.2 illustrates two such configurations; in Fig. 6.2a a H_2/O_2 reactant cross-flow shows evidence of a distributed reaction zone, and Fig. 6.2b-c shows a large pocket of C_2H_4/O_2 cross-flow passing through the wave front (at normalized dimensions X=33**d**, Y=6**d**) without reacting. In both cases evidence of global or localized mixing is present and necessitates a reduction in the expected wave speed as a result in a loss in the global heat release.

The objective of this study is to examine the reduced propagation velocity of detonation waves through partially mixed reactant species. The analytical approach is to simplify the complex RDE flowfield into a one-dimensional and analogous reactant composition that is comprised of both chemically inert and reactive species to replicate the impact of incomplete mixing in the RDE. Experiments capture the physics of the

RDE by “unwrapping” the annular channel into a linear analog that otherwise mimics the injection geometry of RDEs. The experimental results are then compared to the partial mixing model of partially mixed detonation wave speeds.

6.4 Experimental Setup

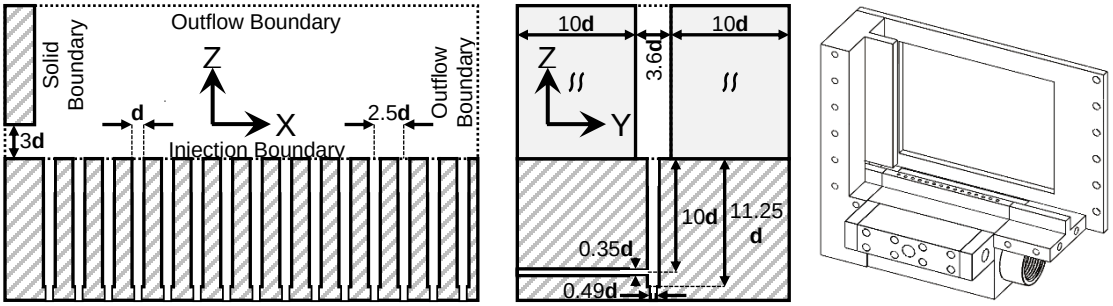

Figure 6.3: Cross-section of LMDE channel in the X-Z (left) and Y-Z (middle) planes, with X-Y-Z forming a right-handed coordinate system. Isometric view of facility shown with windows and near window holder removed (right). Dimensions normalized by injection tube diameter, **d**.

The Linear Model Detonation Engine (LMDE) facility is shown in Fig. 6.3 in multiple perspectives; dimensions are normalized by recessed tube diameter **d**, 0.1-inch. Width of the LMDE channel (Y direction) is 3.6**d**. Design of the LMDE integrates elements of the AFRL’s 6-inch RDE [6.16] and the NRL’s premixed microinjection system [6.2]. Recessed tubes used for reactant injection (Z<0) are not visualized in the current LMDE configuration. Confinement of reactant species is provided on the sides by the quartz windows and below by the injection plane.

Reactant flow propagating in the positive Z direction simulates RDE inflow. Within the fifteen recessed cylindrical tubes (L/D of 11.25), fuel and oxidizer impinge at a depth of 10**d** relative to the bottom of the LMDE channel as illustrated in Fig. 6.2, which allows for partial premixing of the reactant species. Independent solenoid control

for each reactant allows for control over the height of the partially premixed reactant layer just prior to detonation transit.

A pre-detonator with internal diameter of 4.3**d** and L/D of 42 generates a detonation propagating in the positive X direction into the reactive cross-flow within the LMDE. A transition piece converts the circular cross-section to a rectangular one with sides measuring 3**d** and 3.6**d**. The pre-detonator operates using a stoichiometric mixture of hydrogen and oxygen, with fill times varied to control the strength of the wave entering the LMDE. An electric spark from an automotive ignition system using an iridium tipped spark plug initiates combustion.

6.5 Analytic Framework

Traditional analysis of detonation wave speed assumes a one-dimensional, well mixed, and quiescent gas. Jump conditions for the conservation of mass, momentum, and energy, as well as the ideal gas equation of state, are:

$$\rho_1 u_1 = \rho_2 u_2 \tag{6.1}$$

$$P_1 + \rho_1 u_1^2 = P_2 + \rho_2 u_2^2 \tag{6.2}$$

$$c_{P,1} T_1 + \frac{1}{2} u_1^2 + q_{in} = c_{P,2} T_2 + \frac{1}{2} u_2^2 \tag{6.3}$$

$$P = \rho R T \tag{6.4}$$

For calorically perfect gases, the heat capacities at initial and final states can be assumed to be constant; however, for real gases the heat capacities will differ between the two states due to the substantial change in pressure, temperature, and species composition. Conservation of mass and momentum equations yields the Rayleigh line:

$$\frac{P_2}{P_1} = \left[-\frac{u_1^2}{P_1 v_1}\right] \cdot \frac{v_2}{v_1} + \left[1 + \frac{u_1^2}{P_1 v_1}\right] \tag{6.5}$$

Where in *P-v* space the slope of the Rayleigh line is dependent on the incident wave speed, u_2. Conservation of mass, momentum, and energy, in addition to the equation of state, yield the Hugoniot curve:

$$\frac{P_2}{P_1} = \frac{\left[\frac{\gamma_1+1}{\gamma_1-1} + \frac{2\gamma_1}{\gamma_1-1} \cdot \hat{q}\right] - \frac{v_2}{v_1}}{\left[\frac{\gamma_2+1}{\gamma_2-1}\right]\frac{v_2}{v_1} - 1}, \qquad \hat{q} = \frac{q_{in}}{c_{P,1} T_1} \tag{6.6}$$

For calorically imperfect gases, solutions to Eqn. 6.6 require knowledge of the heat capacity ratio (γ) as a function of pressure, temperature, and species composition. In this analysis, Cantera is used with appropriate mechanism files, *h2air_highT* for hydrogen and *gri30_highT* otherwise, to model the chemical kinetics and thermodynamics of the gases used. Equation 6.3 is modified to make used of Cantera's internal tracking of mixture enthalpy:

$$h_1 + \tfrac{1}{2}u_1^2 = h_2 + \tfrac{1}{2}u_2^2 \tag{6.7}$$

The net heat added to the flow is tracked in Cantera through the formation and destruction of gas species, and is included within h_1 in Eqn. 6.7.

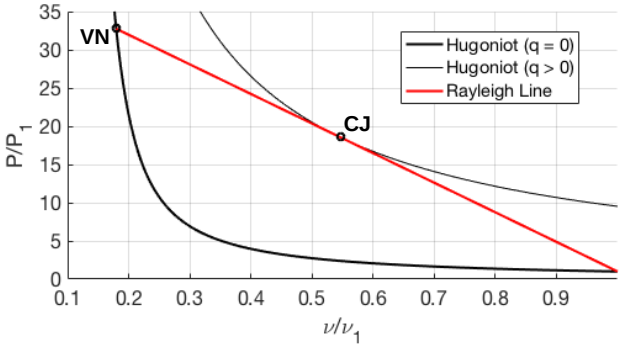

Figure 6.4: Hugoniot curves for stoichiometric H_2/O_2 in *P-v* space. CJ and von Neumann points included.

Figure 6.4 examines the Hugoniot curves and Rayleigh line for a stoichiometric H_2/O_2 mixture. Gas species match the reactants along the curve with no heat release ($q=0$), while species are in equilibrium concentrations along the curve with heat release ($q>0$). The Rayleigh line tangent to the Hugoniot with heat release ($q>0$) is shown in Fig. 6.4 with corresponding CJ and von Neumann points. Solving for when Eqn. 6.5 is tangent to Eqn. 6.6 yields the following well-known relationship for this minimum wave speed (the CJ speed, V_{CJ}):

$$\frac{V_{CJ}^2}{a_1^2} = \left[\frac{\gamma_2^2-1}{\gamma_1-1}(1+\hat{q}) - \gamma_1\left(\frac{\gamma_2}{\gamma_1}\right)^2\right] + \sqrt{\left[\frac{\gamma_2^2-1}{\gamma_1-1}(1+\hat{q}) - \gamma_1\left(\frac{\gamma_2}{\gamma_1}\right)^2\right]^2 - \left(\frac{\gamma_2}{\gamma_1}\right)^2} \tag{6.8}$$

The simplest approach to model mixing limited detonation propagation is to decrease the value of $\hat{q}$; as the fraction of reactants that chemically react decrease the net heat available must decrease. Inspection of Eqn. 6.8 indicates that $V_{CJ} \propto \sqrt{\hat{q}}$. However, because the relationship between γ_2 and $\hat{q}$ is a function of the pressure, temperature, and species concentrations, directly determining the decrease in V_{CJ} from this approach is not tractable.

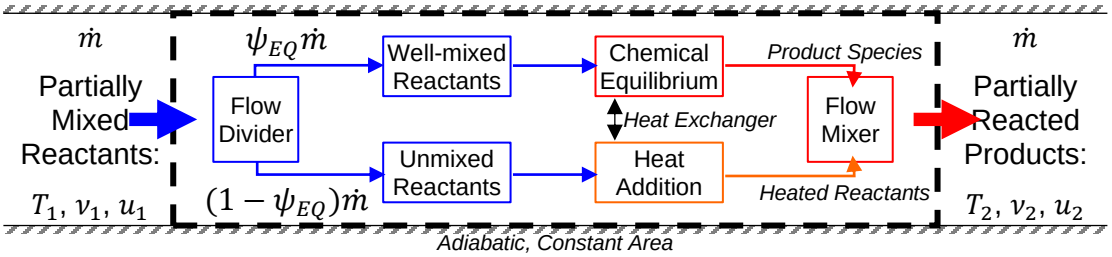

Figure 6.5: Partial mixture detonation model for constant area configuration.

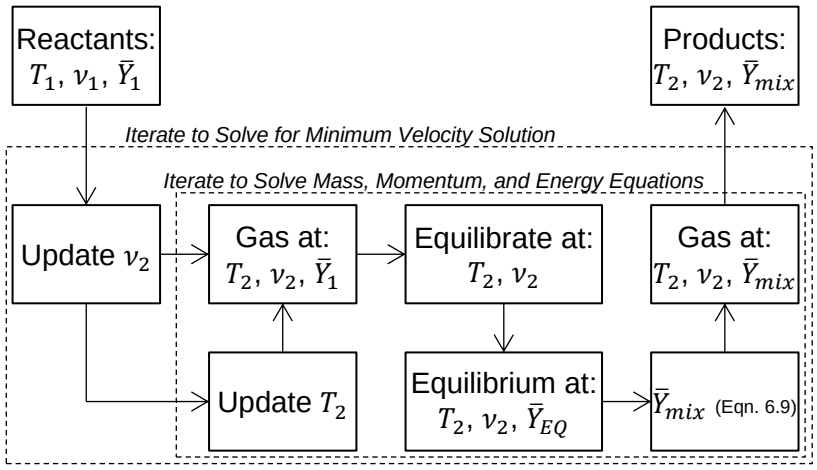

Figure 6.6: Pseudocode for Cantera based iterative partial mixture detonation model.

A simple model to assess the decrease in V_{CJ} due to reactant mixing is illustrated in Fig. 6.5, and the corresponding pseudocode for Cantera implementation is in Fig. 6.6. The extent of mixing is quantified with the parameter ψ_{EQ}, which represents the mass fraction of gas in equilibrium at the final, partially reacted state. This fraction of well-mixed reactants is equilibrated at some final state given by T_2 and ν_2, yielding a species composition $\bar{Y}_{EQ}$. The remaining fraction of unmixed reactants is brought to the same temperature and specific volume; although these reactants are considered chemically inert, heat transfer occurs between the two gas mixtures. The two gas fractions are combined at constant temperature and specific volume, yielding the partially reacted mixture mass fractions:

$$\bar{Y}_{mix} = (\psi_{EQ}) \cdot \bar{Y}_{EQ} + (1 - \psi_{EQ}) \cdot \bar{Y}_1 \tag{6.9}$$

As illustrated in Fig. 6.6, the final temperature T_2 is selected such that conservation of mass, momentum, and energy occurs between the reactants and partially reacted products; the final specific volume v_2 is selected to find the tangency of the Rayleigh line to the partially reacted Hugoniot curve.

Figure 6.7 displays select curves of constant equilibrium mass fraction for a stoichiometric H_2/O_2 mixture. As $\psi_{EQ} \rightarrow 1$, the Hugoniot curve with heat release ($q>0$) from Fig. 6.4 is recovered, and as $\psi_{EQ} \rightarrow 0$ the Hugoniot curve without heat release ($q=0$) is recovered. The locus of mixing limited CJ points for $0 \leq \psi_{EQ} \leq 1$ is shown in Fig. 6.7.

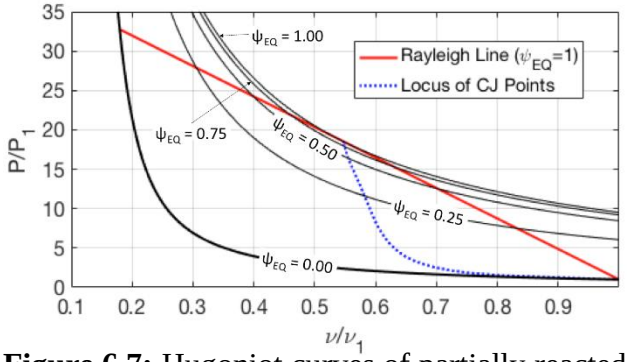

Figure 6.7: Hugoniot curves of partially reacted stoichiometric H_2/O_2 in *P-v* space. Rayleigh line for full heat release and locus of CJ points included.

6.6 Results and Discussion

Mixing limited detonation wave speeds were calculated for a number of stoichiometric reactant mixtures and are shown in Fig. 6.8; Figure 6.8a shows the value of these CJ speeds, while Fig. 6.8b normalizes the CJ speed with the expected CJ speed for a well-mixed and fully reacted mixture of the same initial composition. For all reactant mixtures the CJ speed was the bulk sound speed of the reactants when the equilibrium mass fraction was zero, and approached the well-mixed CJ speed for the

mixture as the equilibrium mass fraction approached one. In all cases the trend between CJ speed and equilibrium mass fraction, and therefore the amount of heat release to the flow, agrees with Eqn. 6.8 in that $V_{CJ} \propto \sqrt{\psi_{EQ}}$. Although only two hydrocarbon fuels are represented in Fig. 6.8, the behavior of C_2H_6 and C_3H_8 closely matches that of CH_4 and C_2H_4 and were omitted for clarity.

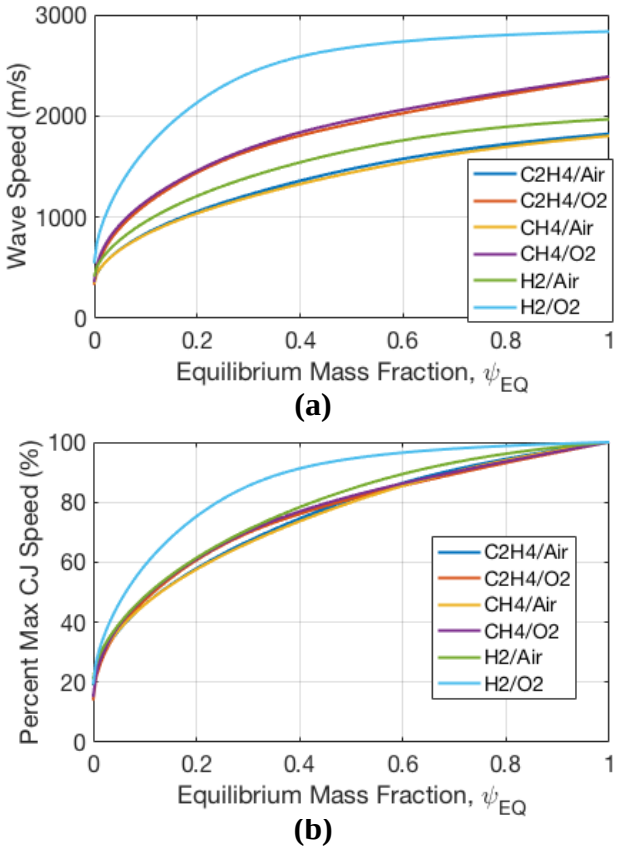

Figure 6.8: Mixture limited CJ speeds for various stoichiometric mixtures.

Figure 6.8b highlights the difference between H_2/O_2 detonations and all of the remaining reactant mixtures, including H_2/Air. While all mixtures are initially highly sensitive to the amount of equilibrium mass fraction, the normalized wave speeds follow similar trend lines as equilibrium mass fraction increases. For most mixtures this means that $\psi_{EQ} \approx 0.5$ produces a detonation propagating near 80% of the well mixed CJ speed for the mixture.

In H_2/O_2 mixtures, however, 80% of the well-mixed CJ speed is reached at a much lower value of $\psi_{EQ} \approx 0.25$. In comparison to other mixtures, only a small fraction of reactants in a H_2/O_2 detonation need to react to produce substantial detonation speeds; the trend line for the H_2/O_2 case shows that only ~40% of the

reactants need to contribute to driving the wave to reach ~90% of the well-mixed CJ speed.

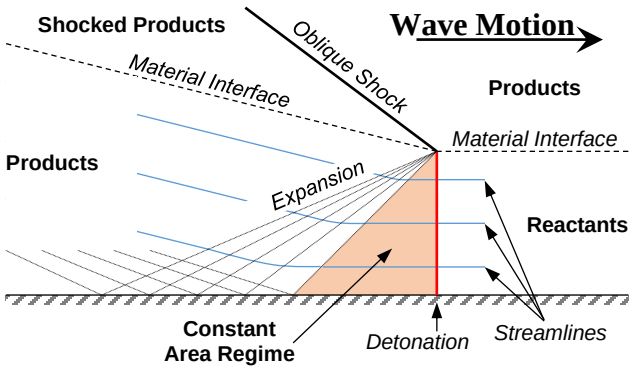

Figure 6.9: Significant flow features and regions in simplified layered detonation propagation.

In a purely one-dimensional flow-field, such as in a pulse detonation engine (PDE), any unburned reactants behind these mixing limited CJ waves will continue mixing and burning. These subsequent reactions would eventually influence the incident wave, driving it towards the well-mixed CJ speed. In the RDE the inevitable expansion of the species behind the detonation wave limits the interaction of this delayed heat release with the incident wave.

Figure 6.9 shows the flow features of a simplified detonation propagating through a reactant layer, as in RDE. This illustration assumes a planar detonation propagating normal to a wall into reactants uniformly confined above by the combustion products from a previous detonation transit; the illustration neglects non uniformities in the shape of the material interface, the presence of transverse waves, and other details of detonation propagation. For example, an inclined detonation would produce an oblique shock or expansion fan anchored at the detonation/wall interface, depending on the angle of inclination.

An oblique shock and expansion fan are required where the detonation meets the initial reactant/product material interface to maintain a pressure match across this material interface. As a result the gas streamlines behind the detonation wave diverge through this expansion fan. In this simplified configuration reactant streamlines are

one-dimensional prior to their interaction with this expansion fan. Bound by the detonation wave, reactant injection plane, and start of the expansion fan, this "constant area regime" is largest at the base of the annular channel, and approaches zero length for the streamline that represents the material interface. Static pressure and temperature drop as the streamline traverses the expansion fan, leading to a drop in chemical reactivity; streamlines near the material interface, which quickly traverse the constant area regime, likely experience chemical quenching.

The proposed partial mixing model for mixing limited CJ speeds is defined within the constant area regime, where the flow is one-dimensional. Unreacted reactants within the model will likely react after passing through the expansion fan in Fig. 6.9, but it is assumed that because of this expansion their heat release will not influence the detonation propagation, leading to the mixing limited

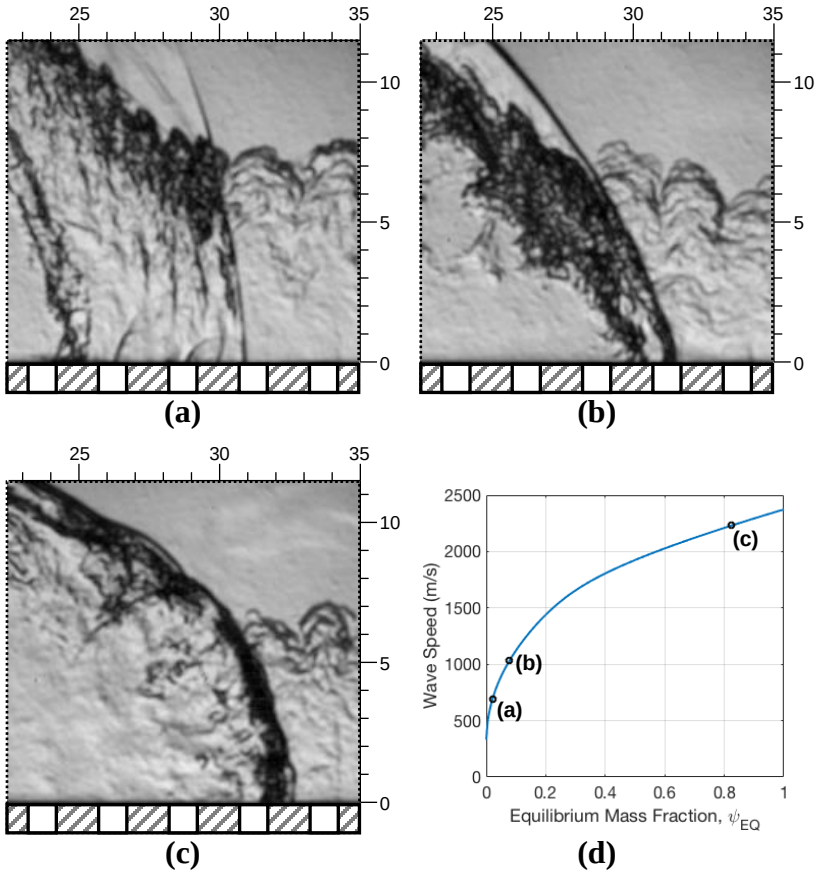

Figure 6.10: Schlieren of stoichiometric C_2H_4/O_2 waves at: (a) 690 m/s, (b) 1030 m/s, and (c) 2230 m/s. Percent of reaction driving wave front estimated as 2%, 8%, and 82% for cases (a)-(c), respectively. Wave speed curve for stoichiometric C_2H_4/O_2 detonations shown in (d).

CJ speeds in Fig. 6.8.

Comparisons of the partial mixing model to experimental results for stoichiometric C_2H_4/O_2 detonations are made in Figure 6.10. For these tests cases the reactant composition of the LMDE cross-flow is held constant, but the degree of reactant mixing and incident wave speed were varied. The schlieren images in Fig. 6.10 correspond to (a) a blast wave, (b) a reaction zone closely coupled to a shock wave, and (c) a detonation.

The schlieren of the blast wave indicate relatively weak compression of the reactant cross-flow. Luminescence images of this configuration provided little signal, indicative of little to no chemistry behind the wave. Using the transmitted wave speed, the mixing model indicates less than 2% of the reactants are releasing energy that drives the wave, which is in good agreement.

The wave front in Fig. 6.10b does not resemble that of a typical detonation, but does include a steady reaction zone closely following a shock wave; transverse waves are not present along the front and the reaction zone is relatively thick. In this test case the C_2H_4/O_2 cross-flow appears to fully react, but due to the inclination of the incident wave front, most of these reactions are occurring outside of the constant area regime. Despite the cross-flow burning, the mixing model indicates that only 8% of the reactants are releasing energy that is influencing the wave speed.

Finally, the wave front in Fig. 6.10c resembles that of a typical detonation in cross-flow. The wave front is largely normal to the propagation direction, with a slight inclination of the wave front as the top of the reactant layer is approached. The detonation front itself is characterized by a thin reaction zone and a number of

transverse waves. Dark spots in the schlieren image in the wake of the wave transit indicate some reactants did not contribute to driving the forward wave speed; application of the partial mixing model suggests that approximately 82% of the reactants are contributing to the forward wave speed in this case.

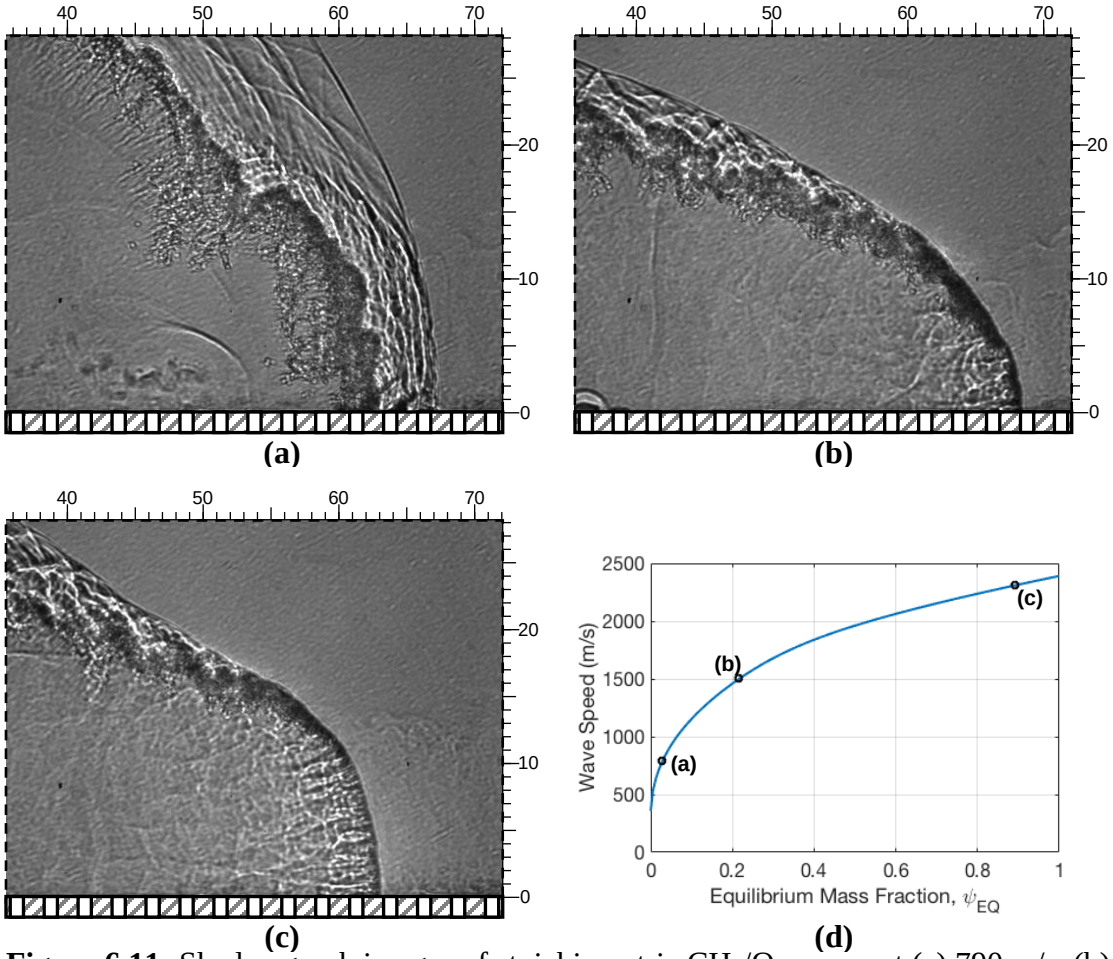

Figure 6.11: Shadowgraph images of stoichiometric CH_4/O_2 waves at (a) 790 m/s, (b) 1500 m/s, and (c) 2310 m/s. Percent of reaction driving wave front estimated as 3%, 22%, and 89% for cases (a)-(c), respectively. Wave speed curve for stoichiometric CH_4/O_2 detonations shown in (d).

Additional experiments of steady waves through stoichiometric CH_4/O_2 reactants are shown in Fig. 6.11a-c. As before, reactant composition of the cross-flow in the LMDE channel was held constant, but the degree of mixing and incident wave speed were varied by controlling solenoid timing for LMDE and pre-detonator gasses,

respectively. These three test cases correspond to (a) a blast wave, (b) a weak detonation, and (c) a strong detonation transit.

The shadowgraph of the blast wave indicates a chaotic region of pressure waves immediately behind the wave front. Deflagration of the reactant cross-flow in the wake of the weak wave leads to the shedding of pressure waves that, because the flow is subsonic, reinforce the incident wave front. Because the combustion is occurring well behind the wave front, however, the energy transfer is negligible, and as little as 3% of the CH_4/O_2 reactants are estimated to be driving the wave front.

The flow-field of Fig. 6.11b, corresponding to the weak detonation, includes many of the features expected of the RDE flow-field as presented in Fig. 6.1 and Fig. 6.9. Despite the increase in wave speed, the wave front is poorly defined at points; from Y=5-10**d** the front thickness continues to expand until it blends in with the material interface between the detonation products and shocked background gas. This broadening is likely the result of either the expansion fan in Fig. 6.9, or the result of increasingly poor reactant mixing as greater heights in the reactant crossflow. Because the LMDE reactants are not premixed and is filled transiently, the local mixedness likely varies with cross-flow evolution. Despite this, the wave propagates at approximately 60% of the well-mixed CJ speed, with an estimated 22% of the reactants contributing to the forward wave propagation.

Figure 6.11c showcases a well-defined detonation wave. In this case the wave front thickness is relatively thin throughout the cross-flow layer, and the wave front only curves back near the edge of the cross-flow where the reactants likely mixed more thoroughly with background gasses. Numerous transverse waves characterize this wave

front, which propagates in excess of 95% of the well-mixed CJ speed and with approximately 89% of the reactants driving the wave front.

6.7 Summary and Conclusions

We investigated the transit of detonation waves in reactant cross-flows of various levels of mixedness, simulating the evolving reactant flowfield of an "unwrapped" rotating detonation engine, and proposed a simple partial mixing model to determine the reduction in CJ wave speed as a function of reactant mixing. Experimental observations of partially premixed gaseous ethylene-oxygen with oxygen confinement, and of partially premixed gaseous methane-oxygen with oxygen confinement, were made using high-speed flow visualizations. Comparison of the experimental results to the proposed mixing model show good qualitative agreement with the amount of reactants contributing to the wave propagation.

The simplified model proposes that under poorly mixed reactant conditions the post detonation products are composed of two constituents: equilibrium products at some temperature and pressure, and unreacted pockets of fuel and oxidizer at the same temperature and pressure. The unreacted fuel and oxidizer do not contribute to the global heat release, reducing the CJ wave speed. Conservation of mass, momentum, and energy equations for a one-dimensional flow, as well as the mass fraction of equilibrium products, uniquely determine the CJ speed.

Application of the one-dimensional mixing model is possible in the RDE in the immediate wake of the detonation transit, prior to streamline divergence through an expansion fan. Visualization of RDE experiments indicates that where streamlines spend little time in this regime, near the top of the reactant layer, there is a broadening

of the reaction zone that may be the result of reaction quenching due to temperature and pressure drop through the expansion fan. This aggregate reduction in chemistry, integrated across all reactant streamlines, is representative of the unreacted fuel and oxidizer species in the proposed mixing model. When comparisons of the experimentally visualized wave speeds are made to the mixing model, the indicated levels of reaction occurring within this constant-area regime are within expectations.

The approach of using a simplified one-dimensional mixing model to estimate the reduction in propagation speed is well suited for RDE operation. Flow in the immediate wake of the detonation transit is limited to constant area regimes, which allow for use of such a model. The high-quality experimental visualizations allowed for insights into the coupling of the heat release with the wave transit, as estimated by the mixing model. Additionally, this model is an important tool in understanding the operability of RDE and its crucial dependence on reactant mixing, where sustaining wave motion is essential in achieving pressure gain.

6.8 Acknowledgments

This material is based upon work supported by the U.S. Air Force Office of Scientific Research under grant number FA9550-17-1-0086 with Dr. Chiping Li as the program manager.

6.9 References

[6.1] M. Hishida, T. Fujiwara, and P. Wolanski. Fundamentals of rotating detonations. *Shock Waves*, 19(1):1-10, 2009.

[6.2] D. Schwer and K. Kailasanath. Numerical investigation of the physics of rotating-detonation-engines. *Proceedings of the Combustion Institute*, 33(2):2195-2202, 2011.

[6.3] R. T. Fievisohn and K. H. Yu. Steady-State Analysis of Rotating Detonation Engine Flowfields with the Method of Characteristics. *Journal of Propulsion and Power*, 33(1):89-99, 2017.

[6.4] F. A. Bykovskii and E.F. Vedernikov. Continuous detonation combustion of an annular gas-mixture layer. *Combustion, Explosion and Shock Waves*, 32:489:491, 1996.

[6.5] K. Kailasanath. Review of Propulsion Applications of Detonation Waves. *AIAA Journal*, 38(9):1698-1708, 2000.

[6.6] P. Wolanski. Detonative propulsion. *Proceedings of the Combustion Institute*, 34(1):125-158, 2013.

[6.7] F. K. Lu and E. M. Braun. Rotating Detonation Wave Propulsion: Experimental Challenged, Modeling, and Engine Concepts. *Journal of Propulsion and Power*, 30(5):1125-1142, 2014.

[6.8] Y. T. Shao, M. Liu, and J. P. Wang. Numerical Investigation of Rotating Detonation Engine Propulsive Performance. *Combustion Science and Technology*, 182(11-12):1586-1597, 2010.

[6.9] F. K. Lu, R. Miller, M. R. Nalim, and K. H. Yu. Introduction: Special Section on Pressure Gain Combustion. *Journal of Propulsion and Power*, 33(1):16, 2017.

[6.10] R. M. Clayton and R. S. Rogero. Experimental Measurements on a Rotating Detonation-Like Wave Observed During Liquid Rocket Resonant Combustion. Jet Propulsion Laboratory Technical Report No. 32-788, 1965.

[6.11] J. A. Nicholls, R. E. Cullen, and K. W. Ragland. Feasibility studies of a rotating detonation wave rocket motor. *Journal of Spacecraft and Rockets*, 3(6):893-898, 1966.

[6.12] T. C. Adamson Jr. and G. R. Olsson. Performance Analysis of a Rotating Detonation Wave Rocket Engine. *Astronautica Acta*, 13(4):405-415, 1967.

[6.13] P. I. Shen and T. C. Adamson Jr. Theoretical Analysis of a Rotating Two-Phase Detonation in Liquid Rocket Motors. *Astronautica Acta*, 17(4):715-728, 1972.

[6.14] J. Kindracki, P. Wolanski, and Z. Gut. Experimental research on the rotating detonation in gaseous fuels-oxygen mixtures. *Shock Waves*, 21(2):75:84, 2011.

[6.15] F. A. Bykovskii, S. A. Zhdan, and E. F. Vedernikov. Continuous Spin Detonations. *Journal of Propulsion and Power*, 22(6):1204-1216, 2006.

[6.16] J. C. Shank. Development and Testing of a Rotating Detonation Engine Run on Hydrogen and Air. MS thesis, Air Force Institute of Technology, 2012.

Chapter 7: Conclusions

7.1 Concluding Remarks

Numerous experimental and computational efforts are underway with the goal of improving the understanding and development of Rotating Detonation Engine (RDE). Research is hindered on both fronts by the complex nature of the RDE flowfield; experimental diagnostics attempt to capture the large amplitude and short time scale measurements necessary, while computational efforts are limited by the extent of available data for validation efforts. Lacking a simple closed-form analytical framework to explain the myriad of reported RDE behavior, research has advanced through the comprehensive exploration of iterative design.

A linear RDE analog, like the Extended Linear Model Detonation Engine (eLMDE) experimental facility, allows for the direct study of fundamental phenomena at the heart of RDE design. Reactant species of varied fuel-oxidizer mixtures are injected into a linear channel, subjected to a detonation wave from a pre-detonator, and the subsequent detonation-reactant interaction is examined using high-quality optical visualizations and time-resolved diagnostics. Although a linear facility is limited to one or two detonation transits per test, and therefore does not reach the “steady” flowfield of a continuous detonation in RDE, the resulting detonation-reactant interactions and the subsequent reactant refresh yield numerous insights into experimentally observed phenomena in RDE. Experimentally observed detonation modes, reactant conditions, wave structures, and reactant refresh characteristics are all readily producible for

fundamental study in the linearized facility. Additionally, the data generated by the detonation transits are a valuable tool in the validation, development, and support of numerical works.

This approach to study the RDE flowfield was developed as a means to experimentally study the fundamental features of a detonation wave propagating orthogonal to discretely spaced reactant jets; eLMDE facility design was in part informed by experimental and computational RDE combustors, and the resulting detonation experiments are pertinent to analogous research efforts. The direct visualizations of these interactions have demonstrated the significance of mixing in regard to nearly every aspect of the RDE flowfield. A simplified model was developed to demonstrate that poor reactant mixing, leading to long reactant induction time scales, is one possible source of the experimentally measured "velocity deficit" in comparison to the one-dimensional CJ wave speeds. Current efforts are underway to examine additional features pertinent to RDE, such as the reignition process associated with the counter-propagating detonation wave mode (or slapping/clapping) that often results from high mass flow rate RDE operation. The work presented here helps to explain a number of detonation features relevant to RDE, as well as provide a tool for the subsequent investigation of countless RDE flowfield phenomena.

7.2 Summary of Contributions

High-quality optical visualizations of the RDE flowfield were captured for the first time in a linear analog. Design of this novel facility, the Extended Linear Model Detonation Engine (eLMDE), incorporated partially mixed and recessed injectors characteristic of numerical studies from the Naval Research Laboratory, and geometric

dimensions such as channel width, height, and injector size and spacing from existing efforts at the Air Force Research Laboratory at Wright-Patterson Air Force Base.

The eLMDE geometry permitted the study of channel-confined detonation through partially-mixed reactant cross-flow of various propellant compositions, including H_2/O_2, H_2/Air, C_2H_4/O_2, and CH_4/O_2. Schlieren, shadowgraph, luminescence, and chemiluminescence images of these waves were captured for the first time by Phantom v2512 cameras illuminated with a 640nm CAVILUX Smart pulsed diode laser at acquisition rates of 30-500kHz. Dynamic pressure and photomultiplier measurements were collected at 500-750kHz.

In the absence of reactant cross-flow, regular shock reflections were observed from the discrete injector array. The generation and propagation of these transverse features could be the source of the triple points required to propagate a detonation wave. Design of RDE injector geometries may benefit from resonance matching between these injector reflections and the nominal transverse wave spacing in planar detonation waves that occur as a result of well-mixed reactant characteristics.

Visualizations of the detonation waves yielded insight into the importance of non-uniform pre-mixing between the fuel, oxidizer, and product (previous cycle) species present in RDE. Hydrogen-oxygen experiments in particular were sensitive to the local cross-flow composition; wave speeds for globally stoichiometric cross-flow compositions were observed to fluctuate in the range of 1200-1500 m/s, or 43-54% of the well-mixed and one-dimensional Chapman-Jouguet (CJ) speed. Acceleration of these H_2/O_2 waves to 85% of the well-mixed and one-dimensional CJ speed occurred in tandem with a noticeable thinning of the reaction zone as observed in schlieren and

shadowgraph visualizations. In the case of C_2H_4/O_2 detonations, non-stoichiometric mixtures both at the jet tips and within the jet core allowed for the convection of unburned reactant pockets into the high-pressure post-detonation region. The subsequent combustion of these pockets often produced pressure waves that interacted with the incident detonation front. For C_2H_4/O_2 cases where the reactant cross-flow was confined by combustion products, an abundance of product gas was able to decouple the detonation wave. As observed in the luminescence, mixing of the fuel and oxidizer species was limited to within the jet core, and jet to jet mixing was minimal. As a result, a large quantity of non-reactive product gas remained within the reactant layer.

Direct visualizations were made of triple points within the detonation structure. In the case of H_2/Air detonations these features were tracked by the cusping of the detonation front in schlieren images. These cusps appeared to propagate upwards and away from the injector array, alluding to the role of the injector reflections previously discussed. Due to a thinner reaction zone, in C_2H_4/O_2 and CH_4/O_2 experiments transverse wave features were directly observed along the wave front. Some of these waves were generated by the volumetric expansion of reactant pockets burning downstream of the incident wave, or by the strong ignition of reactants at the jet tip where transverse waves reflect off of the material interface with the background gas.

Propagation modes and heat release coupling were examined for both C_2H_4/O_2 and CH_4/O_2 detonations. Depending upon mixing characteristics and height of the cross-flow, robust, weak, decoupling, and decoupled detonations were observed. In the case of C_2H_4/O_2 detonations, these corresponded to 2230 m/s, 1030 m/s, and 690 m/s waves, whereas in CH_4/O_2 detonations speeds of 2260 m/s, 2070 m/s, 1425 m/s, and

710 m/s were observed. Dynamic pressure and luminescence/chemiluminescence measurements both confirm that as the wave speed decreases so too does the front uniformity. For both gas compositions, the shock-flame interactions represented by the lowest observed speeds (690 m/s and 710 m/s) resulted when an insufficient number of triple points were present; for CH_4/O_2 the critical number of triple points required to propagate the detonation was approximately two.

First of their kind visualizations of the reactant refresh process following the transit of a C_2H_4/O_2 detonation yielded new insight. Initial reactant injection into the channel resumed 50–75 μs after the wave transit. Reactant jets remained discrete and poorly mixed for another 100 μs; by this time the combustion products confining the reactant layer were nominally uniform in appearance. Thorough mixing between adjacent reactant jets and entrained background gas took nearly 250 μs in total. Variations in the recovery characteristics of reactant jets was identified and attributed to feed plenum acoustic excitation driven by the detonation transit of the injector array.

As a result of the observations made for H_2/O_2, H_2/Air, C_2H_4/O_2, and CH_4/O_2 detonations, an analytical partial mixing model was developed to, in part, explain the experimentally observed “velocity deficit” phenomena. The model partitions reactants into two categories, one is assumed to be un-mixed and chemically inert, while the other is assumed to be well-mixed and has infinitely fast chemistry. Wave speeds predicted by this model vary between the sound speed of the reactant cross-flow and the well-mixed one-dimensional CJ speed typically calculated for reactant mixtures. Results for C_2H_4/O_2 and CH_4/O_2 detonations show good qualitative agreement between

the experimental wave velocity, the schlieren or shadowgraph visualized fraction of the wave front that is closely coupled, and the analytical model heat release coupling factor.

The variety of experiments conducted in the LMDE and eLMDE facilities are already proven as valuable tools for use in numerical model development, validation, and investigation. Collaboration efforts include, but are not limited to, the work of Schwer et al (2017) from the Naval Research Laboratory, Lietz et al. (2018) from the Air Force Research Laboratory at Edwards Air Force Base, and Prakash et al. (2019) from the University of Michigan. Continued experiments in this novel configuration will no doubt remain a source of insight into the physical mechanisms of RDE.

7.3 Future Work

Several avenues of research logically follow from the efforts documented in this thesis. In general, these tasks either modify the eLMDE facility operation, alter the geometry of the facility, or vary the diagnostics used; the flexibility of the eLMDE facility allows for numerous permutations in further research.

Additional optical diagnostics can be implemented to improve the understanding of the RDE flowfield. Formaldehyde (CH_2O) planar laser induced fluorescence (PLIF), for example, is capable of obtaining a snapshot of the concentrations of CH_2O throughout the flowfield that can be used as a marker of heat release. Similarly, Raman spectroscopy can be used to isolate the concentrations of various reactants within the partially-mixed reactant cross-flow by measuring the stokes and/or the anti-stokes emission spectra of the gases. Together these two measurement techniques would provide a wealth of information on the distribution of reactants and heat release responsible for the detonation structures that have already been observed.

Implementation of either a laser line or sheet is relatively trivial for the eLMDE facility; the primary challenge with such diagnostics is ensuring precise optical alignment and synchronizing the laser with camera system.

Adjusting the eLMDE hardware to permit multiple pre-detonators allows for several avenues of advance. Positioning both pre-detonators at one end of the facility may allow for two consecutive detonation transits with only a short period between them; the current singular pre-detonator requires 110 ms to refresh, and shorter timescales of reactant cross-flow growth either involve transient gas pressurization or a combustion instability to regularly deflagrate the inflow. Placing the pre-detonators at opposite ends of the facility would instead allow for study of the counter-propagating mode observed in RDE experiments. In this case understanding both the feed system acoustic response and the reignition process of the detonation wave in the moments following the wave-wave interaction is of principal interest.

Alternatively, the eLMDE could be equipped with a varying area test section, such as one with a geometric throat installed at the exit plane. In this configuration the nozzling of the outflow could be varied to examine the role of the reflected oblique shock on the reactant refresh process. The acoustic response of the propellant feed systems could also be tailored by changing the insert that is currently installed within this piece of hardware.

Varying the injector and feed system geometries is another path of advance. The current configuration used is highly three-dimensional as a result of the circular injectors in the rectangular channel. Instead, slot-injectors could be machined such that the reactant inflow is as two-dimensional as possible, making the results easier to use

is numerical study validations. Alternatively, the feed system could be modified to support fully pre-mixed reactants; in this configuration the concern over reactant mixing within the cross-flow is entirely eliminated.

Finally, of inevitable interest to the RDE community is the study of detonations driven by a liquid propellant. The nature of propellant breakup through the detonation wave and how the droplet burns and couples to the incident wave front is of great interest. A variety of atomization techniques could be readily examined to ascertain their efficiency in such an unsteady environment.

Although many of these suggestions would make for interesting studies on their own, the incorporation of a numerical solver in parallel to these experiments would be a tremendous benefit. A side-by-side experimental and computational approach would aide in improving the understanding of RDE; where the numerical methods reveal both temporally and spatially resolved details of the flowfield, the experimental results will continue to be used as a valuable tool in grounding the numeric to the physically observed phenomena, as well as in the continued generation of novel data pertaining to the fundamental study of detonation structure in rotating detonation engine.

Appendix A: Experimental Facility Operation

A.1 Cross-Flow Initialization and Control

Investigation of the fundamental structure of detonation propagating into a reactant cross-flow required precise and repeatable control in the creation of a detonable reactant layer. The approach in this document was to control the timing of gas injection through arrays of direct acting solenoid valves (Parker-71215SN2EF00) controlled with a National Instruments CompactRIO controller (cRIO-9024). This

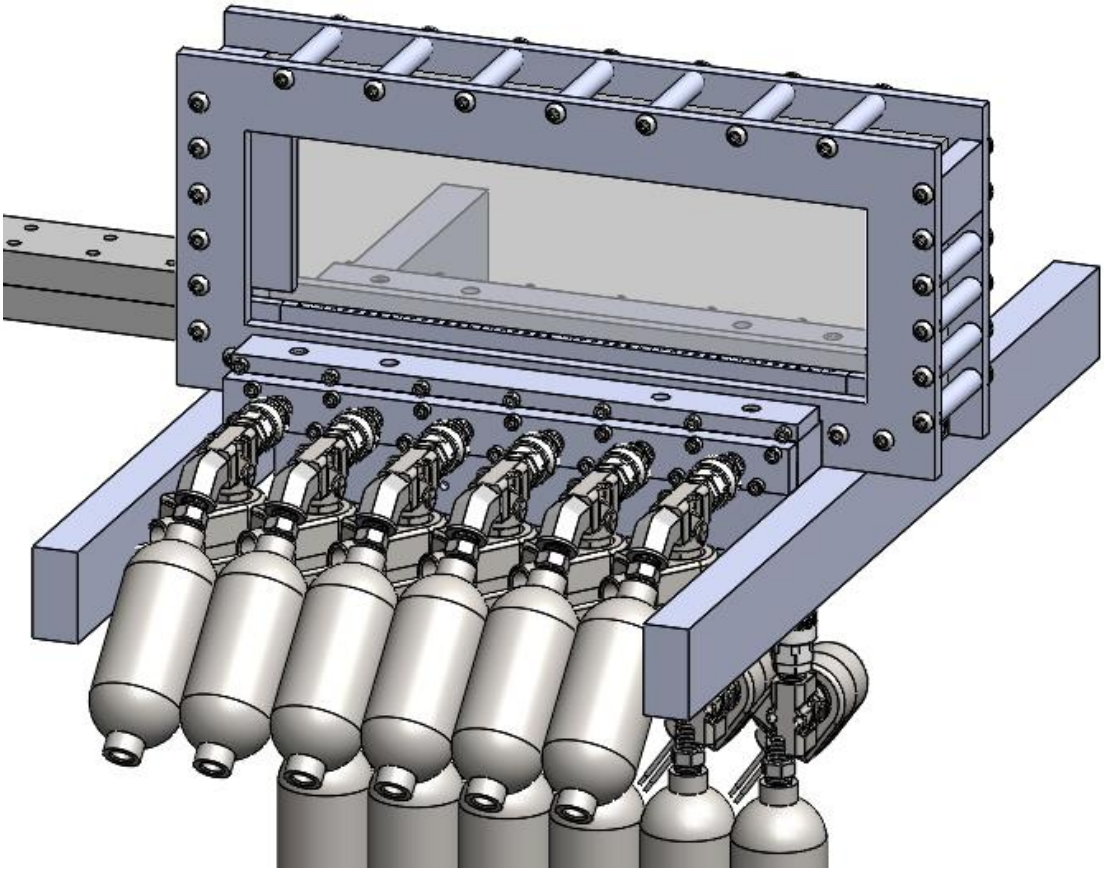

Figure A.1: Trimetric view of eLMDE CAD assembly. Fuel and oxidizer are supplied to the side and bottom of the recessed premixing tube, respectively. Transition piece for pre-detonator tube included (left).

combination allowed for independent and controlled timing of the injection of fuel and oxidizer species for numerous testing campaigns.

A trimetric view of the eLMDE facility with installed solenoid valves and upstream gas reservoirs is shown in Fig. A.1; detonation propagation occurs from left to right in this figure. The cross-section of the eLMDE facility is shown in Fig. A.2. Regions A and B are separated by the pre-detonator exit into the eLMDE channel, regions C and D are separated by control solenoids, regions D and E by geometric throats at the exit of the manifold into the recessed injectors, and region A and E by the exit of the recessed injectors into the reactangular channel. Note that only the oxidizer feed manifold is visualized in this cross-section; the fuel feed manifold is identical in geometry but occurs out of plane, as per Fig. A.1.

The timescale between subsequent wave transits in RDE geometries is on the order of 10-100's of microseconds, and is dependent on annulus diameter, reactant composition, number of waves, and manifold backpressure. The pre-detonator used in the eLMDE configuration was a PDE operating at approximately 9-Hz, prohibitively

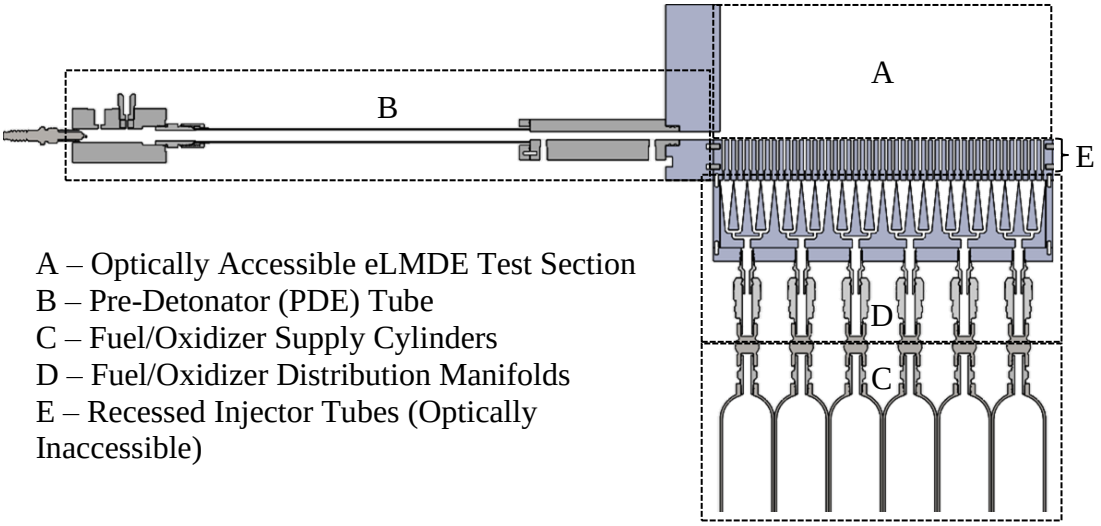

Figure A.2: Cross-sectional view of eLMDE facility. Oxidizer supply for reactant cross-flow (regions C and D) are shown; equivalent fuel supply geometry occurs out of plane and intersects at base of recessed injector tubes (region E).

slow for simulating steady-state RDE timescales. As a result facility operation focused on the generation of the initial reactant layer resulting from the transient pressurization of the reactant feed manifolds. Due to the low backpressure during this process, reactant injection timescales were on the order of 1-10's of milliseconds.

Ensuring that the fuel and oxidizer feed manifolds were not diluted by contaminants prior to the transient pressurization required the use of a purge cycle. In Fig. A.2, all regions except for region C were initially filled with air. Immediately prior to testing the solenoids for the fuel and oxidizer feed manifolds were opened, purging air from regions A, D, and E and replacing it with the respectve fuel or oxidizer for that feed manifold. Upon closing these solenoids the pre-detonator purge, typically nitrogen, filled regions A and B with an inert gas, removing the detonable gas from the eLMDE test section. The pre-detonator, region B, was then filled with a detonable reactant mixture. Solenoids between regions C and D were then opened a second time, generating a transient reactant cross-flow layer in the eLMDE test section. Finally, the pre-detonator was ignited using an automotive spark plug, and the resulting detonation transit through the reactant cross-flow was visualized.

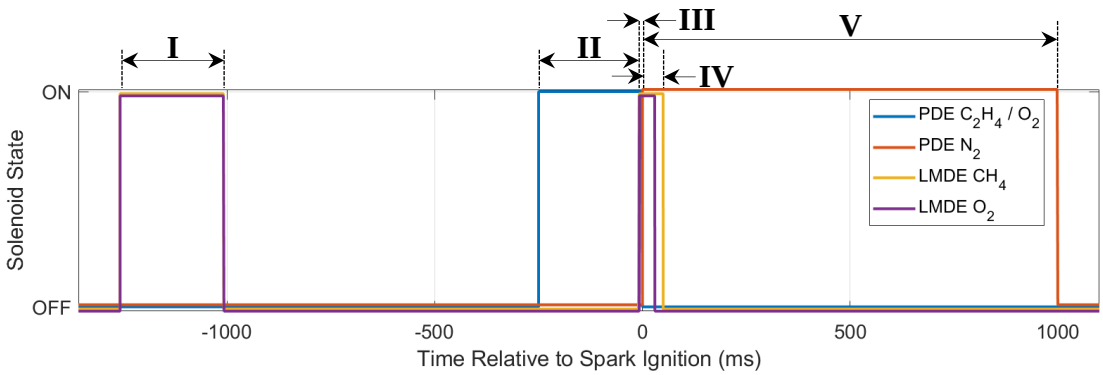

Figure A.3: Typical solenoid on/off sequence for CH_4/O_2 detonation experiments. Relevant timing components marked; spark ignition of PDE occurs at t = 0.

The time sequence of solenoid on/off states are plotted in Fig. A.3, with significant events marked. These regions correspond to: (I) the initial purge of the fuel and oxidizer feed manifolds; (II) the filling of the pre-detonator with a detonable gas; (III) the second pressurization of the fuel and oxidizer feed manifolds, yielding the reactant cross-flow; (IV) additional fuel and oxidizer feed manifold pressurization time, to ensure continuous inflow following detonation transit; and (V) the pre-detonator purge phase following the detonation transit.

Of particular note is the short duration of the second pressurization of the fuel and oxidizer feed manifolds (III). While the totality of the pre-test purge sequence is approimately one second in length, this phase is of the order of 1-10's of milliseconds. Additionally, the additional fuel and oxidizer feed manifold times (IV) are not equal; this difference in timing ensures that a largely fuel or oxidizer mixture that is not detonable remains within recessed premixing tubes at the end of the test sequence. In general the gas with the lower molecular weight is chosen to remain on the longest to ensure it will not pool within these tubes.

The necessary sequence of solenoid on and off commands were accomplished with a National Instruments CompactRIO device; programming of the FPGA made use of the timed loop structure such that the state of the solenoids were updated at a rate of 40MHz. Microsecond-level accuracy of output control was possible for updating the state of the solenoids for the reactant feed manifolds, as well as pre-detonator gases, spark timing, camera triggering, and other signals. To ensure maximum program flexibility, most of the triggering signals were variable in nature; purge duration, time between the end of purge and secondary pressurization, and other on/off states, could

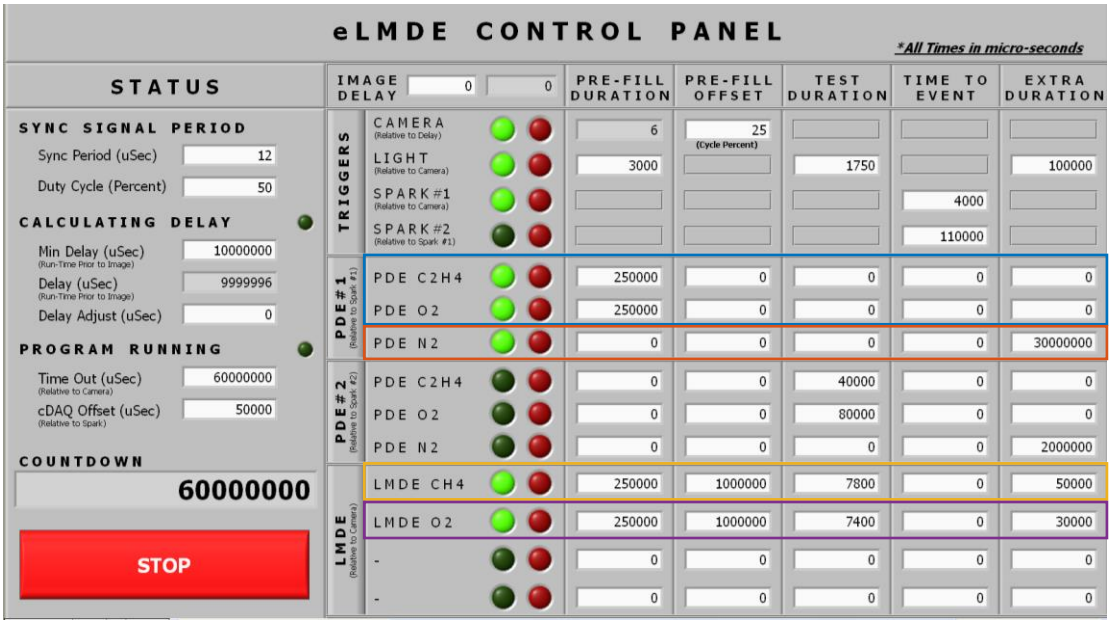

Figure A.4: Computer interface of LabVIEW FPGA Module for National Instruments CompactRIO controller for the eLMDE facility. Solenoid on/off sequence for outlined channels depicted in Fig. A.3.

be easily modified to tune the reactant cross-flow characteristics and composition of the eLMDE test section between tests. An example of the LabVIEW controller for the eLMDE facility is shown in Fig. A.4. Note that the outlined timings in Fig. A.4 correspond to those illustrated in Fig. A.3.

In general the five control parameters for each gas channel correspond to durations of an “on-off-on-off-on” sequence for the corresponding solenoid(s). Individual device channels can be toggled on and off to quickly examine different features of establishing the eLMDE flowfield. Additional program features include generating a square Low-Voltage Transistor-Transistor Logic (LVTTL) signal used to synchronizing camera, laser, and solenoid signals, triggering a light source, triggering a camera, triggering a LabVIEW CompactDAQ system, and firing a second pre-detonator.

A.2 Standard Operating Procedure (SOP)

(Extended) Linear Detonation Rig Experiment

Advanced Propulsion Research Laboratory, University of Maryland

I. Safety Precautions:

1. This experiment involves volatile flammable gases at detonable mixture ratios, which can lead to an explosive rise in the local pressure (i.e., 13-55 times). Everyone participating in the experiment must be aware of the danger of detonation testing. Review both the test procedure and the emergency shutdown procedure.
2. When detonation experiment is in progress, all participants are required to wear hearing protection and everyone must be outside of the test bay, a safe distance away from the detonation test rig.
3. Prior to testing, all valves and connections should be checked for proper functioning and possible leaks. Inspect the supply line for each gas, carefully noting various components involved.

II. Test Procedure:

1. Carefully inspect all test equipment and instrumentations. Make sure the test control and data acquisition programs are ready and functioning properly. Verify the accuracy of pre-test calculation, with special attention to the length of the total test duration and the amount of detonable reactants involved.
2. Set the pressure values in the gas supply lines for proper flow rates, including oxidizer, fuel, and purge gases.

3. Make sure everyone is outside of the test bay and/or safely away. Start the test programs, which control the sequence of solenoid valves openings and closings as well as the timing of the ignition, the automatic stop and the flow of purge gas.
4. After each test ends, turn off the solenoid valves for fuel(s) and oxidizer(s) from the switch box. Close immediately the manual valves for the fuels and the oxidizer lines.
5. Each detonation test should end when the pre-programmed sequence is completed from the test control software. If the test continues after it was supposed to stop, employ the EMERGENCY SHUTDOWN PROCEDURE described below. Also, in case of uncontrolled reaction or unplanned disruptive event, employ the EMERGENCY SHUTDOWN PROCEDURE.
6. At the completion of the tests, purge all gas lines, remove the spark plug wire, and close all the supply gas bottles.

EMERGENCY SHUTDOWN PROCEDURE (PANIC STOP):

Turn off all fuel solenoid valves and close all fuel manual valves, in no particular order. Also, turn off or close all oxidizer valves as well.

IN CASE OF EMERGENCY: Fire extinguishers are posted around the laboratory space. The easiest way to eliminate combustor-related fire is to shut off all fuel supply. If any undesirable flow conditions are encountered that needs to be abandoned immediately, turn off or close all fuel solenoid valves and fuel manual valves. Call for help.

Appendix B: Engineering Drawings of LMDE

This appendix contains the engineering drawings for the most important components of the Linear Model Detonation Engine (LMDE) used for the hydrogen and ethylene detonation experiments. The dimensions in all of these drawings are provided in inches and the scale varies depending on the size of the part of assembly to highlight different design features.

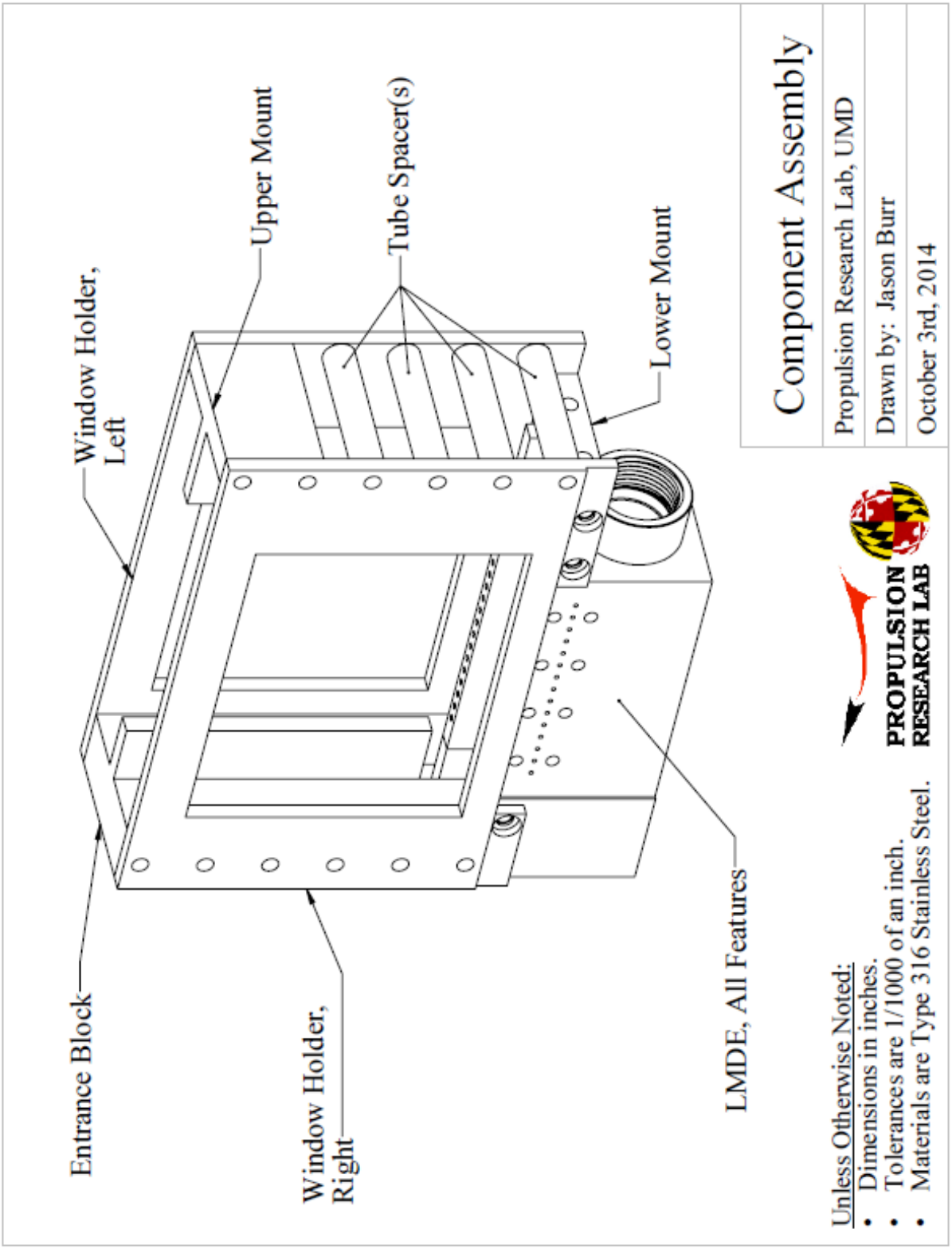
Window Holder, Left
Upper Mount
Tube Spacer(s)
Lower Mount
Entrance Block
Window Holder, Right
LMDE, All Features
Component Assembly
Propulsion Research Lab, UMD
Drawn by: Jason Burr
October 3rd, 2014
PROPULSION RESEARCH LAB
Unless Otherwise Noted:
• Dimensions in inches.
• Tolerances are 1/1000 of an inch.
• Materials are Type 316 Stainless Steel.

Air Mount Block
(Note: Threaded holes on face
opposite the one the arrow points to)
Air Manifold
Welds on all four
joining edges. Welds
on the top should be
"flat" to allow for a
gasket seal.
1 Inch Half-Coupler
Welds along outer diameter. Half-Coupler
should align with the hollowed-out
cylinder from the Air Manifold. Welds
needs to be airtight (up to ~130psi).
Unless Otherwise Noted:
• All dimensions are in inches.
• All tolerances are 5/1000 of an inch.
• All materials are Type 316 Stainless Steel.
Air Manifold Welds
Propulsion Research Lab, UMD
Drawn By: Jason Burr
December 9th, 2013

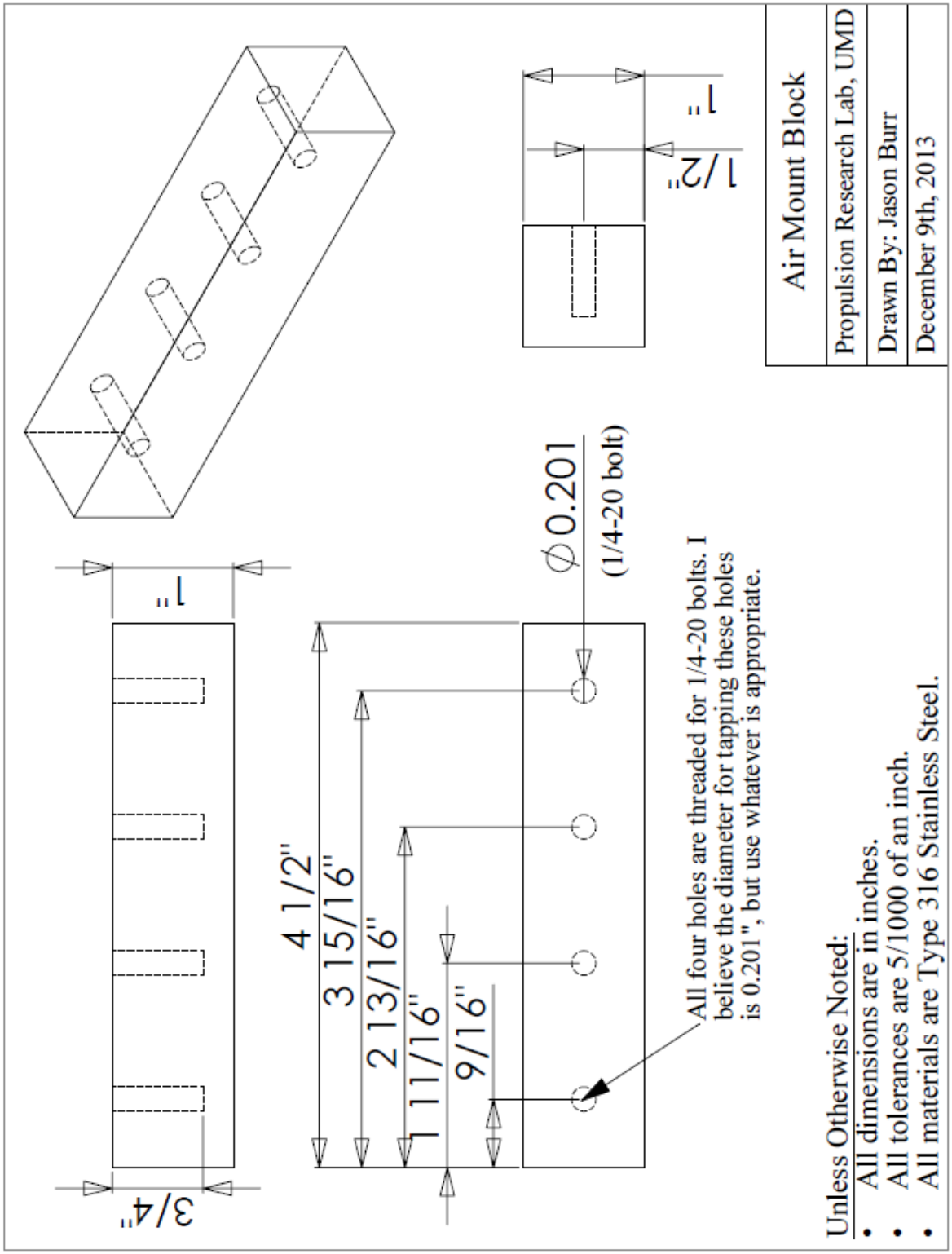
Air Mount Block
Propulsion Research Lab, UMD
Drawn By: Jason Burr
December 9th, 2013
Unless Otherwise Noted:
• All dimensions are in inches.
• All tolerances are 5/1000 of an inch.
• All materials are Type 316 Stainless Steel.
All four holes are threaded for 1/4-20 bolts. I believe the diameter for tapping these holes is 0.201", but use whatever is appropriate.
⌀0.201
(1/4-20 bolt)
4 1/2"
3 15/16"
2 13/16"
1 11/16"
9/16"
1"
3/4"
1 1/2"
1"

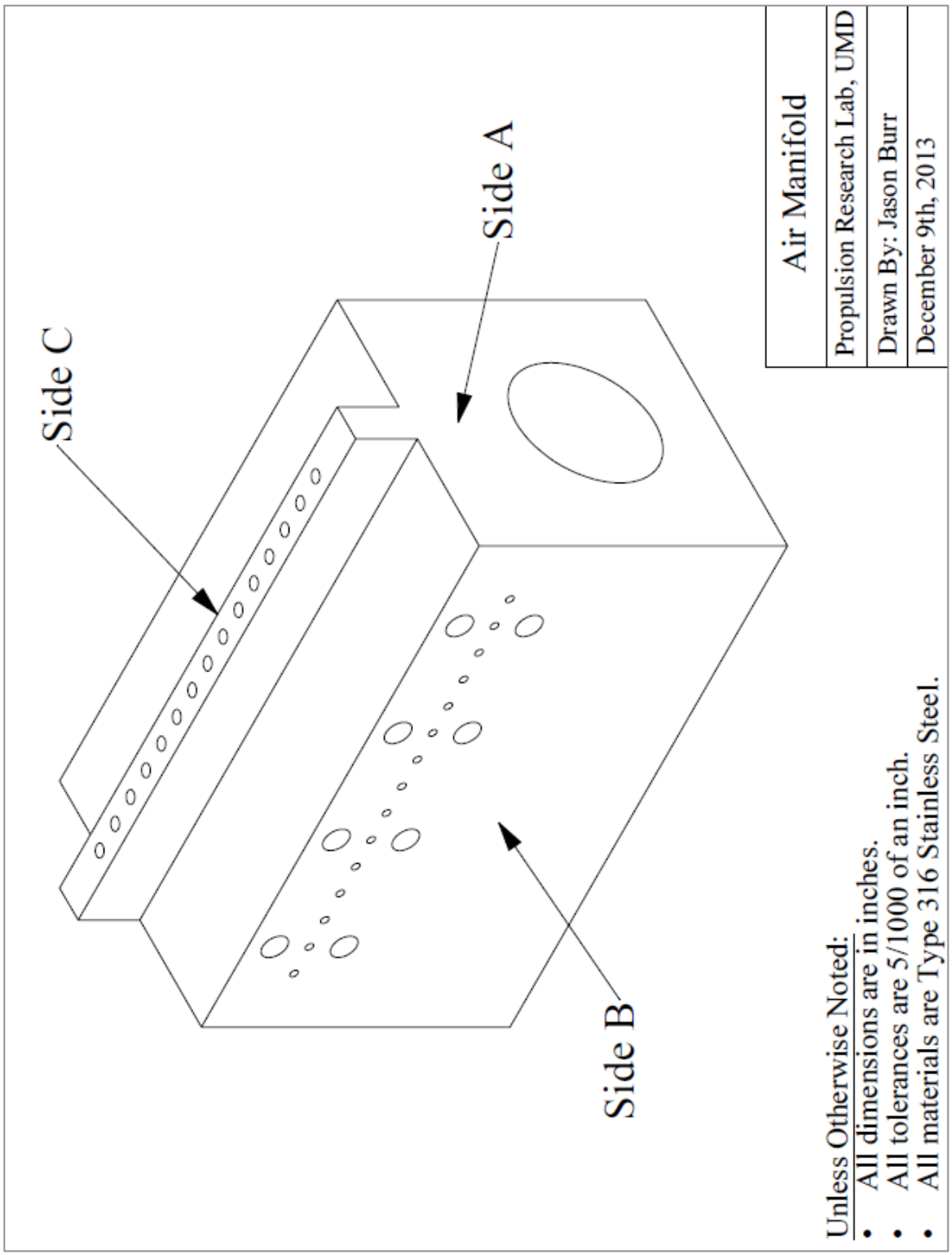
Side C
Side A
Side B
Air Manifold
Propulsion Research Lab, UMD
Drawn By: Jason Burr
December 9th, 2013
Unless Otherwise Noted:
• All dimensions are in inches.
• All tolerances are 5/1000 of an inch.
• All materials are Type 316 Stainless Steel.

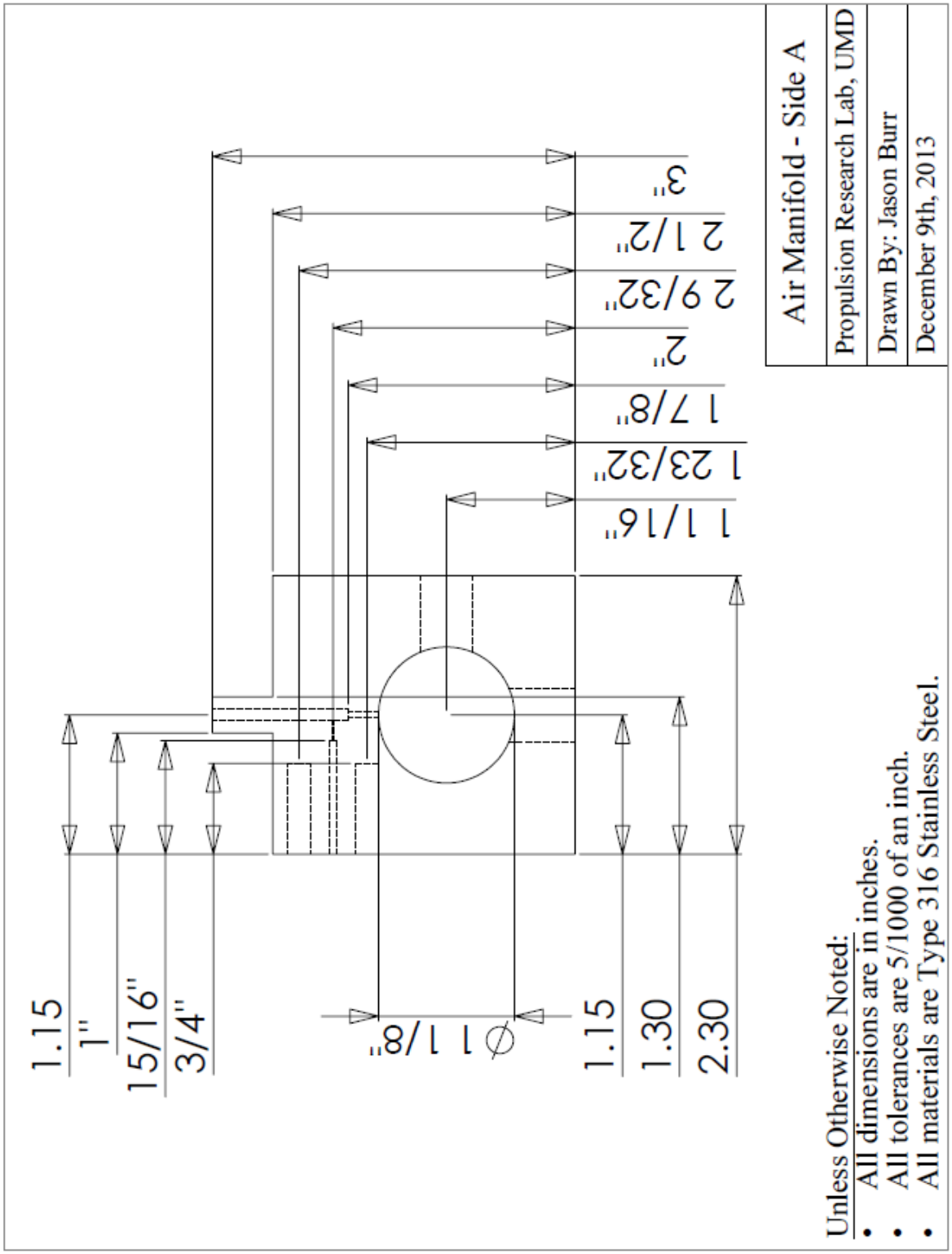
Air Manifold - Side A
Propulsion Research Lab, UMD
Drawn By: Jason Burr
December 9th, 2013
Unless Otherwise Noted:
• All dimensions are in inches.
• All tolerances are 5/1000 of an inch.
• All materials are Type 316 Stainless Steel.
3"
2 1/2"
2 9/32"
2"
1 7/8"
1 23/32"
1 1/16"
∅ 1 1/8"
1.15
1"
15/16"
3/4"
1.15
1.30
2.30

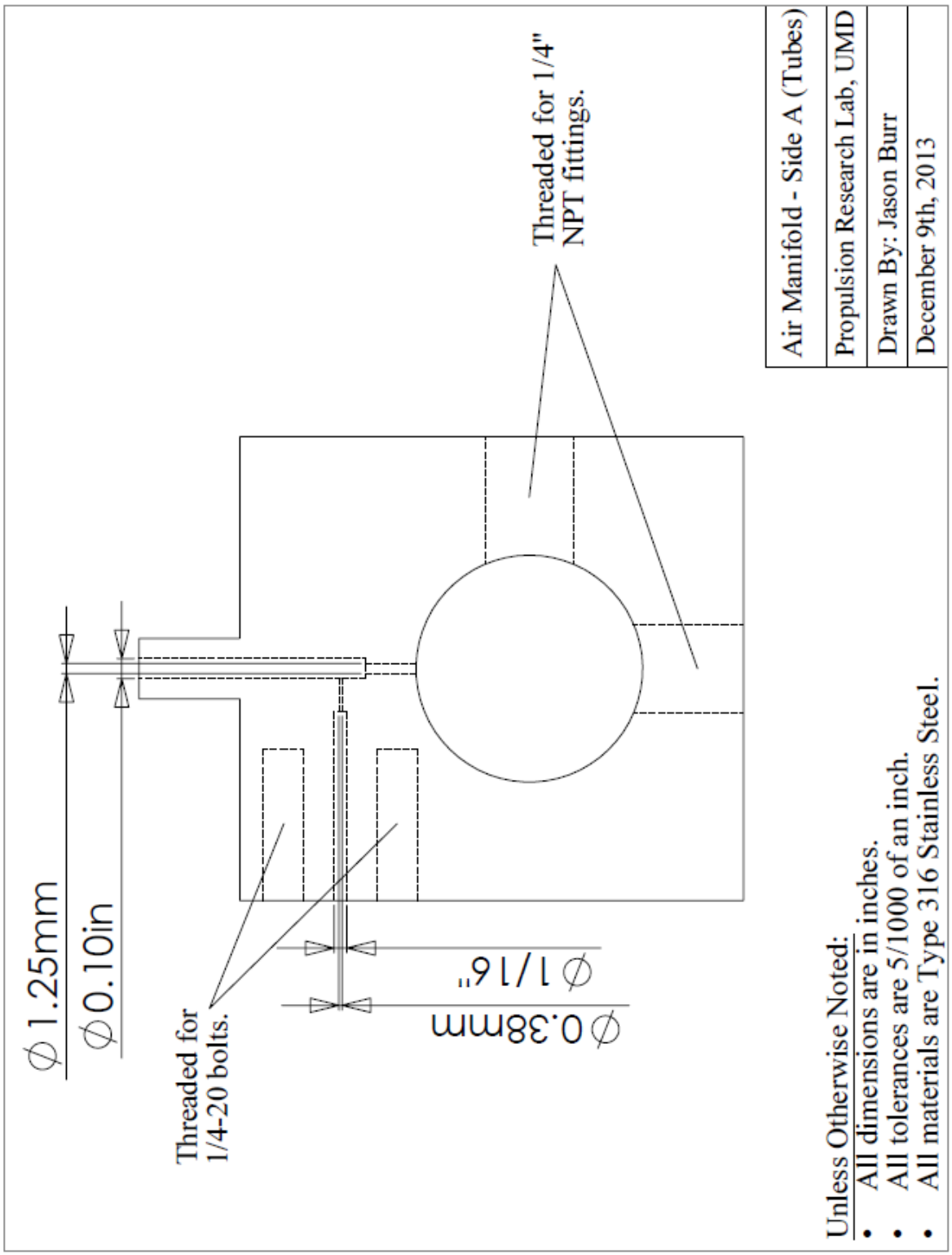
Air Manifold - Side A (Tubes)
Propulsion Research Lab, UMD
Drawn By: Jason Burr
December 9th, 2013
Threaded for 1/4"
NPT fittings.
Threaded for
1/4-20 bolts.
∅1.25mm
∅0.10in
∅0.38mm
∅1/16"
Unless Otherwise Noted:
• All dimensions are in inches.
• All tolerances are 5/1000 of an inch.
• All materials are Type 316 Stainless Steel.

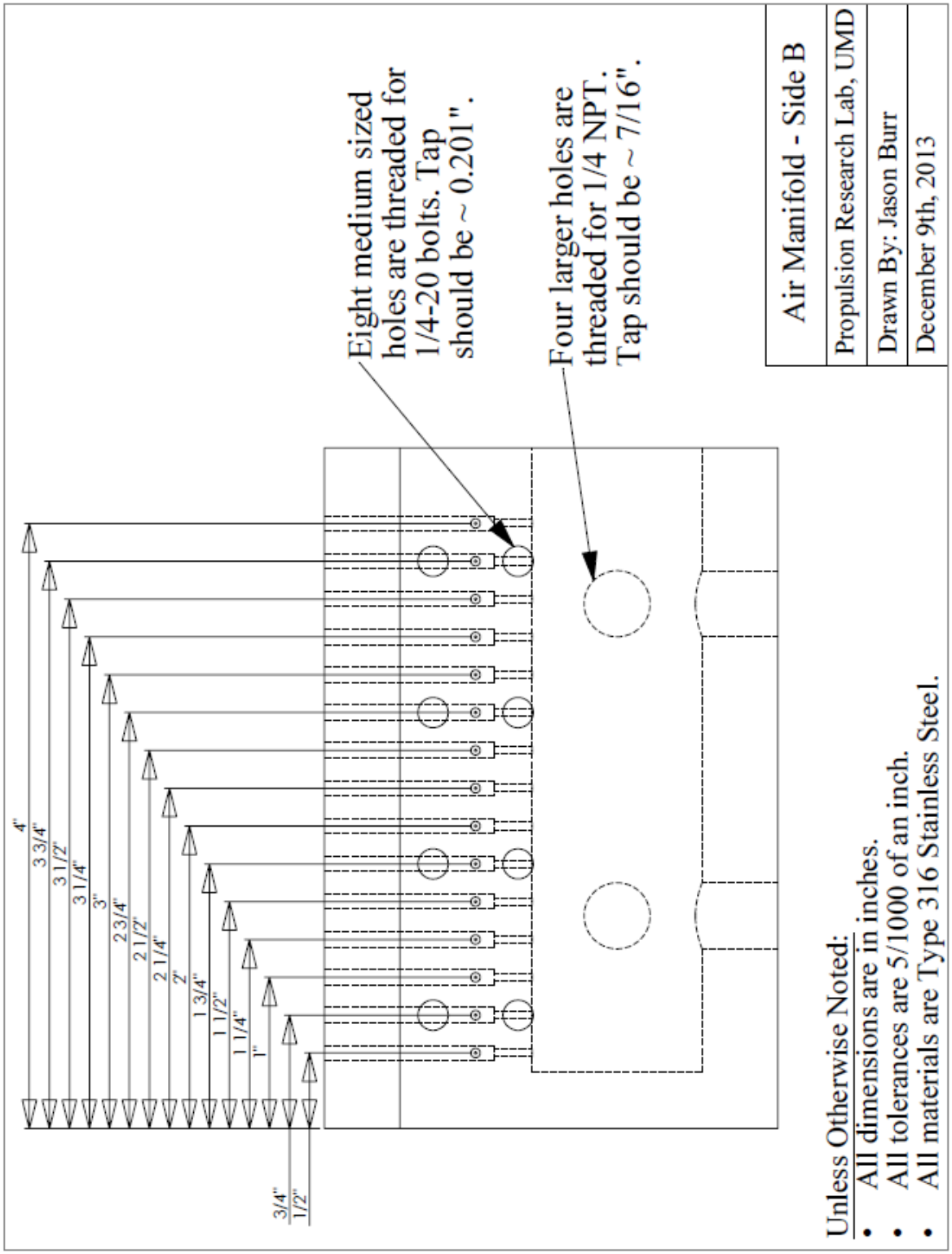
Air Manifold - Side B
Propulsion Research Lab, UMD
Drawn By: Jason Burr
December 9th, 2013
Eight medium sized holes are threaded for 1/4-20 bolts. Tap should be ~ 0.201".
Four larger holes are threaded for 1/4 NPT. Tap should be ~ 7/16".
4"
3 3/4"
3 1/2"
3 1/4"
3"
2 3/4"
2 1/2"
2 1/4"
2"
1 3/4"
1 1/2"
1 1/4"
1"
3/4"
1/2"
Unless Otherwise Noted:
All dimensions are in inches.
All tolerances are 5/1000 of an inch.
All materials are Type 316 Stainless Steel.

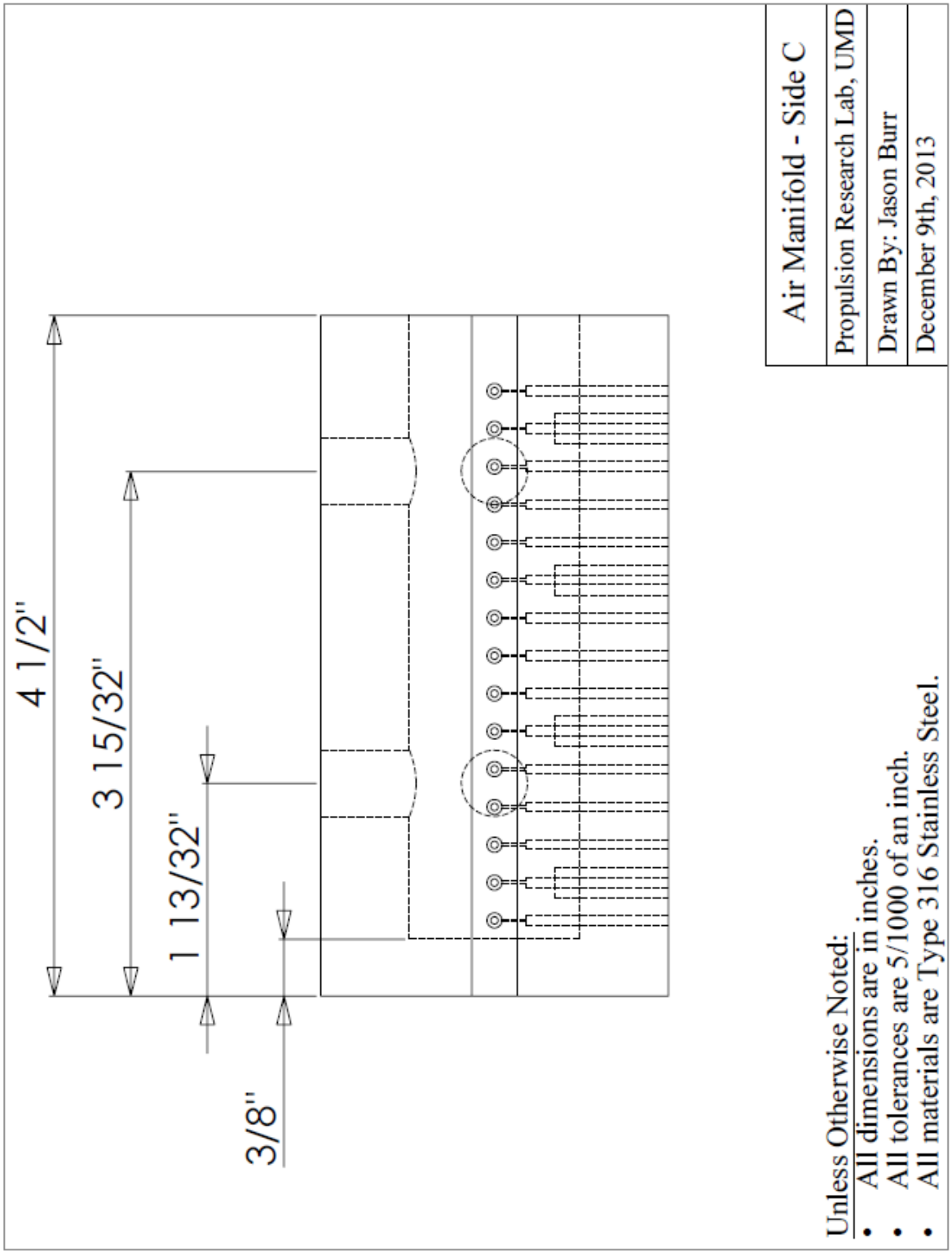
4 1/2"
3 15/32"
1 13/32"
3/8"
Air Manifold - Side C
Propulsion Research Lab, UMD
Drawn By: Jason Burr
December 9th, 2013
Unless Otherwise Noted:
• All dimensions are in inches.
• All tolerances are 5/1000 of an inch.
• All materials are Type 316 Stainless Steel.

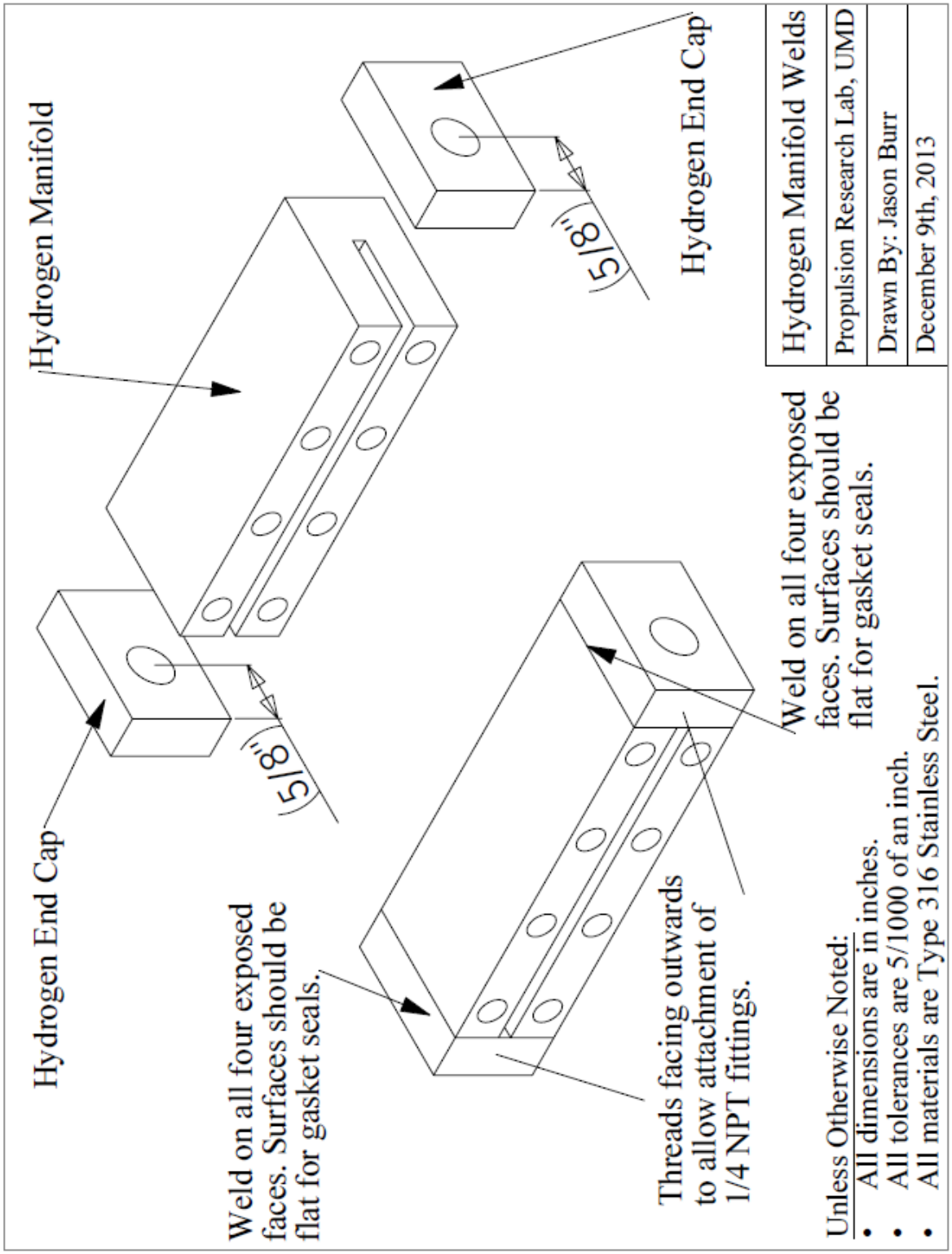
Hydrogen Manifold
Hydrogen End Cap
5/8"
Hydrogen End Cap
5/8"
Weld on all four exposed faces. Surfaces should be flat for gasket seals.
Threads facing outwards to allow attachment of 1/4 NPT fittings.
Weld on all four exposed faces. Surfaces should be flat for gasket seals.
Hydrogen Manifold Welds
Propulsion Research Lab, UMD
Drawn By: Jason Burr
December 9th, 2013
Unless Otherwise Noted:
• All dimensions are in inches.
• All tolerances are 5/1000 of an inch.
• All materials are Type 316 Stainless Steel.

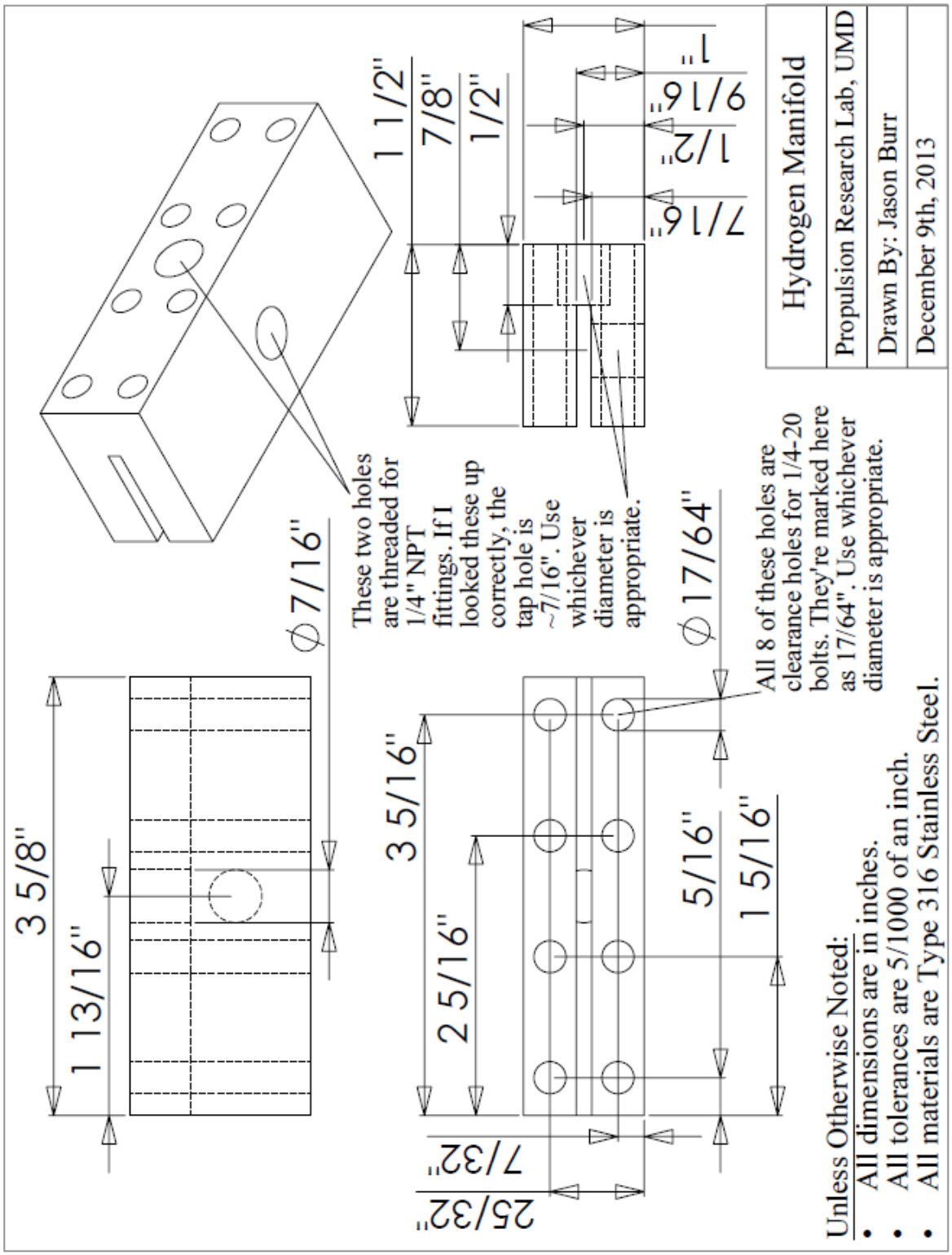
Hydrogen Manifold
Propulsion Research Lab, UMD
Drawn By: Jason Burr
December 9th, 2013
Unless Otherwise Noted:
All dimensions are in inches.
All tolerances are 5/1000 of an inch.
All materials are Type 316 Stainless Steel.
All 8 of these holes are clearance holes for 1/4-20 bolts. They're marked here as 17/64". Use whichever diameter is appropriate.
These two holes are threaded for 1/4" NPT fittings. If I looked these up correctly, the tap hole is ~7/16". Use whichever diameter is appropriate.
ϕ 7/16"
ϕ 17/64"
3 5/8"
1 13/16"
3 5/16"
2 5/16"
5/16"
1 5/16"
25/32"
7/32"
1 1/2"
7/8"
1/2"
7/16"
1/2"
9/16"
1"

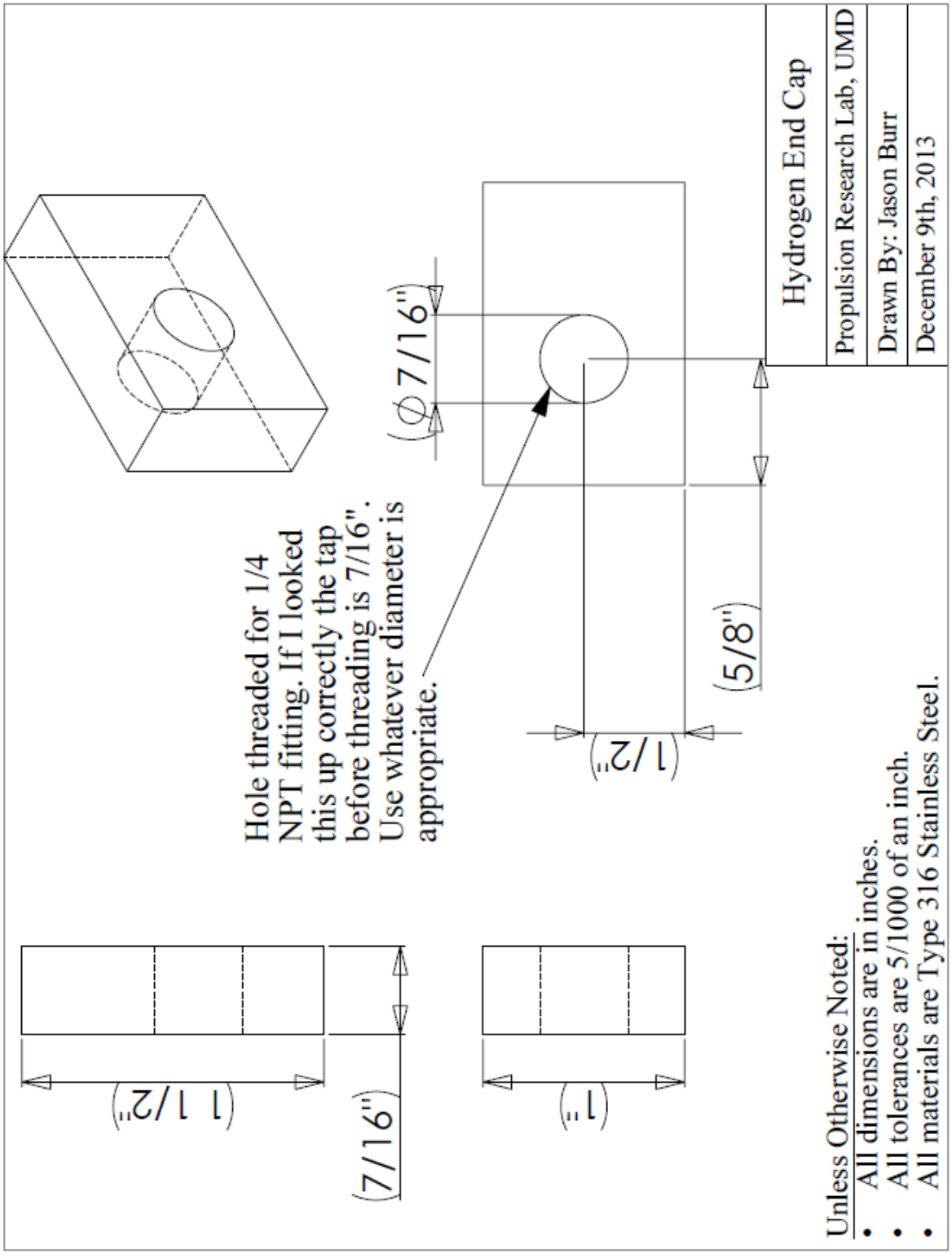
Hydrogen End Cap
Propulsion Research Lab, UMD
Drawn By: Jason Burr
December 9th, 2013
Unless Otherwise Noted:
• All dimensions are in inches.
• All tolerances are 5/1000 of an inch.
• All materials are Type 316 Stainless Steel.
Hole threaded for 1/4 NPT fitting. If I looked this up correctly the tap before threading is 7/16". Use whatever diameter is appropriate.
(Ø 7/16")
(1/2")
(5/8")
(1")
(1 1/2")
(7/16")

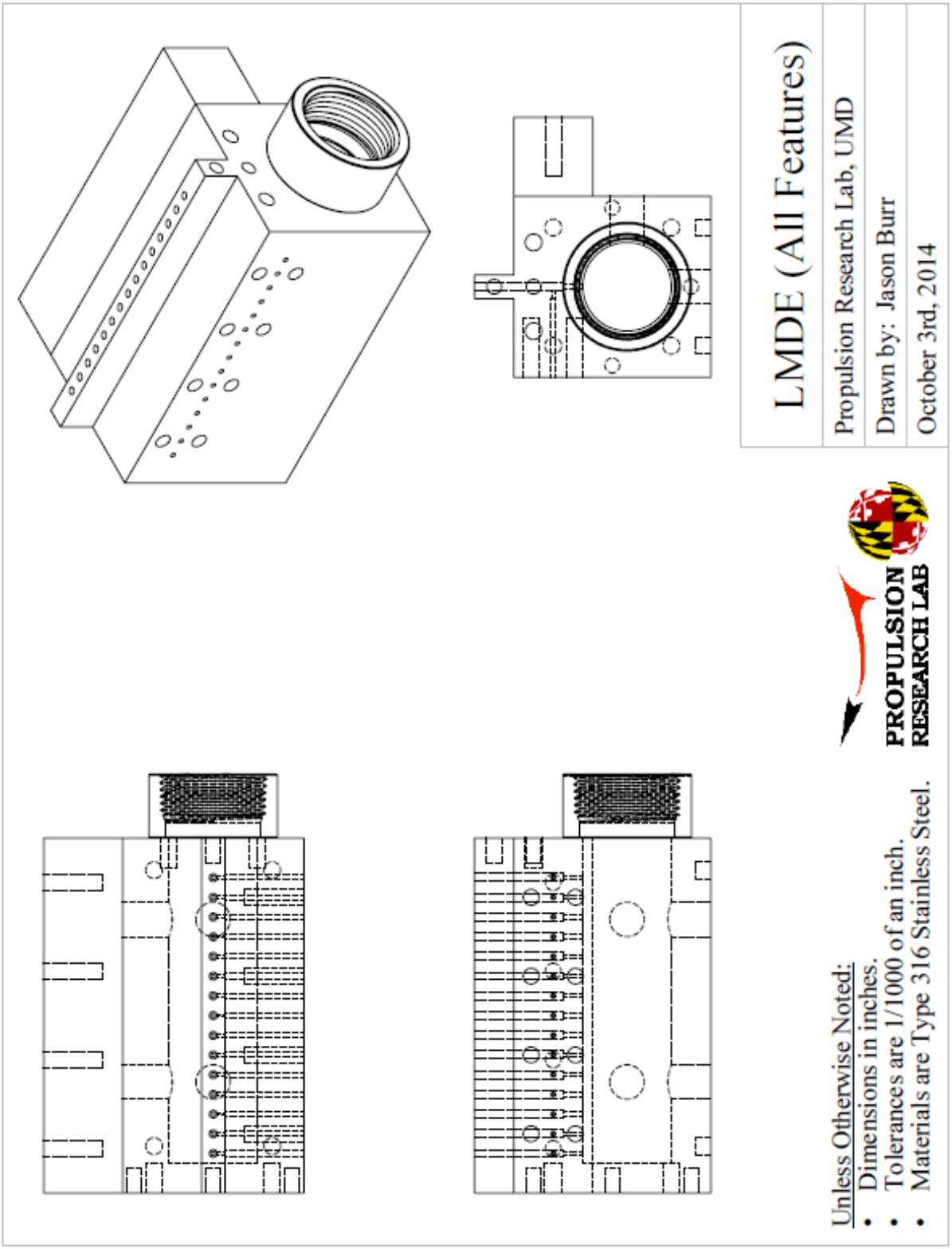
LMDE (All Features)
Propulsion Research Lab, UMD
Drawn by: Jason Burr
October 3rd, 2014
PROPULSION
RESEARCH LAB
Unless Otherwise Noted:
• Dimensions in inches.
• Tolerances are 1/1000 of an inch.
• Materials are Type 316 Stainless Steel.

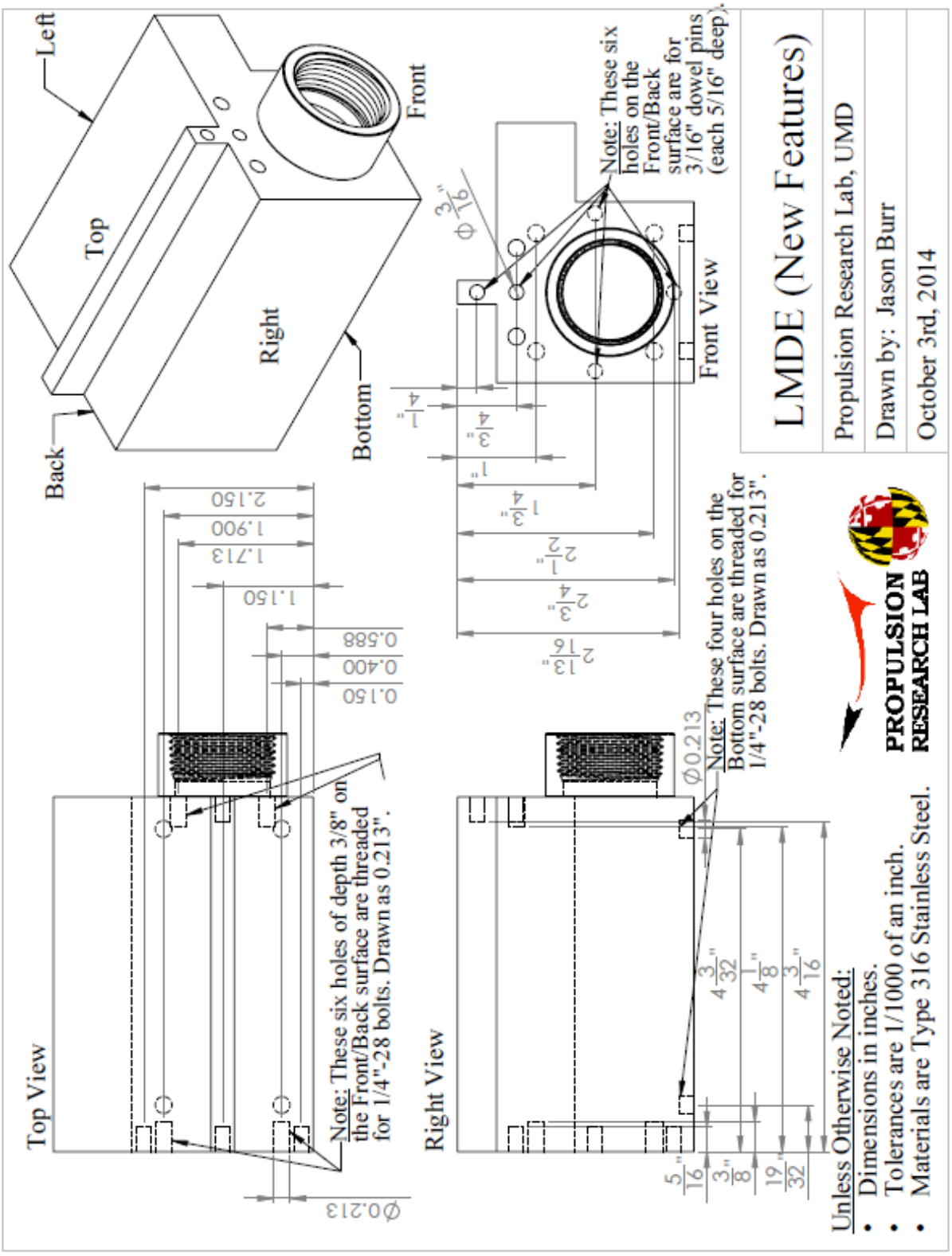
Left
Top
Front
Right
Back
Bottom
Front View
Note: These six holes on the Front/Back surface are for 3/16" dowel pins (each 5/16" deep).
Top View
Note: These six holes of depth 3/8" on the Front/Back surface are threaded for 1/4"-28 bolts. Drawn as 0.213".
Right View
Note: These four holes on the Bottom surface are threaded for 1/4"-28 bolts. Drawn as 0.213".
LMDE (New Features)
Propulsion Research Lab, UMD
Drawn by: Jason Burr
October 3rd, 2014
PROPULSION RESEARCH LAB
Unless Otherwise Noted:
• Dimensions in inches.
• Tolerances are 1/1000 of an inch.
• Materials are Type 316 Stainless Steel.

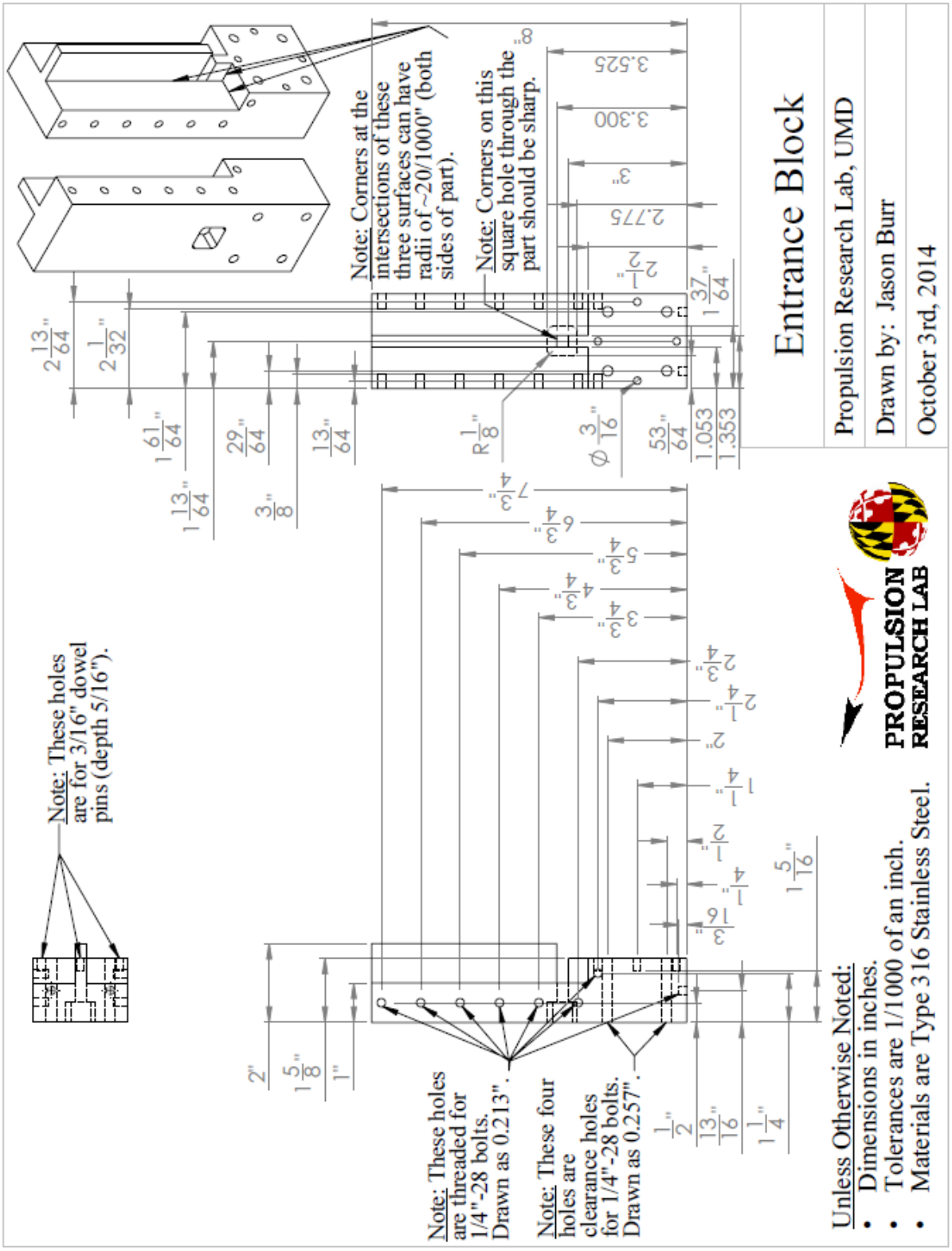
Entrance Block
Propulsion Research Lab, UMD
Drawn by: Jason Burr
October 3rd, 2014
PROPULSION RESEARCH LAB
Note: Corners at the intersections of these three surfaces can have radii of ~20/1000" (both sides of part).
Note: Corners on this square hole through the part should be sharp.
Note: These holes are for 3/16" dowel pins (depth 5/16").
Note: These holes are threaded for 1/4"-28 bolts. Drawn as 0.213".
Note: These four holes are clearance holes for 1/4"-28 bolts. Drawn as 0.257".
Unless Otherwise Noted:
• Dimensions in inches.
• Tolerances are 1/1000 of an inch.
• Materials are Type 316 Stainless Steel.

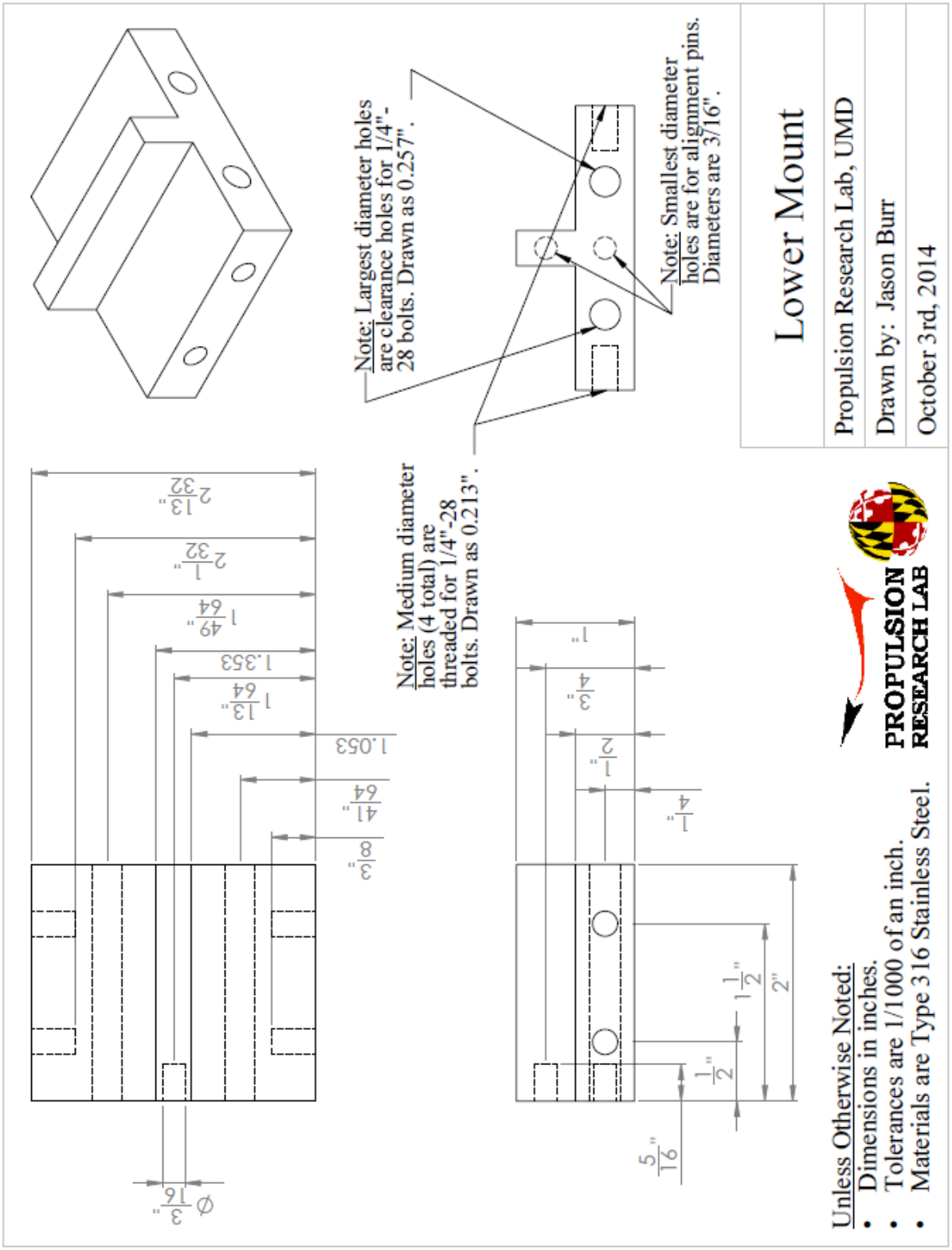
Lower Mount
Propulsion Research Lab, UMD
Drawn by: Jason Burr
October 3rd, 2014
PROPULSION RESEARCH LAB
Note: Largest diameter holes are clearance holes for 1/4"-28 bolts. Drawn as 0.257".
Note: Smallest diameter holes are for alignment pins. Diameters are 3/16".
Note: Medium diameter holes (4 total) are threaded for 1/4"-28 bolts. Drawn as 0.213".
Unless Otherwise Noted:
• Dimensions in inches.
• Tolerances are 1/1000 of an inch.
• Materials are Type 316 Stainless Steel.

Tube Spacer
Propulsion Research Lab, UMD
Drawn by: Jason Burr
October 3rd, 2014
PROPULSION
RESEARCH LAB
Unless Otherwise Noted:
• Dimensions in inches.
• Tolerances are 1/1000 of an inch.
• Materials are Type 316 Stainless Steel.
Note: Material for tube supplied (McMaster-Carr part #89495K485). Four spacers of given length are required.
Ø 1/2"
Ø 0.260
2 27/64"

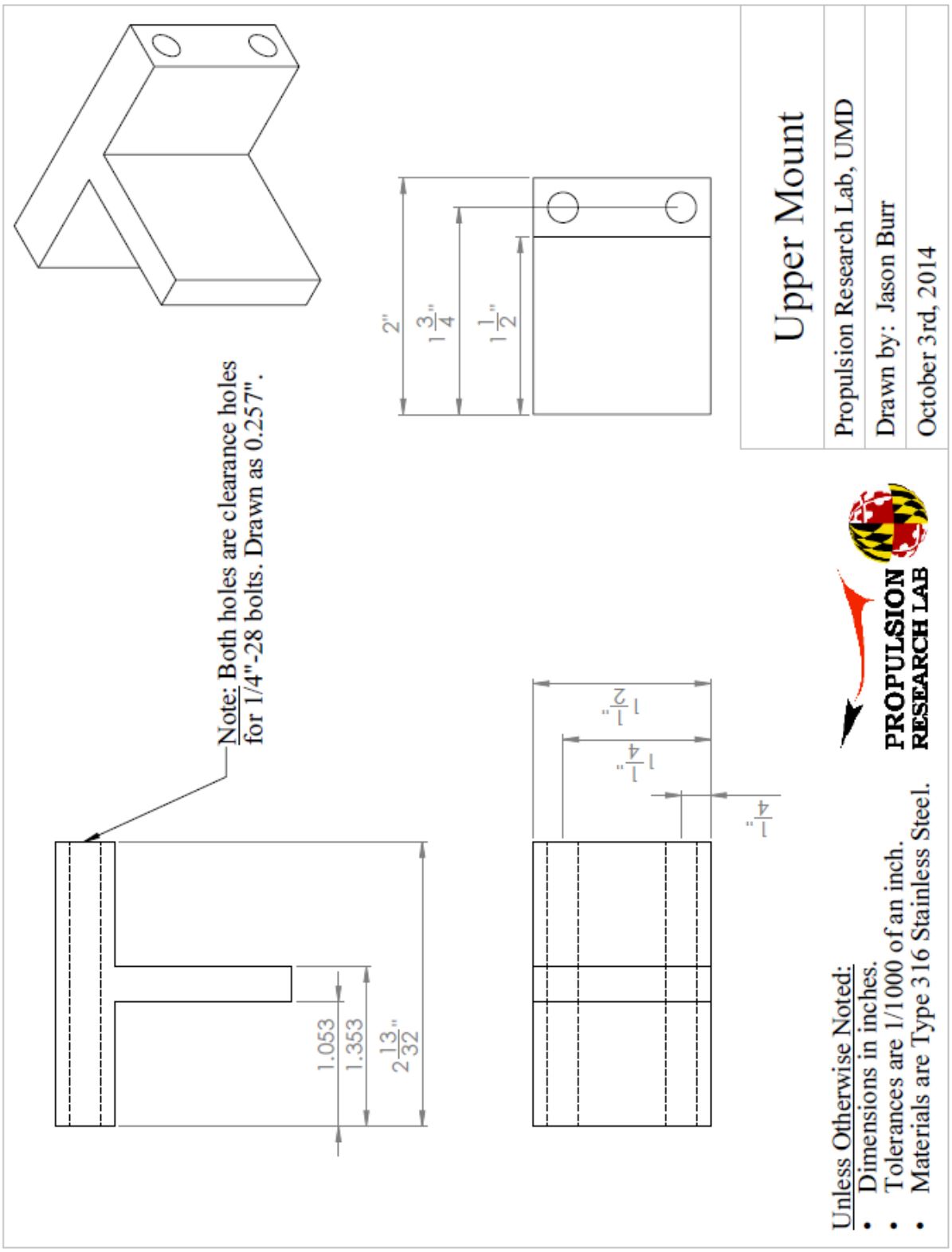
Upper Mount
Propulsion Research Lab, UMD
Drawn by: Jason Burr
October 3rd, 2014
PROPULSION RESEARCH LAB
Unless Otherwise Noted:
• Dimensions in inches.
• Tolerances are 1/1000 of an inch.
• Materials are Type 316 Stainless Steel.
Note: Both holes are clearance holes for 1/4"-28 bolts. Drawn as 0.257".
2"
1 3/4"
1 1/2"
1.053
1.353
2 13/32"
1 1/2"
1 1/4"
1/4"

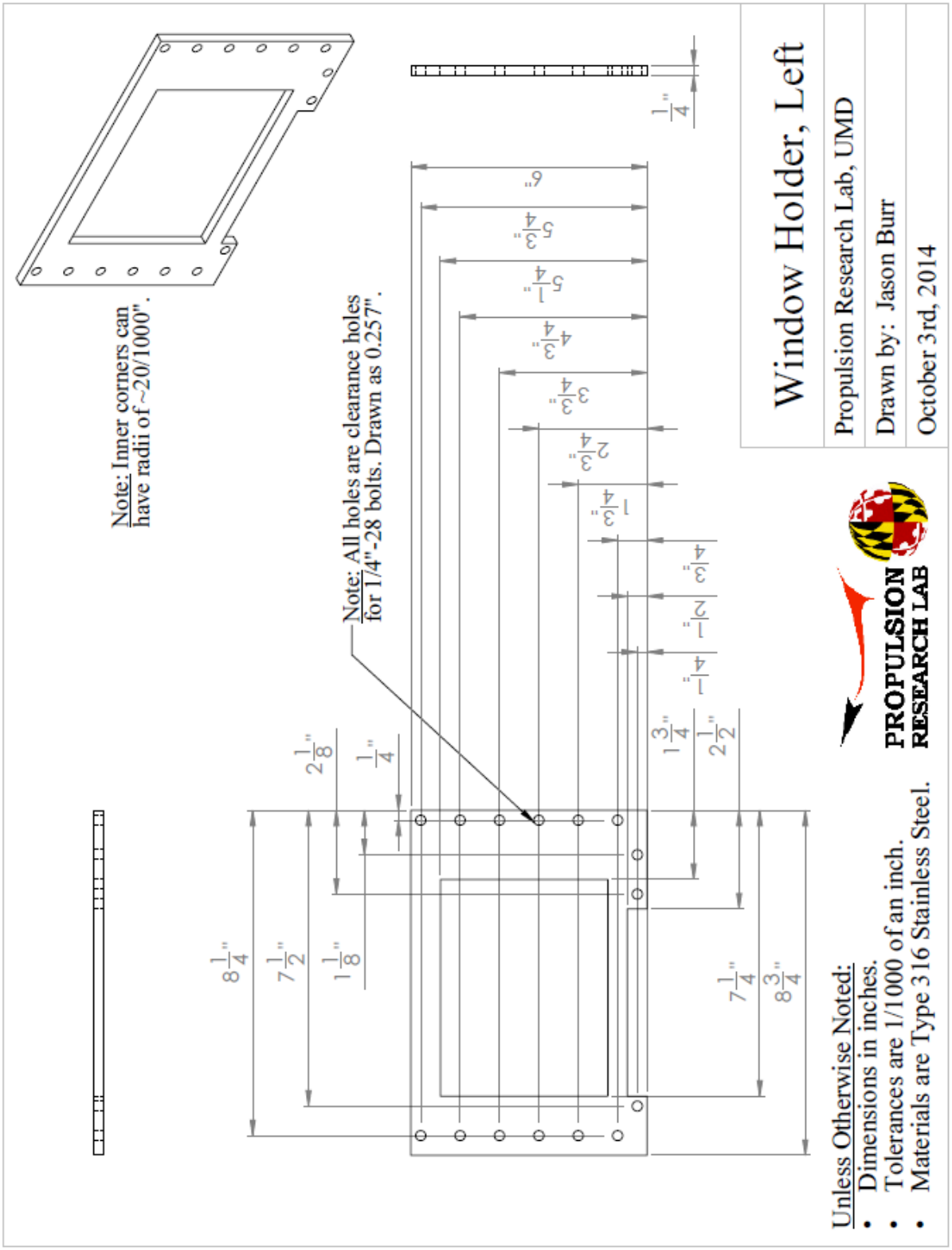
Window Holder, Left
Propulsion Research Lab, UMD
Drawn by: Jason Burr
October 3rd, 2014
PROPULSION RESEARCH LAB
Note: Inner corners can have radii of ~20/1000".
Note: All holes are clearance holes for 1/4"-28 bolts. Drawn as 0.257".
Unless Otherwise Noted:
• Dimensions in inches.
• Tolerances are 1/1000 of an inch.
• Materials are Type 316 Stainless Steel.

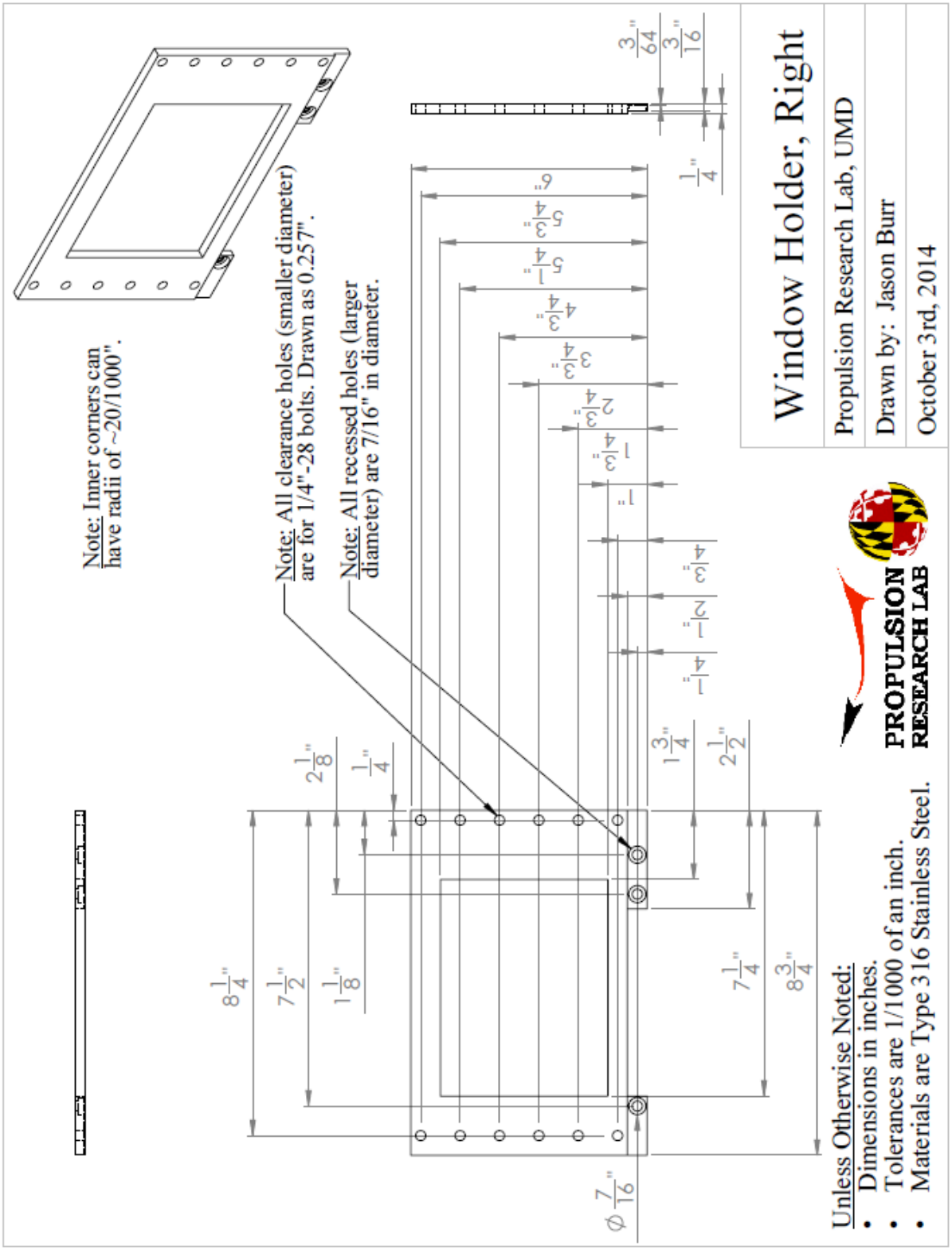
Window Holder, Right
Propulsion Research Lab, UMD
Drawn by: Jason Burr
October 3rd, 2014
PROPULSION RESEARCH LAB
Note: Inner corners can have radii of ~20/1000".
Note: All clearance holes (smaller diameter) are for 1/4"-28 bolts. Drawn as 0.257".
Note: All recessed holes (larger diameter) are 7/16" in diameter.
Unless Otherwise Noted:
• Dimensions in inches.
• Tolerances are 1/1000 of an inch.
• Materials are Type 316 Stainless Steel.

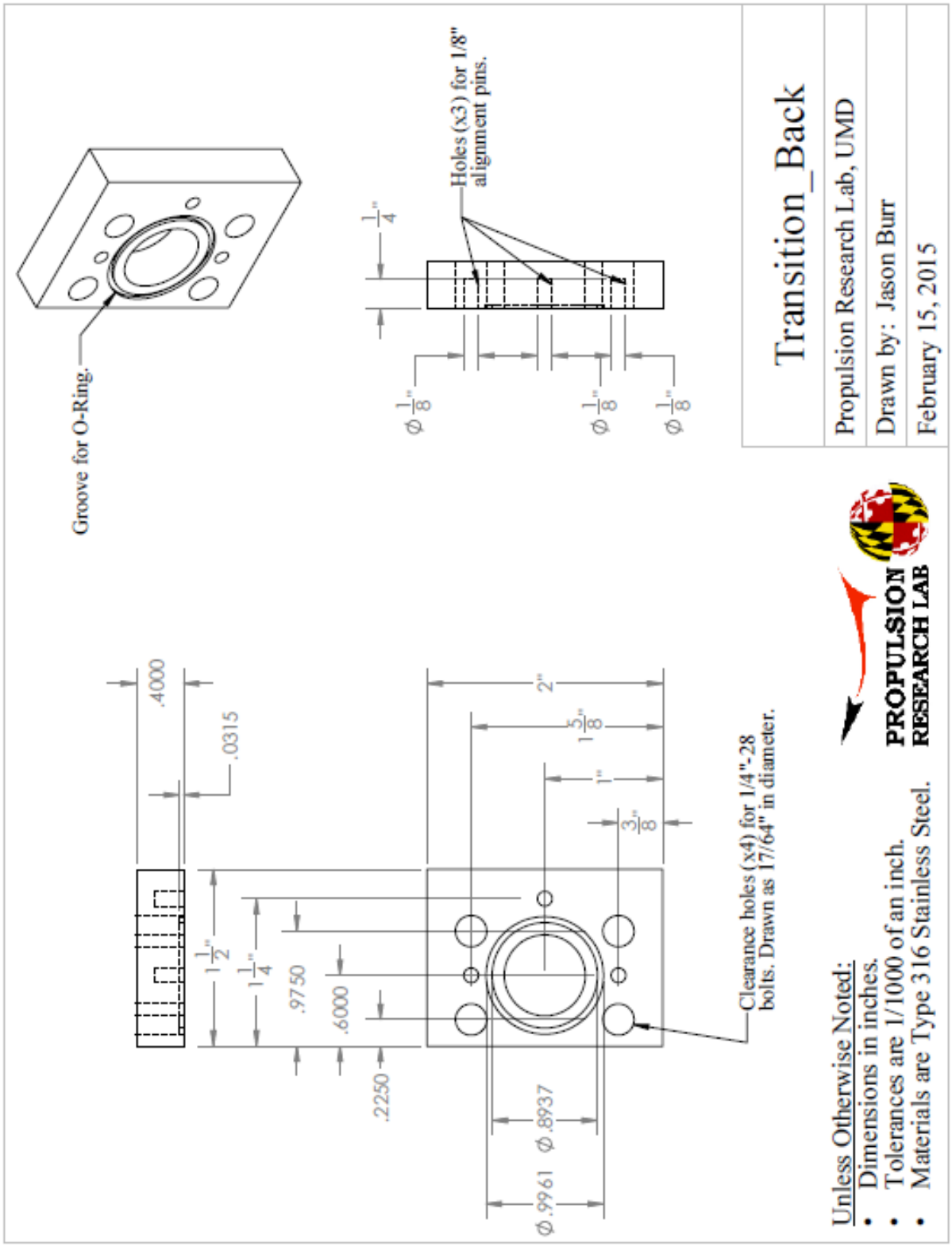
Transition_Back
Propulsion Research Lab, UMD
Drawn by: Jason Burr
February 15, 2015
PROPULSION RESEARCH LAB
Unless Otherwise Noted:
• Dimensions in inches.
• Tolerances are 1/1000 of an inch.
• Materials are Type 316 Stainless Steel.
Groove for O-Ring.
Holes (x3) for 1/8" alignment pins.
Clearance holes (x4) for 1/4"-28 bolts. Drawn as 17/64" in diameter.
.4000
.0315
.9750
.6000
.2250
.8937
.9961
2"

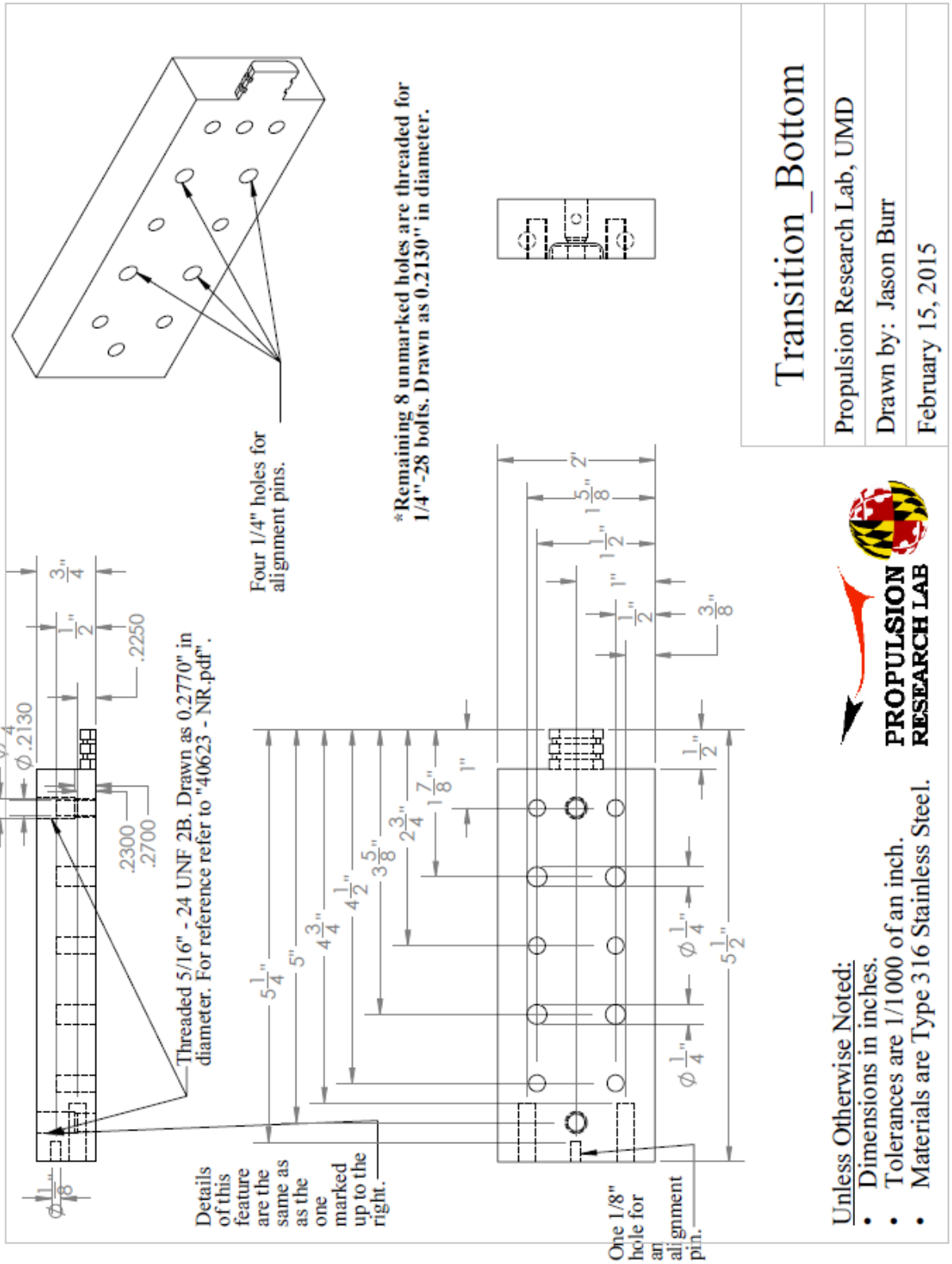
Transition_Bottom
Propulsion Research Lab, UMD
Drawn by: Jason Burr
February 15, 2015
PROPULSION RESEARCH LAB
Unless Otherwise Noted:
• Dimensions in inches.
• Tolerances are 1/1000 of an inch.
• Materials are Type 316 Stainless Steel.
Four 1/4" holes for alignment pins.
*Remaining 8 unmarked holes are threaded for 1/4"-28 bolts. Drawn as 0.2130" in diameter.
Threaded 5/16" - 24 UNF 2B. Drawn as 0.2770" in diameter. For reference refer to "40623 - NR.pdf".
Details of this feature are the same as as the one marked up to the right.
One 1/8" hole for an alignment pin.

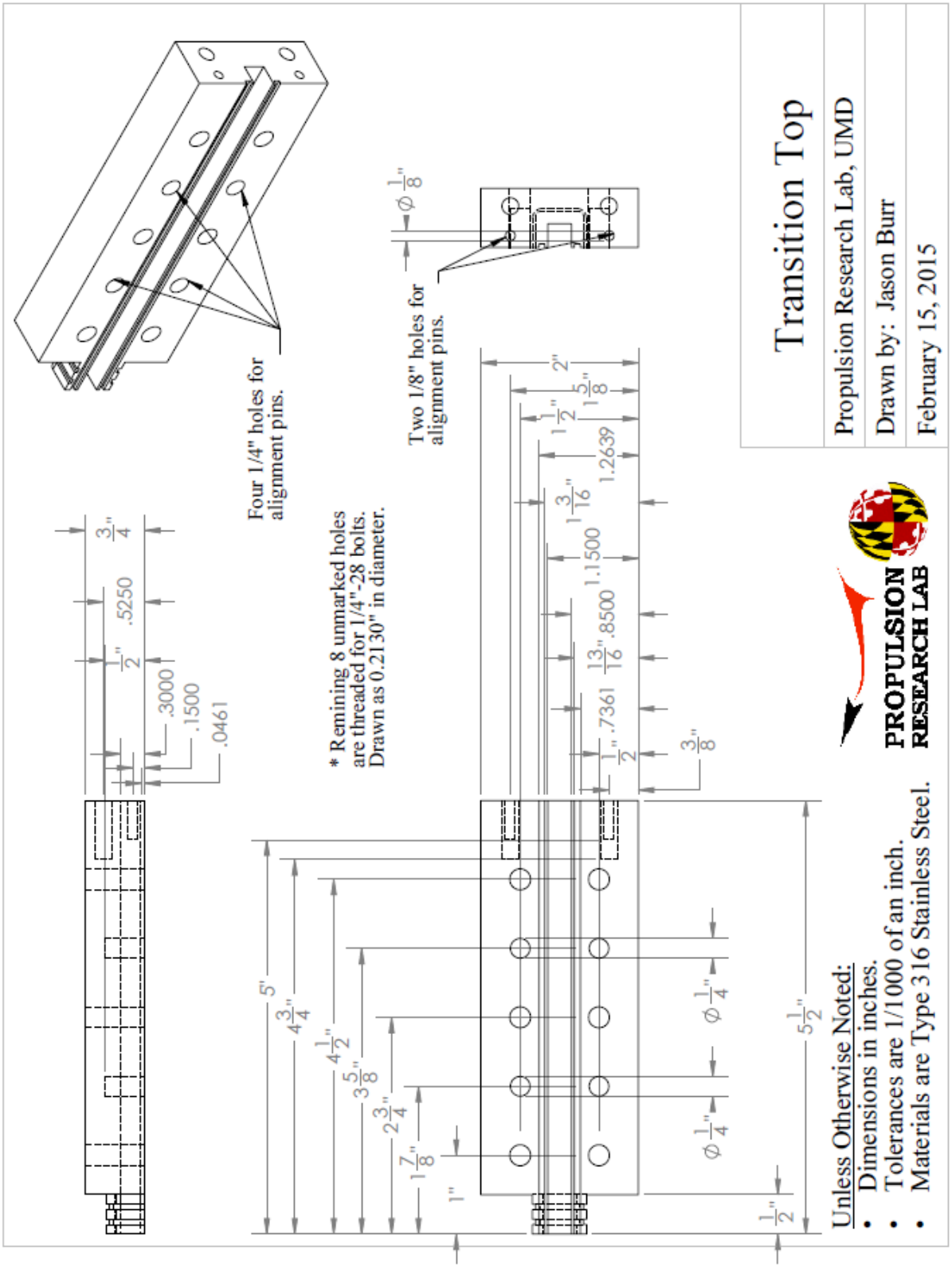
Transition Top
Propulsion Research Lab, UMD
Drawn by: Jason Burr
February 15, 2015
PROPULSION RESEARCH LAB
Four 1/4" holes for alignment pins.
Two 1/8" holes for alignment pins.
* Remining 8 unmarked holes are threaded for 1/4"-28 bolts. Drawn as 0.2130" in diameter.
Unless Otherwise Noted:
• Dimensions in inches.
• Tolerances are 1/1000 of an inch.
• Materials are Type 316 Stainless Steel.

Appendix C: Engineering Drawings of eLMDE

This appendix contains the engineering drawings for the most important components of the Extended Linear Model Detonation Engine (eLMDE) used for the methane detonation experiments. The dimensions in all of these drawings are provided in inches and the scale varies depending on the size of the part of assembly to highlight different design features.

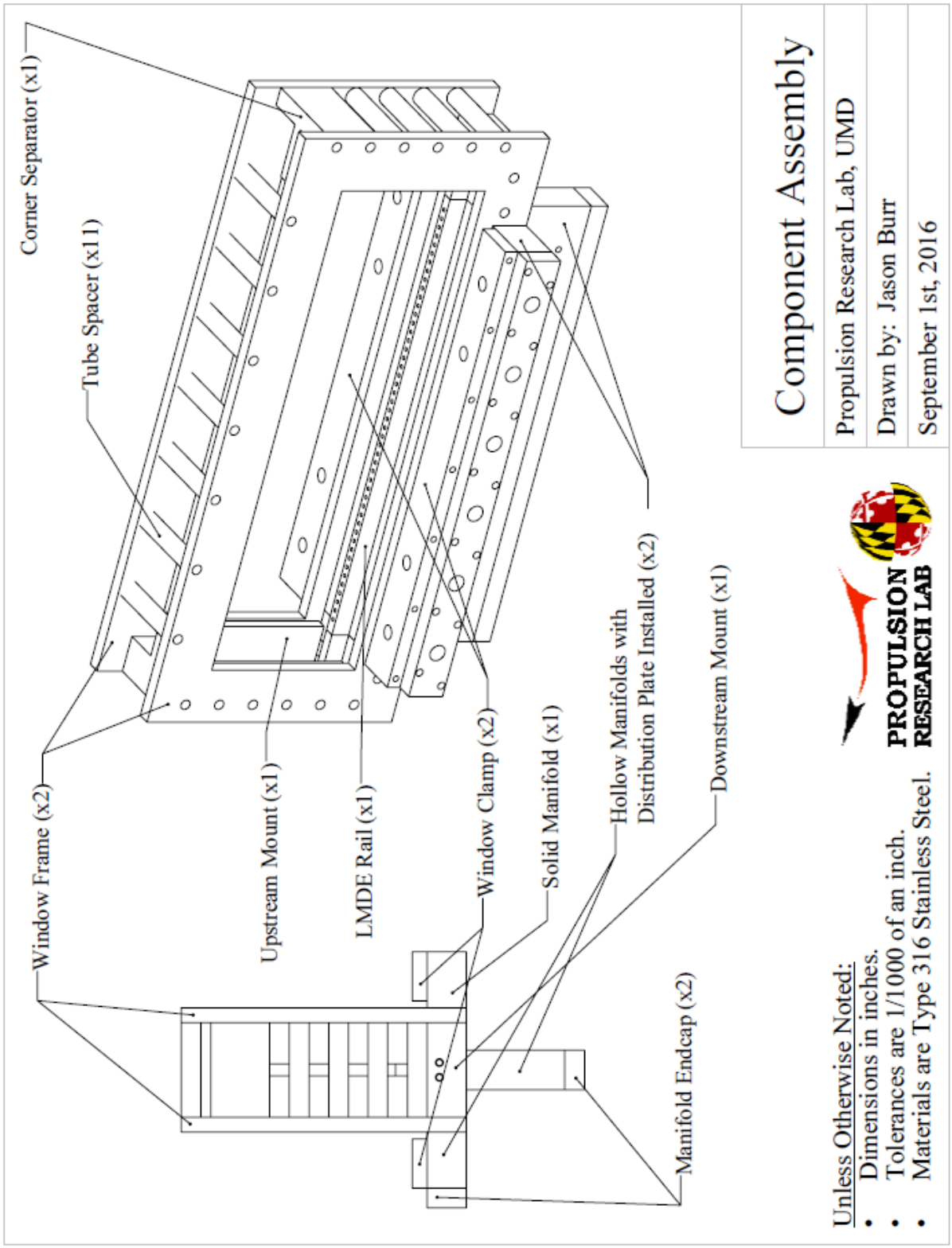
Corner Separator (x1)
Tube Spacer (x11)
Window Frame (x2)
Upstream Mount (x1)
LMDE Rail (x1)
Window Clamp (x2)
Solid Manifold (x1)
Hollow Manifolds with Distribution Plate Installed (x2)
Downstream Mount (x1)
Manifold Endcap (x2)
Component Assembly
Propulsion Research Lab, UMD
Drawn by: Jason Burr
September 1st, 2016
PROPULSION RESEARCH LAB
Unless Otherwise Noted:
• Dimensions in inches.
• Tolerances are 1/1000 of an inch.
• Materials are Type 316 Stainless Steel.

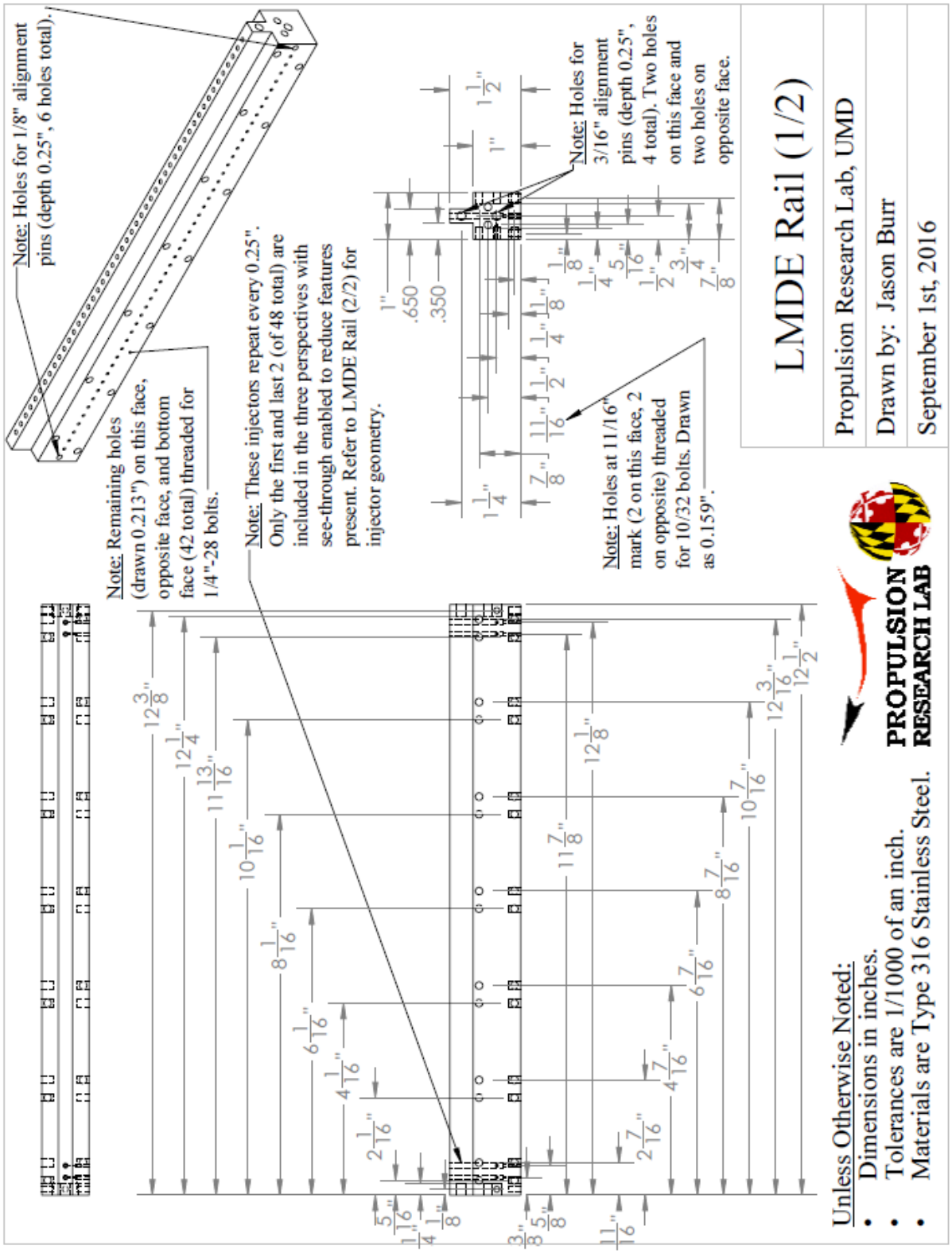
Note: Holes for 1/8" alignment pins (depth 0.25", 6 holes total).
Note: Remaining holes (drawn 0.213") on this face, opposite face, and bottom face (42 total) threaded for 1/4"-28 bolts.
Note: These injectors repeat every 0.25". Only the first and last 2 (of 48 total) are included in the three perspectives with see-through enabled to reduce features present. Refer to LMDE Rail (2/2) for injector geometry.
Note: Holes at 11/16" mark (2 on this face, 2 on opposite) threaded for 10/32 bolts. Drawn as 0.159".
Note: Holes for 3/16" alignment pins (depth 0.25", 4 total). Two holes on this face and two holes on opposite face.
LMDE Rail (1/2)
Propulsion Research Lab, UMD
Drawn by: Jason Burr
September 1st, 2016
PROPULSION RESEARCH LAB
Unless Otherwise Noted:
• Dimensions in inches.
• Tolerances are 1/1000 of an inch.
• Materials are Type 316 Stainless Steel.

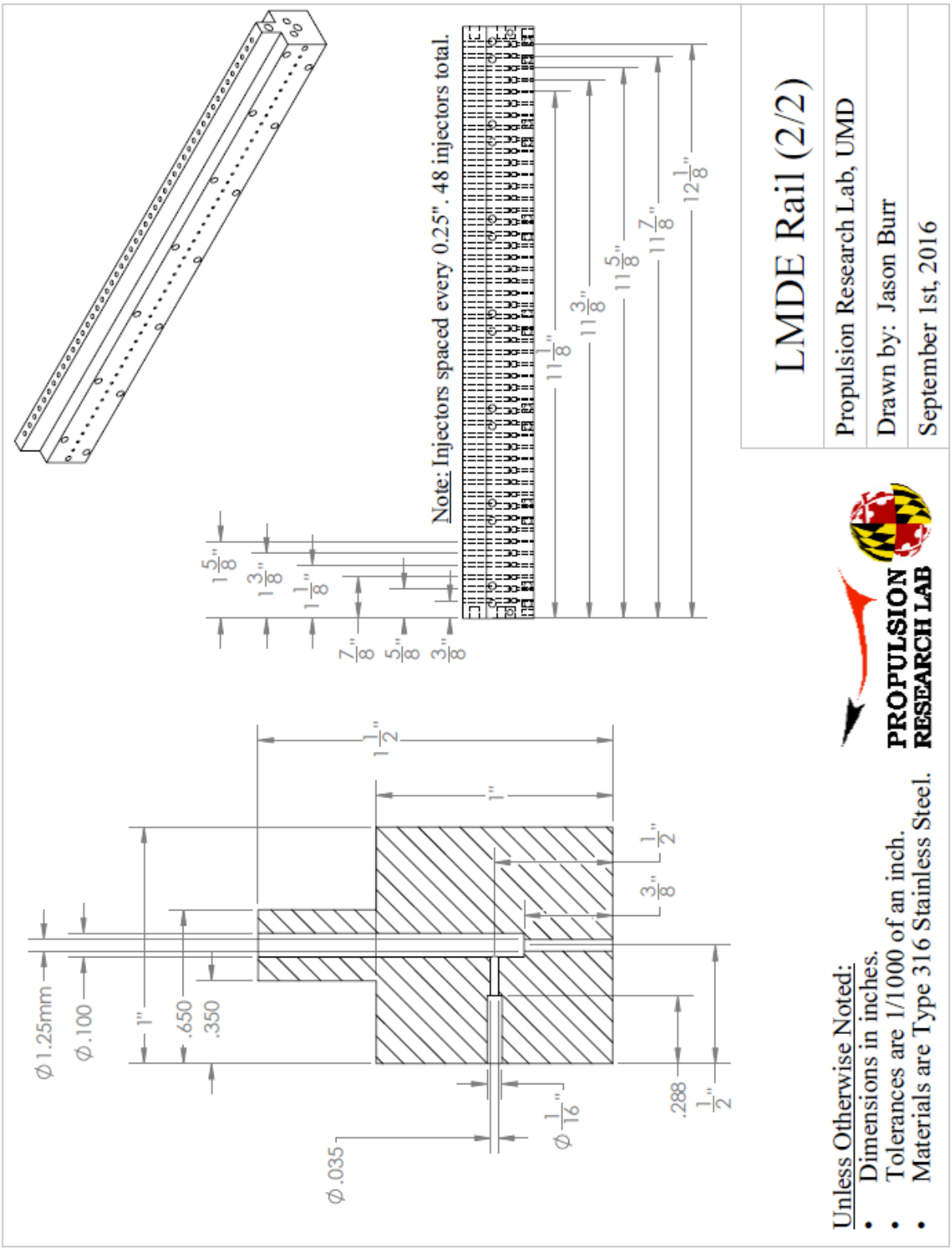
LMDE Rail (2/2)
Propulsion Research Lab, UMD
Drawn by: Jason Burr
September 1st, 2016
PROPULSION RESEARCH LAB
Unless Otherwise Noted:
• Dimensions in inches.
• Tolerances are 1/1000 of an inch.
• Materials are Type 316 Stainless Steel.
Note: Injectors spaced every 0.25". 48 injectors total.
Ø 1.25mm
Ø .100
1"
.650
.350
Ø .035
Ø 1/16"
.288
1/2"
3/8"
1/2"
1"
1 1/2"
3/8"
7/8"
5/8"
3/8"
1 5/8"
1 3/8"
1 1/8"
11 1/8"
11 3/8"
11 5/8"
11 7/8"
12 1/8"

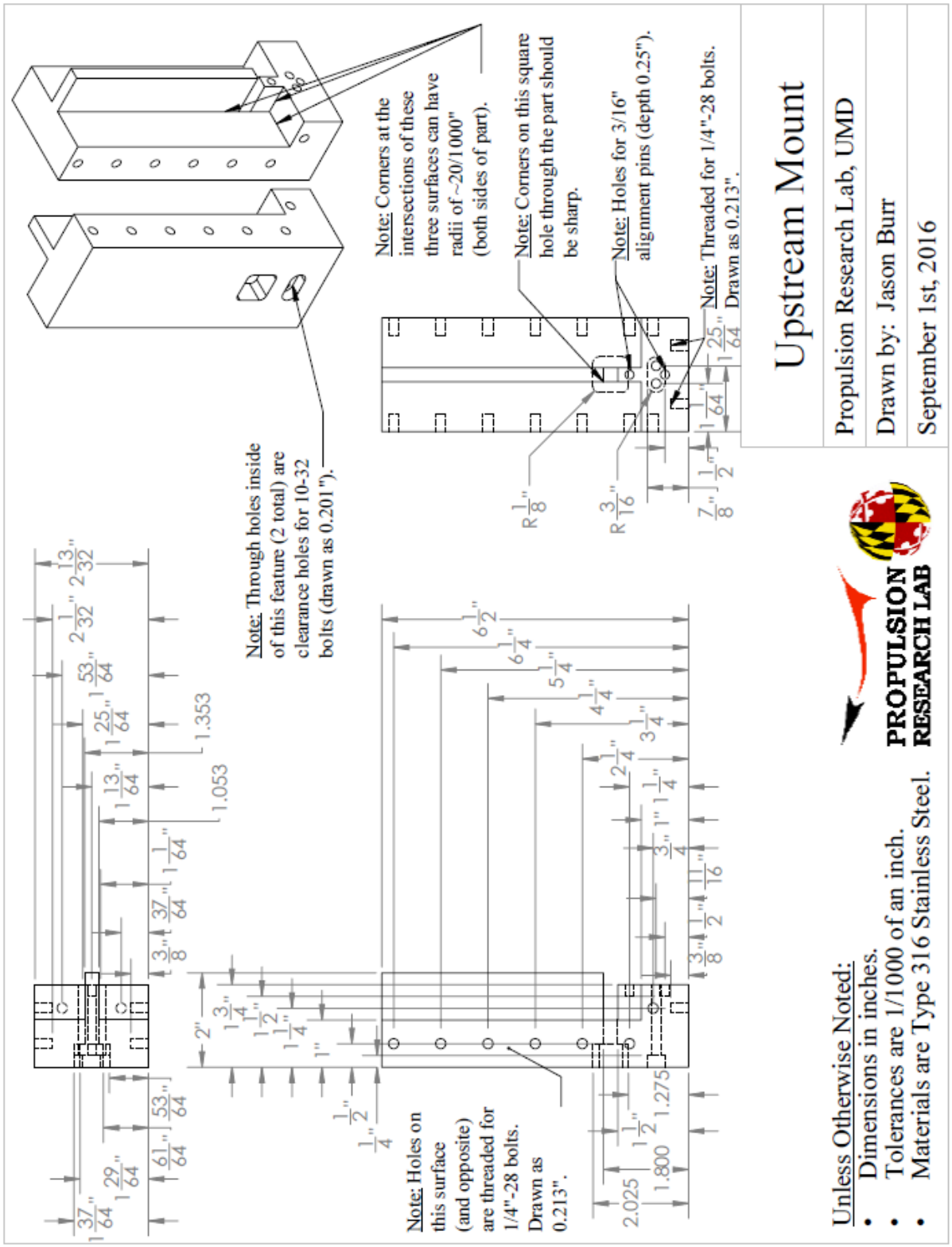
Upstream Mount
Propulsion Research Lab, UMD
Drawn by: Jason Burr
September 1st, 2016
PROPULSION RESEARCH LAB
Unless Otherwise Noted:
• Dimensions in inches.
• Tolerances are 1/1000 of an inch.
• Materials are Type 316 Stainless Steel.
Note: Through holes inside of this feature (2 total) are clearance holes for 10-32 bolts (drawn as 0.201").
Note: Corners at the intersections of these three surfaces can have radii of ~20/1000" (both sides of part).
Note: Corners on this square hole through the part should be sharp.
Note: Holes for 3/16" alignment pins (depth 0.25").
Note: Threaded for 1/4"-28 bolts. Drawn as 0.213".
Note: Holes on this surface (and opposite) are threaded for 1/4"-28 bolts. Drawn as 0.213".
1.353
1.053
2.025
1.800
1.275

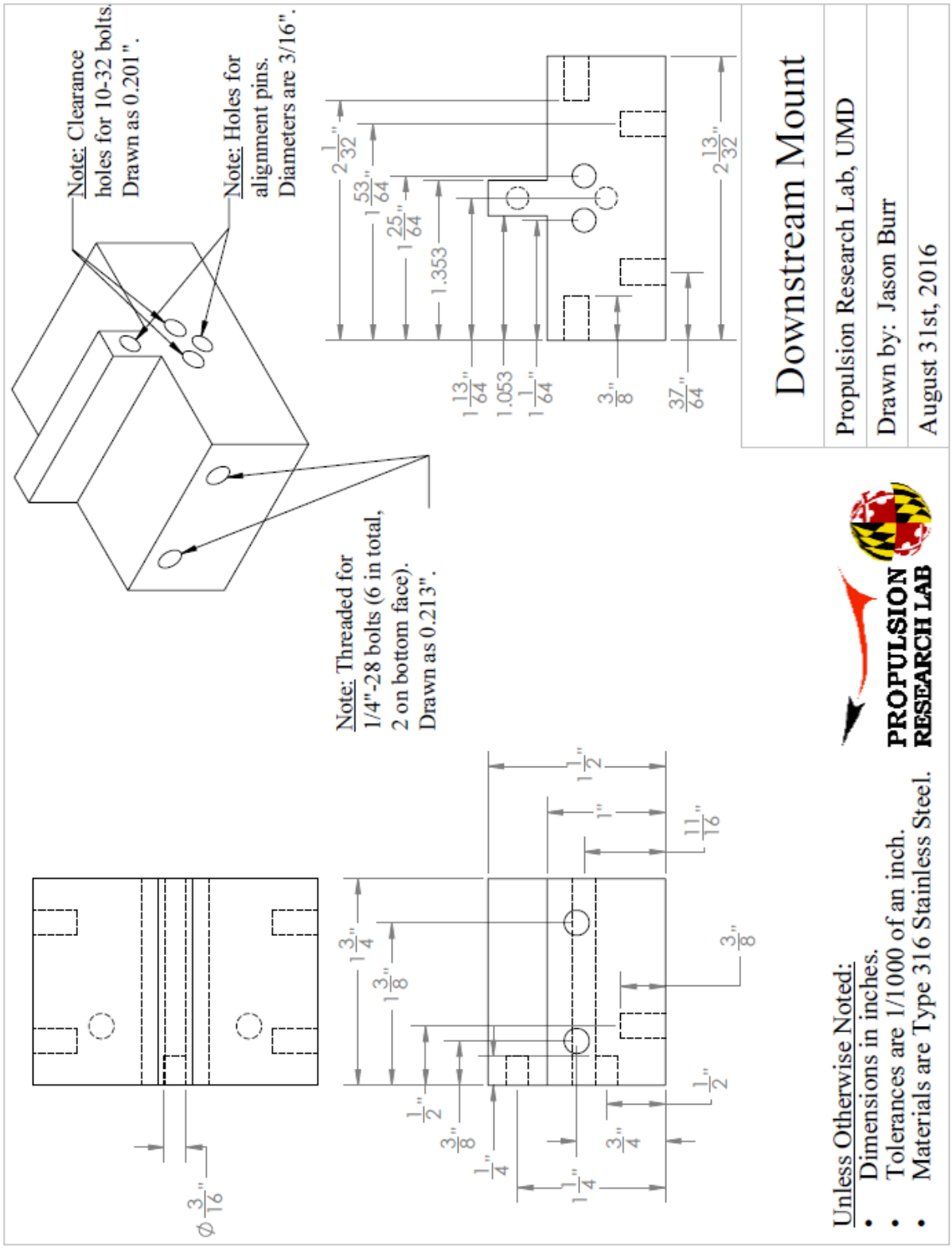
Note: Clearance holes for 10-32 bolts. Drawn as 0.201".
Note: Holes for alignment pins. Diameters are 3/16".
Note: Threaded for 1/4"-28 bolts (6 in total, 2 on bottom face). Drawn as 0.213".
Downstream Mount
Propulsion Research Lab, UMD
Drawn by: Jason Burr
August 31st, 2016
PROPULSION RESEARCH LAB
Unless Otherwise Noted:
• Dimensions in inches.
• Tolerances are 1/1000 of an inch.
• Materials are Type 316 Stainless Steel.

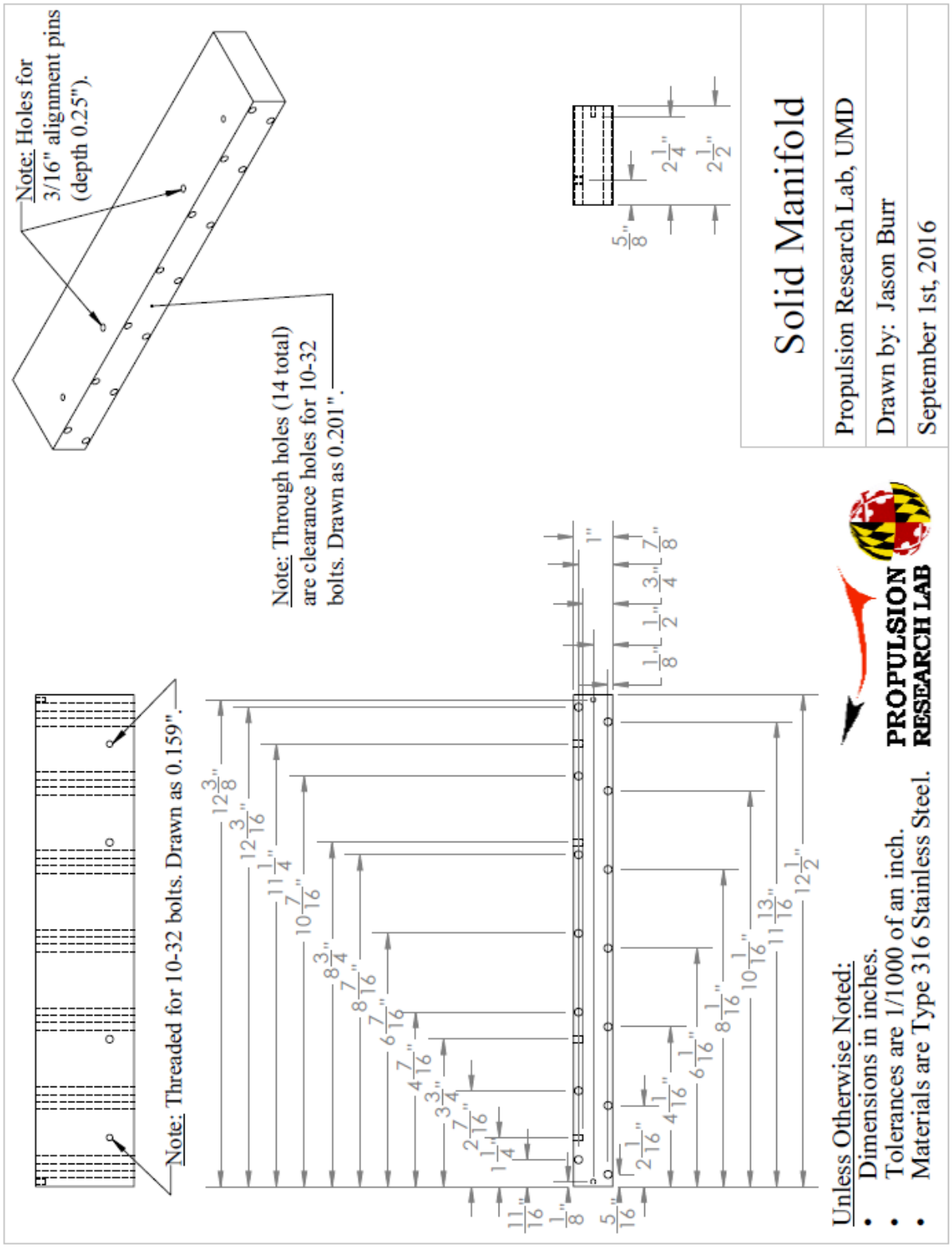
Note: Holes for 3/16" alignment pins (depth 0.25").
Note: Through holes (14 total) are clearance holes for 10-32 bolts. Drawn as 0.201".
Note: Threaded for 10-32 bolts. Drawn as 0.159".
Solid Manifold
Propulsion Research Lab, UMD
Drawn by: Jason Burr
September 1st, 2016
PROPULSION RESEARCH LAB
Unless Otherwise Noted:
• Dimensions in inches.
• Tolerances are 1/1000 of an inch.
• Materials are Type 316 Stainless Steel.

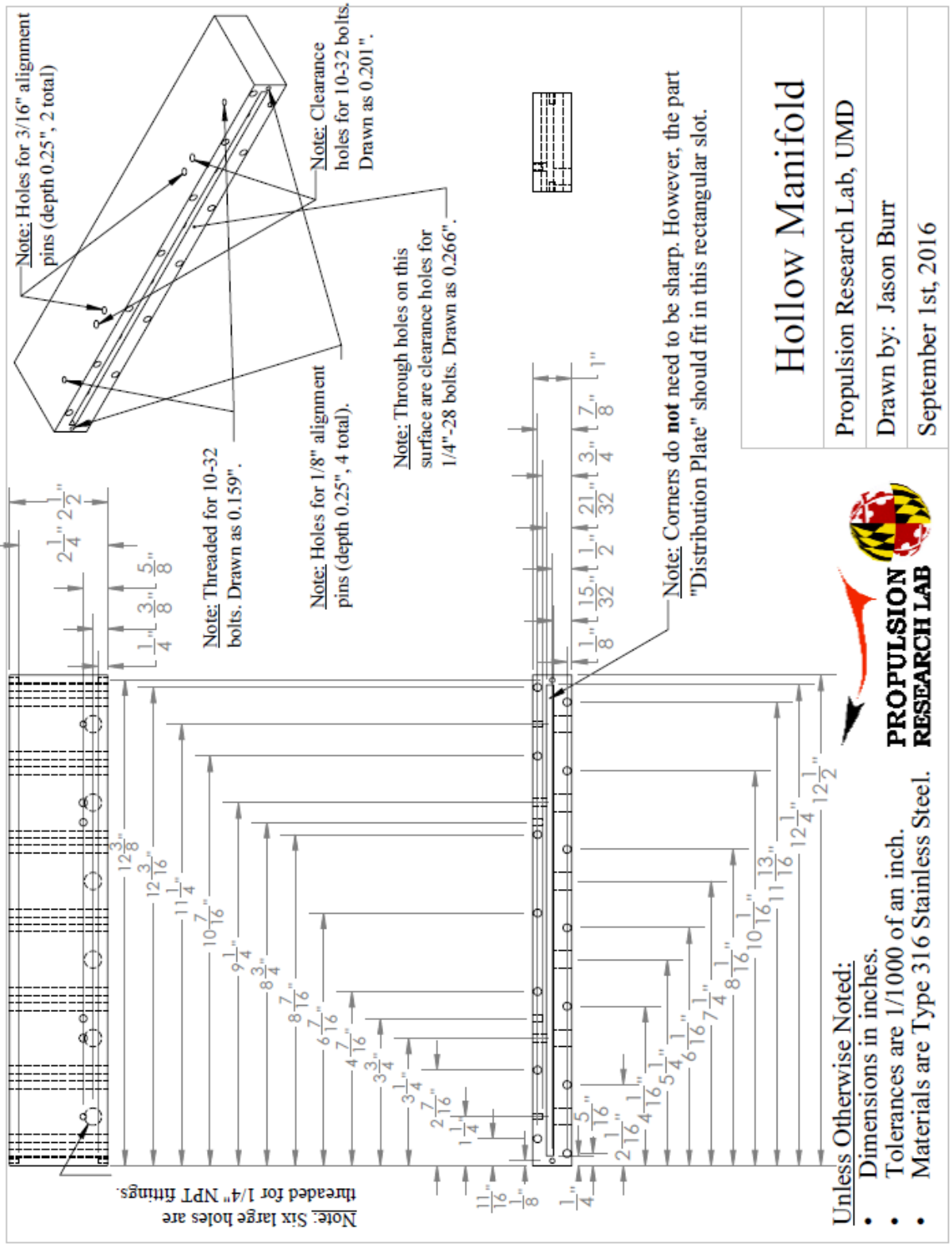
Hollow Manifold
Propulsion Research Lab, UMD
Drawn by: Jason Burr
September 1st, 2016
PROPULSION RESEARCH LAB
Unless Otherwise Noted:
• Dimensions in inches.
• Tolerances are 1/1000 of an inch.
• Materials are Type 316 Stainless Steel.
Note: Six large holes are threaded for 1/4" NPT fittings.
Note: Holes for 3/16" alignment pins (depth 0.25", 2 total)
Note: Threaded for 10-32 bolts. Drawn as 0.159".
Note: Holes for 1/8" alignment pins (depth 0.25", 4 total).
Note: Clearance holes for 10-32 bolts. Drawn as 0.201".
Note: Through holes on this surface are clearance holes for 1/4"-28 bolts. Drawn as 0.266".
Note: Corners do not need to be sharp. However, the part "Distribution Plate" should fit in this rectangular slot.

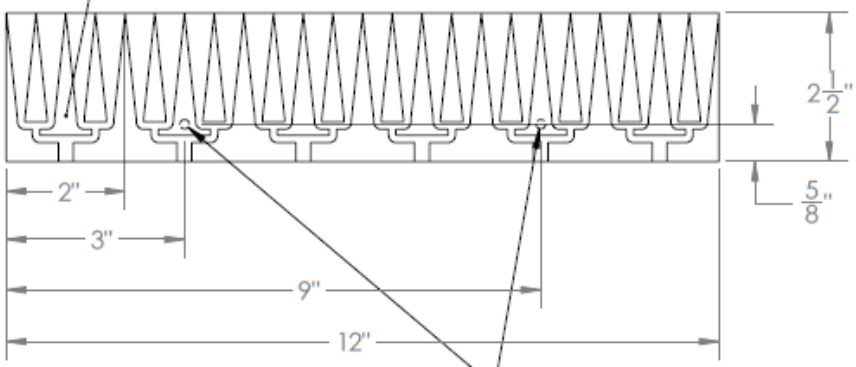

Note: Pattern repeats every two inches. Material removal depth is 1/16". Smallest groove width is 1/8".

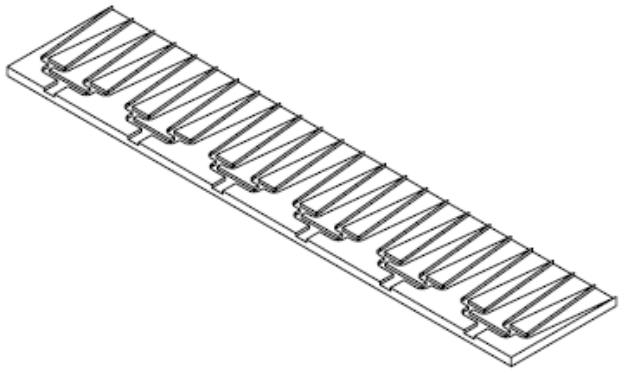

Note: Threaded for 10-32 bolts (2 total, depth 1/8"). Drawn as 0.159" in diameter. Hole starts from surface opposite grooved pattern.

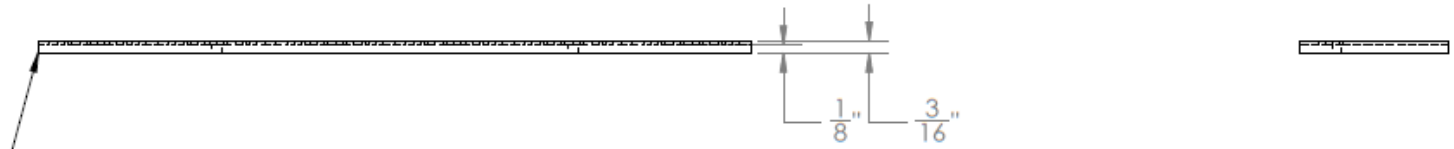

Note: These corners do **not** need to be sharp. This part needs to fit inside of the part "Hollow Manifold" (threaded holes align with clearance holes for securing insert).

Unless Otherwise Noted:
- Dimensions in inches.
- Tolerances are 1/1000 of an inch.
- Materials are Type 316 Stainless Steel.

PROPULSION RESEARCH LAB

Distribution Plate

Propulsion Research Lab, UMD

Drawn by: Jason Burr

September 1st, 2016

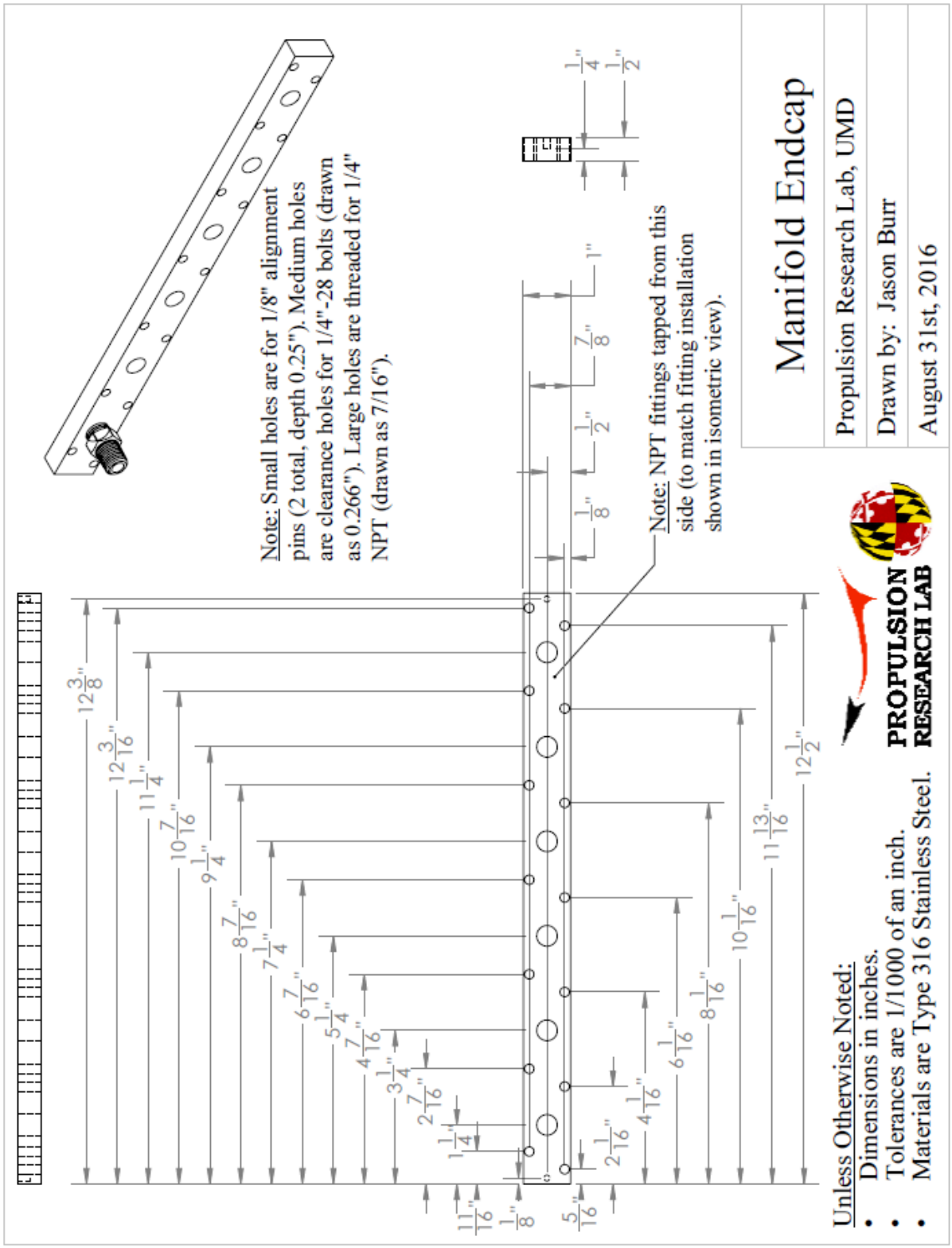
Manifold Endcap
Propulsion Research Lab, UMD
Drawn by: Jason Burr
August 31st, 2016
PROPULSION RESEARCH LAB
Note: Small holes are for 1/8" alignment pins (2 total, depth 0.25"). Medium holes are clearance holes for 1/4"-28 bolts (drawn as 0.266"). Large holes are threaded for 1/4" NPT (drawn as 7/16").
Note: NPT fittings tapped from this side (to match fitting installation shown in isometric view).
Unless Otherwise Noted:
Dimensions in inches.
Tolerances are 1/1000 of an inch.
Materials are Type 316 Stainless Steel.

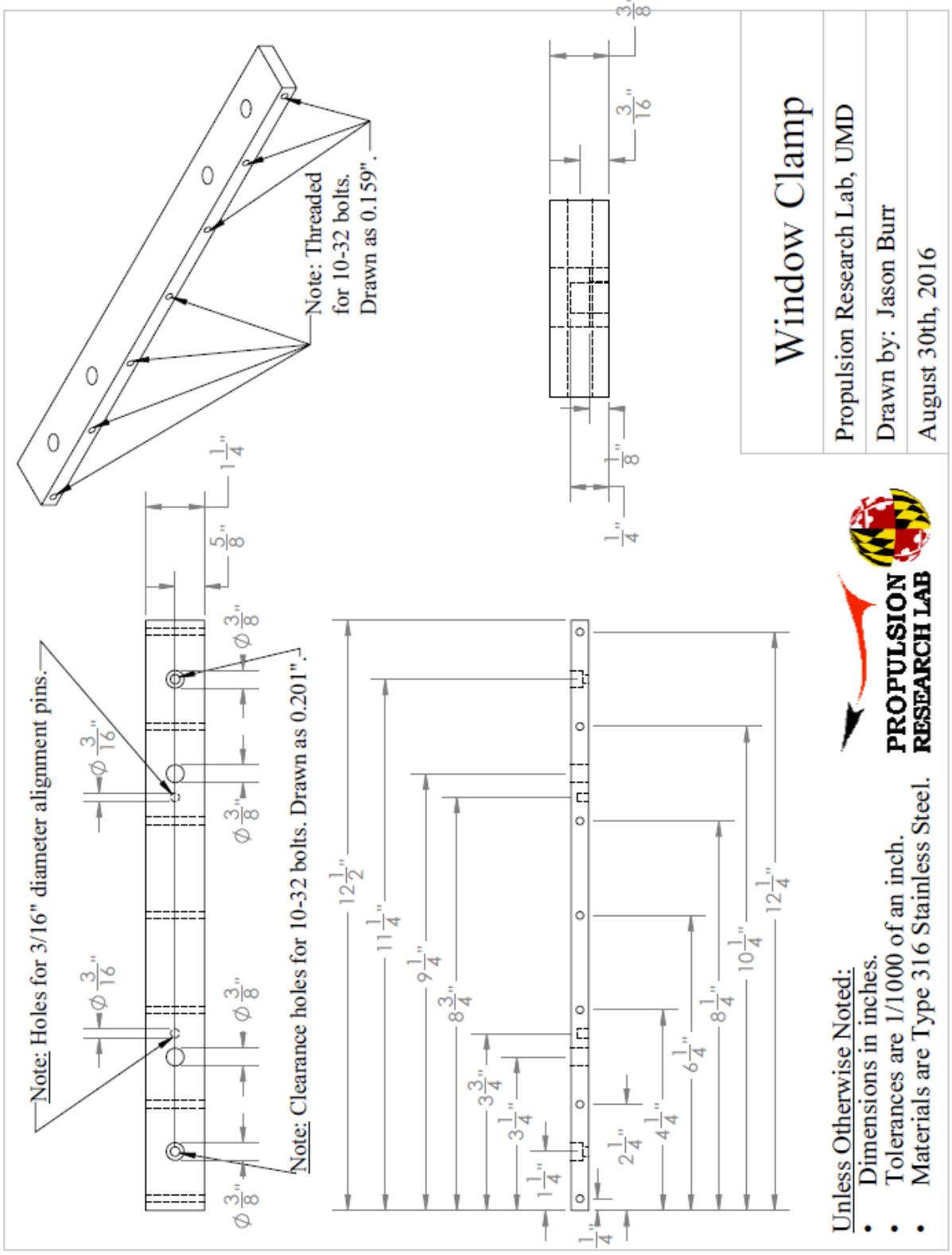
Window Clamp
Propulsion Research Lab, UMD
Drawn by: Jason Burr
August 30th, 2016
PROPULSION RESEARCH LAB
Unless Otherwise Noted:
• Dimensions in inches.
• Tolerances are 1/1000 of an inch.
• Materials are Type 316 Stainless Steel.
Note: Holes for 3/16" diameter alignment pins.
Note: Clearance holes for 10-32 bolts. Drawn as 0.201".
Note: Threaded for 10-32 bolts. Drawn as 0.159".

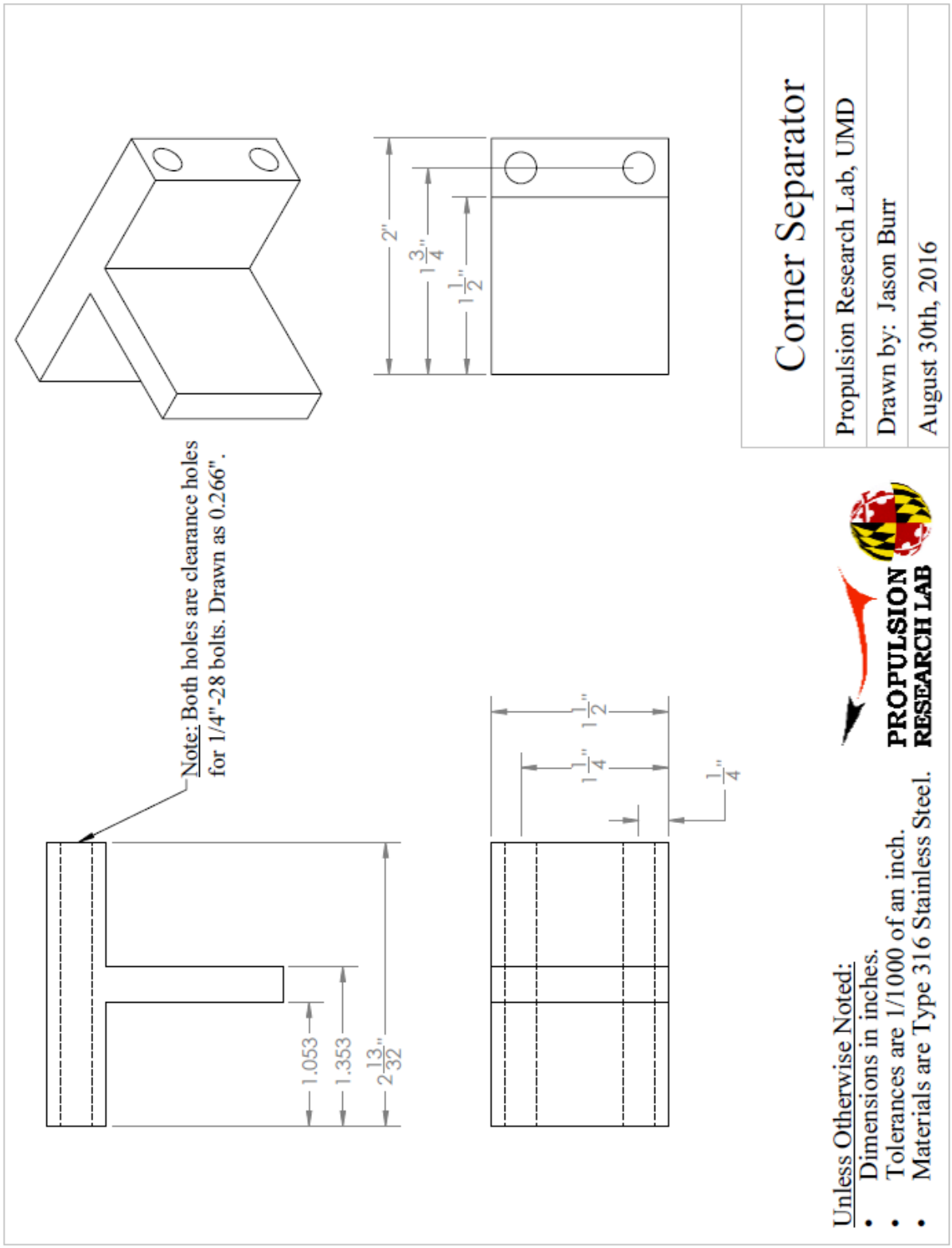
Corner Separator
Propulsion Research Lab, UMD
Drawn by: Jason Burr
August 30th, 2016
PROPULSION RESEARCH LAB
Unless Otherwise Noted:
• Dimensions in inches.
• Tolerances are 1/1000 of an inch.
• Materials are Type 316 Stainless Steel.
Note: Both holes are clearance holes for 1/4"-28 bolts. Drawn as 0.266".
1.053
1.353
2 13/32"
2"
1 3/4"
1 1/2"
1 1/2"
1 1/4"
1/4"

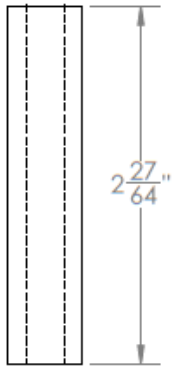

Note: Material for tube supplied (McMaster-Carr part #89495K485). Eleven spacers of given length are needed.

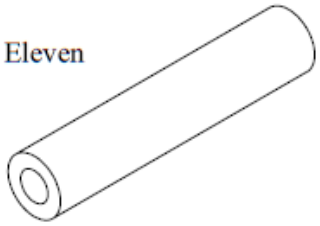

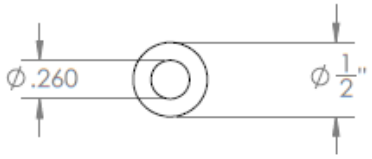

Unless Otherwise Noted:
- Dimensions in inches.
- Tolerances are 1/1000 of an inch.
- Materials are Type 316 Stainless Steel.

PROPULSION RESEARCH LAB

Tube Spacer

Propulsion Research Lab, UMD

Drawn by: Jason Burr

August 30th, 2016

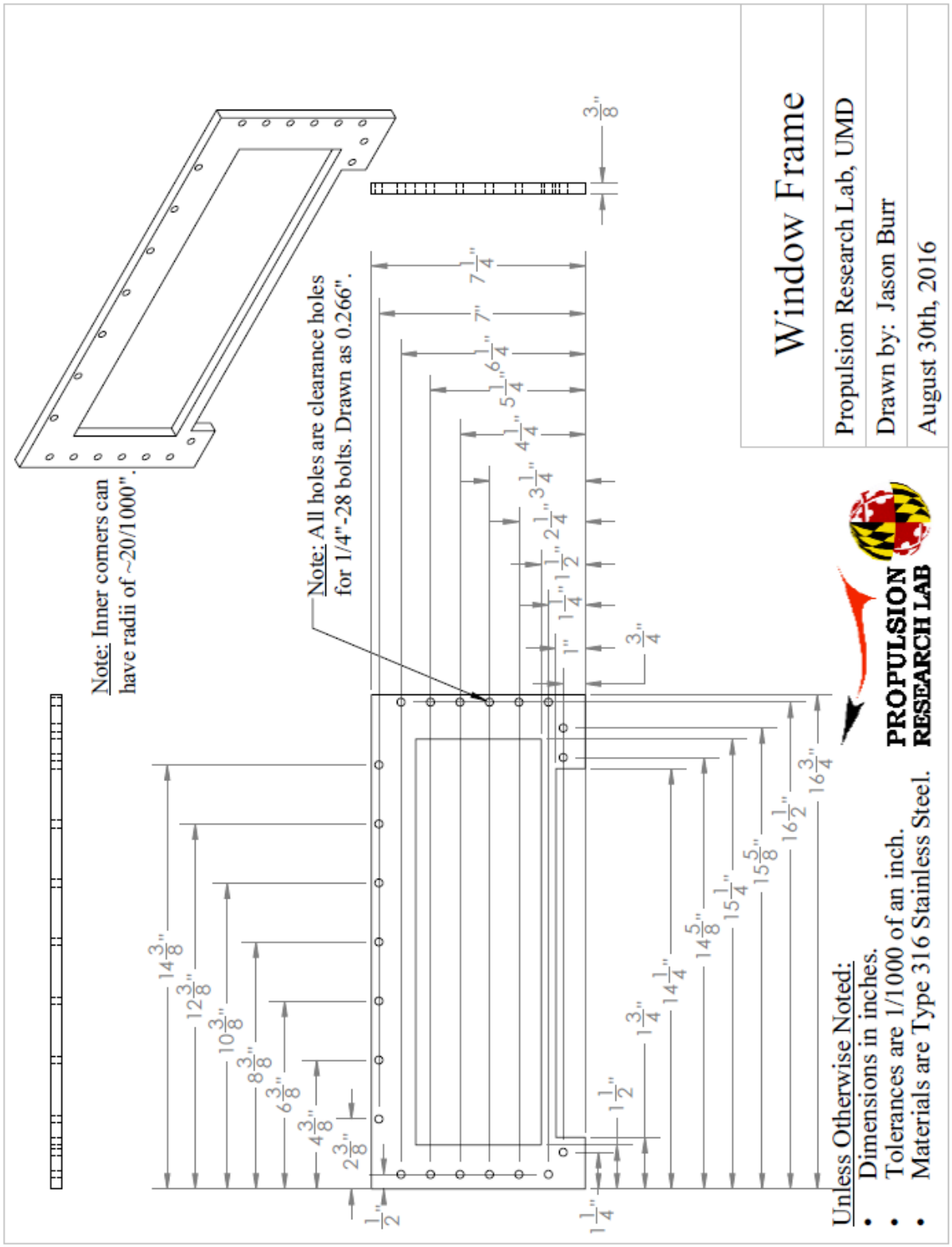
Window Frame
Propulsion Research Lab, UMD
Drawn by: Jason Burr
August 30th, 2016
PROPULSION RESEARCH LAB
Note: Inner corners can have radii of ~20/1000".
Note: All holes are clearance holes for 1/4"-28 bolts. Drawn as 0.266".
Unless Otherwise Noted:
• Dimensions in inches.
• Tolerances are 1/1000 of an inch.
• Materials are Type 316 Stainless Steel.

Appendix D: Partial Reaction Cantera Code

This appendix contains the custom Python 2.7 code developed by Jason R. Burr in December 2018 and used, in conjunction with the open-source chemical equilibrium software Cantera, to estimate the mixing-limited CJ detonation wave speeds described in Chapter 6. The code that follows iterates to find the tangent Rayleigh line to the partially reacted Hugoniot curve through a set of nested bisection iterations on temperature and specific volume. Execution of the code is achieved by the following command in the Python 2.7 environment:

$$gasCJ = findCJ(gas, mech, x, tol=1e\text{-}3) \tag{C.1}$$

Where "*gasCJ*" is the Cantera gas object corresponding to mixing-limited CJ state, "*gas*" is the Cantera gas object corresponding to the reactants, "*mech*" is the Cantera reaction mechanism, "*x*" is the mass fraction of equilibrium products at the final CJ state, and "*tol*" is the bisection method convergence tolerance.

```
## Set of Functions to Solve for Tangency of Partially Reacted Hugoniot Curves

# - - - - - - - - - - - - - - - - - - - - - - - - - - - - - - -
# Created by Jason R. Burr, December 2018
# - - - - - - - - - - - - - - - - - - - - - - - - - - - - - - -

# Import required components
from SDToolbox import * #import the SDToolbox
from numpy import * #allows array math

# Define tolerances and method for these functions
tol = 10**-3; #dv = tol*v1, dT = 100*tol*T1
diff = 10*tol;

def Sound(gas, rtol=1.0e-6, maxiter=5000):
    """
    Returns the speed of sound(s).  The gas is first set to an
    equilibrium state at the temperature and pressure of the gas, since
    otherwise the equilibrium sound speed is not defined. Units m/s
    """

    # Get the current gas state
    state  = gas.basis
    # Set the basis to mass
    gas.basis = 'mass'

    # Save the current state information
    T0 = gas.T
    x0 = gas.X;
    s0 = gas.s
    P0 = gas.P
    r0 = gas.density_mass;

    # Perturb the pressure up
    P1 = P0*(1 + tol/10);
    dP = P1 - P0 #pressure increment
    # And down
    P2 = P0 - dP #reduce by the same increment

    # STATE 1 - GAS AT HIGHER PRESSURE
    # Find the equilibrium conditions at the heightened pressure
    gas.SPX = s0, P1, x0
    rf1 = gas.density_mass; #kg/m3, frozen sound speed
    gas.equilibrate('SP', rtol=rtol, maxiter=maxiter)
    re1 = gas.density_mass; #kg/m3, equilibrium sound speed
```

```
    # STATE 2 - GAS AT LOWER PRESSURE
    # Find the equilibrium conditions at the heightened pressure
    gas.SPX = s0, P2, x0
    rf2 = gas.density_mass; #kg/m3, frozen sound speed
    gas.equilibrate('SP', rtol=rtol, maxiter=maxiter)
    re2 = gas.density_mass; #kg/m3, equilibrium sound speed

    # FROZEN SOUND SPEED
    dr_dp_f = (rf2 - rf1)/(P2 - P1);
    afrozen = math.sqrt(1/dr_dp_f);

    # EQUILIBRIUM SOUND SPEED
    dr_dp_e = (re2 - re1)/(P2 - P1);
    aequil = math.sqrt(1/dr_dp_e);

    # Set the gas basis back
    gas.TPX = T0, P0, x0
    gas.basis = state

    # Estimate using ideal gas relations
    k = gas.cp/gas.cv;
    aideal = math.sqrt(k*(gas_constant/gas.mean_molecular_weight)*T0);

    return aequil, afrozen, aideal

def findZero(a, b, fa, fb, method=1):
    """
    Function that estimates the location of the zero based off the boundaries.

    INPUT
    a = x-location of first point
    b = x-location of second point
    fa = function evaluation of point a
    fb = function evaluation of point b
    method (1 default):
        1 = bisection method. Ignores fa and fb. c = 0.5*(a +b)
        2 = linear interpolation. Fits a line between (a,fa) and (b,fb) such
            that the estimated zero is at (c,0)

    OUTPUT
    c = estimated location of function zero
    """

    # Check the value of method
    if method==1: #bisection method
        c = 0.5*(a + b);
```

```
    elif method==2: #linear interpolation
        c = (a*fb - b*fa)/(fb - fa);

    else:
        print 'Method not recognized. Bisection selected'
        c = 0.5*(a + b);

    return c

def gasPartial(T, v, x, mech, xf):
    """
    Function that creates a partial equilibrium of the gas at given T and v.

    INPUT
    T = gas temperature (K)
    v = gas specific volume (m3/kg)
    x = mole composition of unreacted species
    mech = reaction mechanism
    xf = reaction progress (mass basis). xf = 0 is no-reaction, xf = 1 is full

    OUTPUT
    gas = gas at partial equilibrium
    """

    # Gas objects for partial equilibrium
    gas2 = Solution(mech);
    gas2.basis = 'mass';

    # Initialize this gas as the original mixture
    gas2.TDX = T, 1/v, x;
    y1 = gas2.Y; #mass fraction of unreacted species

    # Equilibrate at constant T and V
    gas2.equilibrate('TV');
    y2 = gas2.Y; #mass fraction of reacted species

    # Mixture mass fraction
    ymix = y1*(1-xf) + y2*(xf);

    # Create the final gas
    gas = Solution(mech);
    gas.basis = 'mass';
    gas.TDY = T, 1/v, ymix;

    return gas
```

```
def errH(gas1,gas2):
    """
    Function that determines the difference in enthalpies for the mixtures

    INPUT
    gas1 = gas at pre-shock state
    gas2 = gas at post-shock state

    OUTPUT
    dh = difference between enthalpies if mass, momentum, and energy are conserved
    """

    # Grab properties of the first gas
    P1 = gas1.P; #Pa
    p1 = gas1.density_mass; #kg/m3
    h1 = gas1.enthalpy_mass; #J/kg

    # Grab properties of the second gas
    P2 = gas2.P; #Pa
    p2 = gas2.density_mass; #kg/m3
    h2 = gas2.enthalpy_mass; #J/kg

    # Solve for error in the two enthalpies
    dh = (h1 - h2) - (P1 - P2)*(1 + p1/p2)*(1/(2*p1));

    return dh


def findT(gas1, v, mech, xf, tol=1e-3):
    """
    Function that solves for the temperature of that satisfies the mass,
    momentum, and energy equations.

    INPUT
    gas1 = gas at pre-shock state
    v = target specific volume (kg/m)
    mech = reaction mechanism
    xf = reaction progress (mass basis). xf = 0 is no-reaction, xf = 1 is full
    tol = convergence tolerance of function evaluation (1e-3 default)

    OUTPUT
    gas2 = gas at converged post-shock state
    """
```

```
    # Get the gas initial temperature - solution should not be below this
    Tmin = gas1.T; #K
    # Grab the mass composition of the initial gas
    x = gas1.X;

    # Evaluate the error in enthalpy at the minimum temperature
    gas2 = gasPartial(Tmin, v, x, mech, xf);
    dh_min = errH(gas1,gas2);

    # Check to see if this is 0 (or less than)
    if dh_min==0:
        return gas2
    elif dh_min<0: #should NOT be the case
        print 'Adjusting minimum temperature guess...'
        # Start reducing guess on Tmin
        while dh_min<0:
            # Temperature reduction
            Tmin = Tmin - 10; #K, just by a small amount (should not be in here!)
            # Evaluate the error in enthalpy at the minimum temperature
            gas2 = gasPartial(Tmin, v, x, mech, xf);
            dh_min = errH(gas1,gas2);

    # Initialize a second temperature, and loop until these temperatures bound the
solution
    Tmax = 2*Tmin; #K
    flag = 0;
    while flag==0:
        # Evaluate the enthalpy error at this temperature
        gas2 = gasPartial(Tmax, v, x, mech, xf);
        dh_max = errH(gas1,gas2);

        # Consider the possible values of dh_max
        if abs(dh_max)<=tol: #right on with the guess
            flag = 1;
            return gas2
        else: #every other case

            if (dh_max)*(dh_min)>0: #same sign
                # Move the lower bound upwards
                dh_min = dh_max + 0;
                Tmin = Tmax + 0;
                # And change the upper bound
                Tmax = 2*Tmax;

            elif (dh_max)*(dh_min)<0: #different signs
                flag = 1;
```

```
    # Print the temperature bounds
    #print Tmin, Tmax

    # Start searching for the zero within these bounds
    dT = 1e6; #K, huge range on temperature span
    while dT>(100*tol): #order of 1K for tol = 1e-2

        # Temperature span
        dT = Tmax - Tmin; #K, temperature range

        # Estimate the zero guess
        Tc = findZero(Tmin, Tmax, dh_min, dh_max);

        # Check the gas error at this point
        gas2 = gasPartial(Tc, v, x, mech, xf);
        dh_c = errH(gas1,gas2);

        # Create an array of these (absolute) values before updating
        dh_array = abs(array([dh_min, dh_c, dh_max]));
        T_array = array([Tmin, Tc, Tmax]); #K, 3 temperatures

        # Check the error on the zero guess
        if (dh_c)*(dh_min)>0: #same signs as minimum
            Tmin = Tc + 0;
            dh_min = dh_c + 0;

        elif (dh_c)*(dh_min)<0: #different signs as minimum
            Tmax = Tc + 0;
            dh_max = dh_c + 0;

    # Find the minimum error
    Tbest = T_array[dh_array.argmin()]; #K, best temperature
    # Regenerate the gas
    gas2 = gasPartial(Tbest, v, x, mech, xf);

    # Return the (best) converged gas
    return gas2


def dPdv(gas1, v, mech, xf, tol=1e-3):
    """
    Function that solves for the slope of the Rayliegh line connecting gas1 to
    gas2 (specified by specific volume 'v') as well as the local slope of the
    Hugoniot at gas2 by perturbing specific volume 'v' by a small amount.
```

```
    INPUT
    gas1 = gas at pre-shock state
    v = target specific volume (kg/m)
    mech = reaction mechanism
    xf = reaction progress (mass basis). xf = 0 is no-reaction, xf = 1 is full
    tol = convergence tolerance of function evaluation (1e-3 default)

    OUTPUT
    gas2 = gas at converged post-shock state ('v')
    dPdvR = slope of Rayleigh line (Pa*m3/kg)
    dPdvH = local slope of Hugoniot (Pa*m3/kg)
    """

    # Properties of the initial gas
    v1 = 1/gas1.density_mass; #m3/kg
    P1 = gas1.P; #Pa

    # Ensure that 'v' is not equal to v1
    if v>=v1:
        v = (1-tol)*v1;

    # Find the solution for the Hugoniot at the specified 'v'
    gas2 = findT(gas1, v, mech, xf, tol);
    # Properties of this gas
    v2 = 1/gas2.density_mass; #m3/kg
    P2 = gas2.P; #Pa
    # Slope of the Rayleigh Line
    dPdvR = (P2 - P1)/(v2 - v1);

    # Perturb the specific volume to estimate the local slope in Hugoniot
    v3 = (1-diff)*v2;
    gas3 = findT(gas1, v3, mech, xf, tol);
    # Properties of this gas
    v3 = 1/gas3.density_mass; #m3/kg
    P3 = gas3.P; #Pa
    # Local slope of the Hugoniot
    dPdvH = (P3 - P2)/(v3 - v2);

    return gas2, dPdvR, dPdvH

def findCJ(gas1, mech, xf, tol=1e-3):
    """
    Function that solves for the specific volume of that satisfies the mass,
    momentum, and energy equations. Function iterates over specific volumes in
    the range 0 < v <= v1, and for each guess on 'v' iterates to find the
    corresponding Hugoniot temperature.
```

```
    INPUT
    gas1 = gas at pre-shock state
    mech = reaction mechanism
    xf = reaction progress (mass basis). xf = 0 is no-reaction, xf = 1 is full
    tol = convergence tolerance of function evaluation (1e-3 default)

    OUTPUT
    gas2 = gas at converged post-shock state (CJ)
    W = wave speed of converged detonation, m/s
    """

    # Grab specific volume of initial state
    v1 = 1/gas1.density_mass; #m3/kg

    # Define initial guesses on max and min specific volumes
    vmax = (1-tol)*v1; #m3/kg, solution must be on detonation branch of Hugoniot

    # Check reaction progress variable. If xf == 0, then output gas is input
    if xf==0:
        # Create a new gas at the slightly perturbed specific volume
        gas2 = findT(gas1, vmax, mech, xf, tol);

    else: #Adjust bounds on v to find solution for xf =/= 0
        # Check to see if the initial guess on vmax is too small!
        [gasMax, dPdvRmax, dPdvHmax] = dPdv(gas1, vmax, mech, xf, tol);
        dPmax = dPdvRmax - dPdvHmax; #>0 if v<vcj, <0 if v>vcj
        while dPmax>0:
            # Update the guess for vmax
            vmax = 0.5*(vmax + v1);
            # Check to see if the initial guess on vmax is too small!
            [gasMax, dPdvRmax, dPdvHmax] = dPdv(gas1, vmax, mech, xf, tol);
            dPmax = dPdvRmax - dPdvHmax; #>0 if v<vcj, <0 if v>vcj

        # Initialize a guess on vmin and iterate to bound the CJ state
        vmin = 0.9*vmax;
        [gasMin, dPdvRmin, dPdvHmin] = dPdv(gas1, vmin, mech, xf, tol);
        dPmin = dPdvRmin - dPdvHmin; #>0 if v<vcj, <0 if v>vcj
        # Iterate until dPmin>0
        while dPmin<=0:
            # Update the guess on vmin, vmin now becomes vmax
            vmax = vmin + 0;
            dPmax = dPmin + 0;
            vmin = 0.5*vmin;
            # Save the new properties of this point
            [gasMin, dPdvRmin, dPdvHmin] = dPdv(gas1, vmin, mech, xf, tol);
            dPmin = dPdvRmin - dPdvHmin; #>0 if v<vcj, <0 if v>vcj
```

```
    # Iterate with bounds to find convergence point
    dv = 1e6;
    count = 1;
    while dv>tol:

        # Update the range of specific volumes
        dv = vmax - vmin; #m3/kg

        # Estimate new center point
        vmid = findZero(vmin, vmax, dPmin, dPmax);

        # Solve for local difference in Rayleigh and Hugoniot lines
        [gas2, dPdvRmid, dPdvHmid] = dPdv(gas1, vmid, mech, xf, tol);
        # Difference in slopes
        dPmid = dPdvRmid - dPdvHmid;

        # Save the absolute value of errors and specific volumes
        dP_array = abs(array([dPmin, dPmid, dPmax]));
        v_array = array([vmin, vmid, vmax]);

        # Print the count and update
        #print count, vmin, vmid, vmax, dPmin, dPmid, dPmax, dv
        count = count + 1;

        # Check value of the output
        if (dPmid*dPmin)>=0: #same sign as minimum (or zero)
            dPmin = dPmid + 0;
            vmin = vmid + 0;
        else: #must be same sign as maximum
            dPmax = dPmid + 0;
            vmax = vmid + 0;

    # Regenerate the gas based off of the minimum slope error solution
    vbest = v_array[dP_array.argmin()];
    [gas2, dPdvRmid, dPdvHmid] = dPdv(gas1, vbest, mech, xf, tol);


# Grab properties from initial and final state
P1 = gas1.P; #Pa
p1 = gas1.density_mass; #kg/m3
P2 = gas2.P; #Pa
p2 = gas2.density_mass; #kg/m3

# Estimate detonation speed W from these parameters
W22 = (P1 - P2)/(p2*(1 - p2/p1)); #m2/s2
```

```
    W2 = sqrt(W22); #m/s, speed of slow behind detonation wave (in wave frame)
    W = (p2/p1)*W2; #m/s, detonation speed

    return gas2, W


def findVN(gas1, mech, W, tol=1e-3):
    """
    Function that solves for the vonNeumann state that satisfies the mass,
    momentum, and energy equations. Function iterates over specific volumes in
    the range 0 < v <= v1, and for each guess on 'v' iterates to find the
    corresponding shocked-Hugoniot temperature.

    INPUT
    gas1 = gas at pre-shock state
    mech = reaction mechanism
    W = wave speed of converged detonation, m/s
    tol = convergence tolerance of function evaluation (1e-3 default)

    OUTPUT
    gas2 = gas at converged post-shock state (VN)
    """

    # Grab initial state properties
    gas1.basis = 'mass';
    P1 = gas1.P; #Pa
    v1 = 1/gas1.density_mass; #m3/kg
    X1 = gas1.X; #mole fractions

    # Assume a value for the vonNeumann specific volume
    v2 = 0.5*v1;
    # Solve for the vonNeumann pressure (mass+momentum)
    P2 = P1 + (1 - v2/v1)*(W*W)/v1; #Pa
    # Create the gas
    gas2 = Solution(mech);
    gas2.basis = 'mass'
    gas2.DPX = 1/v2, P2, X1

    # Evaluate the error in enthalpy
    dh = errH(gas1,gas2)
    # NOTE: dh>0 if v2<vVN, dh<0 if v2>vVN

    # Consider the 3 cases for the error
    if dh==0: #exact match, return vonNeumann gas
        return gas2
```

```
elif dh>0: #then v2<vVN
    # Define the current bounds
    vmax = v2+0;
    Pmax = P2+0;
    dhmax = dh+0;
    # Loop until upper bound is discovered
    while dh>0:
        # Update to a new guess
        vmin = vmax+0;
        Pmin = Pmax+0;
        dhmin = dhmax+0;

        # Guess between previous minimum and max
        vmax = 0.5*(vmin + v1);
        Pmax = P1 + (1 - vmax/v1)*(W*W)/v1; #Pa

        # Set this gas
        gas2.DPX = 1/vmax, Pmax, X1;

        # Error output
        dh = errH(gas1,gas2);
        dhmax = dh+0;

else: #then v2>vVN
    # Define the current bounds
    vmin = v2+0;
    Pmin = P2+0;
    dhmin = dh+0;
    # Loop until new bound is discovered
    while dh<0:
        # Update to new guess
        vmax = vmin+0;
        Pmax = Pmin+0;
        dhmax = dhmin+0;

        # Guess half of current max
        vmin = 0.5*vmax;
        Pmin = P1 + (1 - vmin/v1)*(W*W)/v1; #Pa

        # Set this gas
        gas2.DPX = 1/vmin, Pmin, X1;

        # Error output
        dh = errH(gas1,gas2);
        dhmin = dh + 0;
```

```
    # Begin bisection method until delta_v is less than tol
    while abs(vmax-vmin)>(tol/10): #can be more accurate since nested iteration is not
required

        # Solve for new center point
        vmid = findZero(vmin, vmax, Pmin, Pmax);
        Pmid = P1 + (1 - vmid/v1)*(W*W)/v1; #Pa

        # Set this gas
        gas2.DPX = 1/vmid, Pmid, X1;

        # Error output
        dhmid = errH(gas1,gas2);

        # Conditional output
        if dhmid==0:
            return gas2
        elif dhmid*dhmax>0: #same sign as dhmax
            vmax = vmid+0;
            dhmax = dhmid+0;
        else: #same sign as dhmin
            vmin = vmid+0;
            dhmin = dhmid+0;

    return
```

Bibliography

G. D. Roy, S. M. Frolov, A. A. Borisov, and D. W. Netzer. Pulse detonation propulsion: challenges, current status, and future perspective. Progress in Energy and Combustion Science, 30(6):545-672, 2004.

F. A. Bykovskii, S. A. Zhdan, and E. F. Vedernikov. Continuous Spin Detonations. Journal of Propulsion and Power, 22(6):1204-1216, 2006.

F. K. Lu and E. M. Braun. Rotating Detonation Wave Propulsion: Experimental Challenges, Modeling, and Engine Concepts. Journal of Propulsion and Power, 30(5):1125-1142, 2014.

M. Hishida, T. Fujiwara, and P. Wolanski. Fundamentals of rotating detonations. Shock Waves 19(1):1-10, 2009.

D. Schwer and K. Kailasanath. Numerical investigation of the physics of rotating-detonation-engines. Proceedings of the Combustion Institute, 33(2):2195-2202, 2011.

J. A. Nicholls, R. E. Cullen, and K. W. Ragland. Feasibility studies of a rotating detonation wave rocket motor. Journal of Spacecraft and Rockets, 3(6):893-898, 1966.

P. I. Shen and T. C. Adamson Jr. Theoretical Analysis of a Rotating Two-Phase Detonation in Liquid Rocket Motors. Astronautica Acta, 17(4):715-728, 1972.

K. Kailasanath. Review of Propulsion Applications of Detonation Waves. AIAA Journal, 38(9):1698-1708, 2000.

P. Wolanski. Detonative propulsion. Proceedings of the Combustion Institute, 34(1):125-158, 2013.

F. Falempin, E. Daniau, F. Getin, F. Bykovskii, and S. Zhdan. Toward a Continuous Detonation Wave Rocket Engine Demonstrator. In 14th AIAA/AHI Space Planes and Hypersonic Systems and Technologies Conference, AIAA Paper 2006-7956, Nov. 2006.

B. V. Voitsekhovsky. Stationary detonation. Reports of USSR Academy of Sciences, 129(6):1254-1256, 1959.

W. P. Sommers and R. B. Morrison. Simulation of Condensed-Explosive Detonation Phenomena with Gases. The Physics of Fluids, 5:241, 1962.

E. K. Dabora, J. A. Nicholls, and R. B. Morrison. The influence of a compressible boundary on the propagation of gaseous detonation. Symposium (International) on Combustion, 10(1):817-830, 1965.

M. Sichel and J. C. Foster. The ground impulse generated by a plane fuel-air explosion with side relief. Acta Astronautica, 6(3-4):243-256, 1979.

L. Thomas, F. Schauer, J. Hoke, and A. Naples. Buildup and Operation of a Rotating Detonation Engine. In 49th AIAA Aerospace Sciences Meeting, AIAA Paper 2011-602, Jan. 2011.

J. Kindracki, P. Wolanski, and Z. Gut. Experimental research on the rotating detonation in gaseous fuels-oxygen mixtures. Shock Waves, 21(2):75:84, 2011.

B. A Rankin, D. R. Richardson, A. W. Caswell, A. G. Naples, J. L. Hoke, and F. R. Schauer. Chemiluminescence imaging of an optically accessible non-premixed rotating detonation engine. Combustion and Flame, 176(1):12-22, 2017.

Y. Shao and J. P. Wang. Continuous Detonation Engine and Effects of Different Types of Nozzle on Its Propulsion Performance. Chinese Journal of Aeronautics, 23(6):647-652, 2010.

N. Tsuboi, Y. Watanabe, T. Kojima, and A. Koichi Hayashi. Numerical estimation of the thrust performance on a rotating detonation engine for a hydrogen-oxygen mixture. Proceedings of the Combustion Institute, 35(2):2005-2013, 2015.

R. Zhou and J. P. Wang. Numerical investigation of flow particle paths and thermodynamic performance of continuously rotating detonation engines. Combustion and Flame, 159(12):3632-3645, 2012.

C. A. Nordeen, D. Schwer, F. Schauer, J. Hoke, T. Barber, and B. Cetegen. Thermodynamic model of a rotating detonation engine. Combustion, Explosion, and Shock Waves, 50:568-577, 2014.

W. Fickett and W. C. Davis, Detonation Theory and Experiment (Dover Publications, Inc., New York, 2000)

B. V. Voitsekhovskii, V. V. Mitrofanov, and M.E. Topchiyan. Structure of the detonation front in gases (survey). Combustion, Explosion, and Shock Waves, 5(3):267-273, 1969.

J. S. Lee, The Detonation Phenomenon (Cambridge University Press, New York, 2008)

A. I. Gavrikov, A. A. Efimenko, and S. B. Dorofeev. A Model for Detonation Cell Size Prediction from Chemical Kinetics. Combustion and Flame 120(1):19-33, 2000.

K. I. Shchelkin and Y. K. Troshin, Gasdynamics of Combustion (Mono Book Corportation, Baltimor, 1965)

H. D. Ng. The effect of chemical reaction kinetics on the structure of gaseous detonations. Ph.D. Thesis, McGill University, 2005.

M. Kaneshige and J.E. Shepherd. Detonation database. Technical Report FM97-8, GALCIT, July 1997 (http://www.galcit.caltech.edu/detn_db/html/)

R. Knystautas, C. Guiaro, J. H. S. Lee, and A. Sulmistras. Measurements of Cell Size in Hydrocarbon-Air Mixtures and Predictions of Critical Tube Diameter, Critical Initiation Energy, and Detonability Limits. In Dynamics of Shock Waves, Explosions, and Detonations, ed. J. R. Bowen, N. Manson, A. K. Oppenheim, and R.I. Soloukhin (1985)

W. H. Sargent and R. A. Gross. Detonation Wave Hypersonic Ramjet. American Rocket Science Journal, 30(6), 1960

Y. B Zeldovich. To the Question of Energy Use of Detonation Combustion. Zhurnal Teknicheskoi Fiziki, 10(17):1453-1461, 1940.

E. Wintenberger and J. E. Shepherd. Stagnation Hugoniot Analysis for Steady Combustion Waves in Propulsion Systems. Journal of Propulsion and Power, 22(4), 2006.

C. Li, K. Kailasanath, and E. S. Oran. Detonation structures behind oblique shocks. Physics of Fluids, 6(4):1600-1611, 1994.

G. P. Menees, H. G. Adelman, J. Cambier, and J. V. Bowles. Wave combustors for trans-atmospheric vehicles. Journal of Propulsion and Power, 8(3):709-713, 1992.

D. Li, K. Kailasanath, E. S Oran, A. M. Landsberg, and J. P Boris. Dynamics of oblique detonations in ram accelerators. Shock Waves, 5(1):97-101, 1995.

K. Kailasanath. Research on Pulse Detonation Combustion Systems: A Status Report. In 47th AIAA Aerospace Sciences Meeting, AIAA Paper 2009-631, 2009.

A. St. George, R. Driscoll, V. Anand, S. Randall, D. Munday, and E. J. Gutmark. Development of a Rotating Detonation Engine Facility at the University of Cincinnati. In 53rd AIAA Aerospace Sciences Meeting, AIAA Paper 2015-0635, 2015.

A. Naples. Recent progress in detonation at air force research labs. In International Workshop on Detonation for Propulsion, Busan, Korea, 2011.

R. T. Fievisohn and K. H. Yu. Steady-State Analysis of Rotating Detonation Engine Flowfields with the Method of Characteristics. Journal of Propulsion and Power, 33(1):89-99, 2017.

F. K. Lu, R. Miller, M. R. Nalim, and K. H. Yu. Introduction: Special Section on Pressure Gain Combustion. Journal of Propulsion and Power, 33(1):16, 2017.

R. M. Clayton and R. S. Rogero. Experimental Measurements on a Rotating Detonation-Like Wave Observed During Liquid Rocket Resonant Combustion. Jet Propulsion Laboratory Technical Report No. 32-788, 1965.

T. C. Adamson Jr. and G. R. Olsson. Performance Analysis of a Rotating Detonation Wave Rocket Engine. Astronautica Acta, 13(4):405-415, 1967.

F. A. Bykovskii and E.F. Vedernikov. Continuous detonation combustion of an annular gas-mixture layer. Combustion, Explosion and Shock Waves, 32(5):489:491, 1996.

B. V. Voitsekhovskii. Maintained detonations. Soviet Physics Doklady, 4(1):1207, 1960.

R. Huff, M. D. Polanka, M. J. McClearn, F. R. Schauer, M. Fotia, and J. L. Hoke. A Disk Rotating Detonation Engine Part 1: Design and Buildup. In 2018 AIAA Aerospace Sciences Meeting, AIAA Paper 2018-0633, 2018.

M. J. McClearn, F. R. Schauer, R. Huff, M. D. Polanka, J. L. Hoke, and M. Fotia. A Disk Rotating Detonation Engine Part 2: Operation. In 2018 AIAA Aerospace Sciences Meeting, AIAA Paper 2018-1607, 2018.

F. A. Bykovskii and V. V. Mitrofanov. Detonation combustion of a gas mixture in a cylindrical chamber. Combustion, Explosion and Shock Waves, 16(5):570-578, 1980.

A. Naples, J. Hoke, J. Karnesky, and F. Schauer. Flowfield Characterization of a Rotating Detonation Engine. In 51t AIAA Aerospace Sciences Meeting, AIAA Paper 2013-0278, 2013.

B. A. Rankin, D. R. Richardson, A. W. Caswell, A. Naples, J. L. Hoke, and F. R. Schauer. Imaging of OH* Chemiluminescence in an Optically Accessible Nonpremixed Rotating Dertonation Engine. In 53rd AIAA Aerospace Sciences Meeting, AIAA Paper 2015-1604, 2015.

B. A. Rankin and F. R. Schauer. Investigation of the structure of detonation waves in a non-premixed hydrogen-air rotating detonation engine using mid-infrared imaging. Proceedings of the Combustion Institute, 37(3):3479-3486, 2019.

F. Chacon and M. Gamba. Study of Parasitic Combustion in an Optically Accessible Continuous Wave Rotating Detonation Engine. In 2019 AIAA Aerospace Sciences Meeting, AIAA Paper 2019-0473, 2019.

D. Schwer and K. Kailasanath. Feedback into Mixture Plenums in Rotating Detonation Engines. In 50th AIAA Aerospace Sciences Meeting, AIAA Paper 2012-0617, Jan. 2012.

D. Schwer and K. Kailasanath. Fluid dynamics of rotating detonation engines with hydrogen and hydrocarbon fuels. Proceedings of the Combustion Institute, 34(2):1991-1998, 2013.

K. Wu, S. Zhang, M. Luan, and J. P. Wang. Effects of flow-field structures on the stability of rotating detonation ramjet engine. Acta Astronautica, 168(1):174-181, 2020.

D. E. Paxson. Numerical Analysis of a Rotating Detonation Engine in the Relative Reference Frame. In 52nd Aerospace Sciences Meeting, AIAA Paper 2014-0284, 2014.

R. W. Houim and R. T Fievisohn. The influence of acoustic impedance on gaseous layered detonations bounded by an inert gas. Combustion and Flame, 179(1):185-198, 2017.

K. Kailasanath. Rotating Detonation Engine Research at NRL. In 2013 International Workshop for Detonations in Propulsion, July 2013.

D. M. Davidenko, I. Gokalp, and A. N. Kurdrvavtsev. Numerical Simulation of the Continous Rotating Hydrogen-Oxygen Detonation with a Detailed Chemical Mechanism. In West-East High Speed Flow Field Conference, Nov. 2007.

J. C. Shank. Development and Testing of a Rotating Detonation Engine Run on Hydrogen and Air. MS thesis, Air Force Institute of Technology, 2012.

Y. T. Shao, M. Liu, and J. P. Wang. Numerical Investigation of Rotating Detonation Engine Propulsive Performance. Combustion Science and Technology, 182(11-12):1586-1597, 2010.

J. R. Burr and K. H. Yu. Detonation Propagation in a Linear Channel with Discrete Injectors and Side Relief. In 26th International Colloquium on the Dynamics of Explosions and Reactive Systems, ICDERS Paper 2017-1107, Aug. 2017.

R. T. Fievisohn and K. H. Yu. Parametric Study of an Ethylene-Air Rotating Detonation Engine Using an Ideal Model. In 54th AIAA Aerospace Sciences Meeting, AIAA Paper 2016-1403, Jan. 2016.

Y. Uemura, A. Koichi Hayashi, M. Asahara, N. Tsuboi, and E. Yamada. Transverse wave generation mechanisms in rotating detonation. Proceedings of the Combustion Institute, 34(2):1981-1989, 2013.

J. Fujii and J. Kasahara. Numerical investigation on detonation velocity in rotating detonation engine. Proceedings of the Combustion Institute, 36(2):2665-2672, 2017.

S. Yao, Z. Ma, S. Zhang, M. Luan, and J. P. Wang. Reinitiation phenomenon in hydrogen-air rotating detonation engine. International Journal of Hydrogen Energy, 42(47):28588-28598, 2017.

L. Deng, H. Ma, C. Xu, X. Liu, and C. Zhou. The feasibility of mode control in rotating detonation engine. Applied Thermal Engineering, 129(1):1538-1550, 2018.

Y. Uemura, A. Koichi Hayashi, M. Asahara, N. Tsuboi, and E. Yamada. Transverse wave generation mechanisms in rotating detonation. Proceedings of the Combustion Institute, 34(2):1981-1989, 2013.

F. A. Bykovskii, A. A. Vasil'ev, E. F. Vedernikov, and V. V. Mitrofanov. Explosive combustion of a gas mixture in radial annular chambers. Combustion, Explosion and Shock Waves, 30(4):510-516, 1994.

C. A. Nordeen, D. Schwer, F. Schauer, J. Hoke, T. Barber, and B. M. Cetegen. Role of inlet reactant mixedness on the thermodynamic performance of a rotating detonation engine. Shock Waves, 26(4):417-428, 2016.

J. Sun, J. Zhou, S. Liu, and Z. Lin. Numerical investigation of a rotating detonation engine under premixed/non-premixed conditions. Acta Astronautica, 152(1):630-638, 2018.

Y. Wang, J. Le, C. Wang, and Y. Zheng. A non-premixed rotating detonation engine using ethylene and air. Applied Thermal Engineering, 137(1):749-757, 2018.

J. Sousa, G. Paniagua, and E. C. Morata. Thermodynamic analysis of a gas turbine engine with a rotating detonation combustor. Applied Energy, 195(1):247-256, 2017.

S. Zhou, H. Ma, Y. Yang, and C. Zhou. Investigation on propagation characteristics of rotating detonation wave in a radial-flow turbine engine combustor model. Acta Astronautica, 160(1):15-24, 2019.

A. Okninski, J. Kindracki, and P. Wolanski. Rocket rotating detonation engine flight demonstrator. Aircraft Engineering and Aerospace Technology, 88(4):480-491, 2016.

G. Ge, L. Deng, H. Ma, X. Liu, and C. Zhou. Effect of blockage ratio on the existence of multiple waves in rotating detonation engine. Acta Astronautica, 164(1):230-240, 2019.

M. L. Fotia, J. Hoke, and F. Schauer. Study of the ignition process in a laboratory scale rotating detonation engine. Experimental Thermal and Fluid Science, 94(1):345-354, 2018.

K. T Walsh and M. D. Smooke. Experimental and computational study of CH, CH*, and OH* in an axisymmetric laminar diffusion flame. Symposium (International) on Combustion, 27(1):615-623, 1998.

J. R. Burr and K. H. Yu. Mixing in Linear Detonation Channel with Discrete Injectors and Side Relief. In 57th AIAA Aerospace Sciences Meeting, AIAA Paper 2019-1014, Jan. 2019.

D. Schwer, K. Kailasanath, J. Burr, and K. Yu. Simulations of the Linear Model Detonation Engine. In *10th U.S. National Combustion Meeting*, Paper 1K10, 2017.

C. Lietz, N. L. Mundis, S. A. Schumaker, and V. Sankaran. Numerical Investigation of Rotating Detonation Rocket Engines. In *2018 AIAA Aerospace Sciences Meeting*, AIAA Paper 2018-0882, 2018.

S. Prakash, R. Fiévet, V. Raman, J. Burr, and K. H. Yu. Analysis of the Detonation Wave Structure in a Linearized Rotating Detonation Engine. *AIAA Journal*, 0(0):1-15, 2019.